



**MONASH MOTORSPORT**  
**FINAL YEAR THESIS COLLECTION**

**Carbon Fibre Composite Monocoque  
Chassis for a Formula Student Race Car**

*Leon Shi & Kieran Rice - 2019*

The Final Year Thesis is a technical engineering assignment undertaken by students of Monash University. Monash Motorsport team members often choose to conduct this assignment in conjunction with the team.

The theses shared in the Monash Motorsport Final Year Thesis Collection are just some examples of those completed.

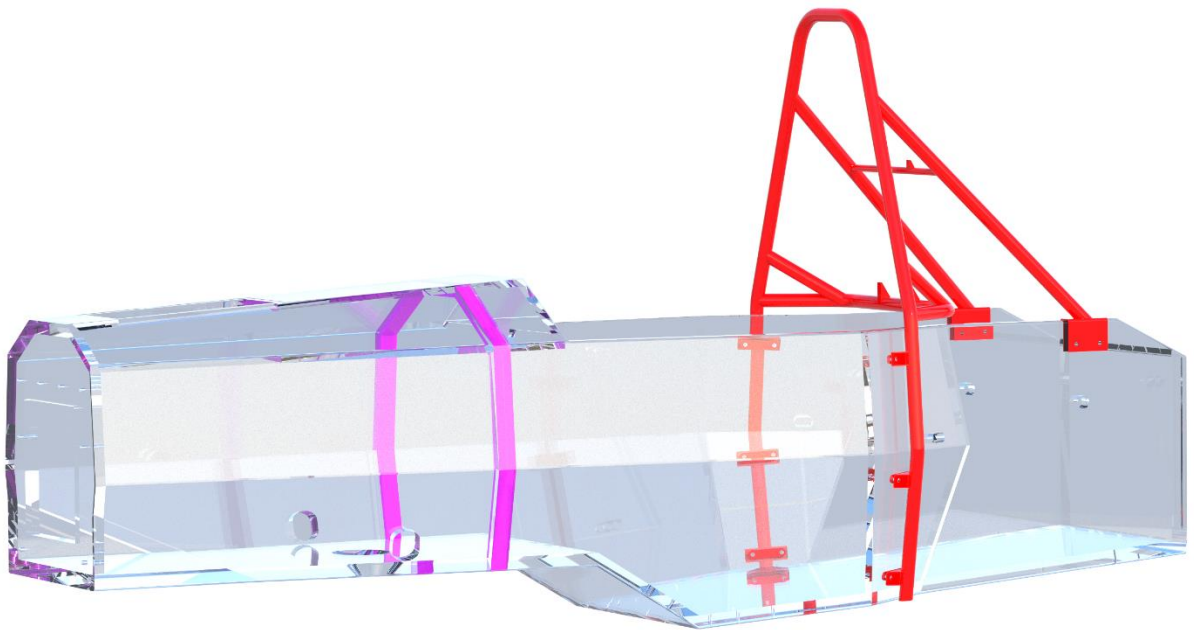
These theses have been the cornerstone for much of the team's success. We would like to thank those students that were not only part of the team while at university but also contributed to the team through their Final Year Thesis.

The purpose of the team releasing the Monash Motorsport Final Year Thesis Collection is to share knowledge and foster progress in the Formula Student and Formula-SAE community.

**We ask that you please do not contact the authors or supervisors directly, instead for any related questions please email [info@monashmotorsport.com](mailto:info@monashmotorsport.com)**



# CARBON FIBRE COMPOSITE MONOCOQUE CHASSIS FOR A FORMULA STUDENT RACE CAR



Leon Shi and Kieran Rice

Supervised by: Dr. Scott Wordley

# Summary

The work presented in this report is the culmination of over four years of development dating back to late 2014. 2019 saw the Monash Motorsport Formula Student team successfully implement its first pair of carbon fibre composite monocoque chassis, replacing the tried and tested tubular steel spaceframe.

To accomplish this objective, the project was divided into several key components. These included:

- An understanding of the rules restrictions and guidelines associated with a composite chassis
- An in-depth literature study of the behaviour of composite materials and sandwich structures
- Geometry design of the monocoque with detailed considerations for packaging, manufacturability and outright performance
- Structural finite element analysis with validation through physical testing
- Manufacturing of the two monocoques
- Post manufacture evaluation and further testing

Overall, every one of these individual tasks was either met or exceeded, resulting in two monocoques weighing in at 25.1kg and 26.3kg, with a physically tested torsional stiffness of 3551Nm/deg. This represented an almost 80% increase in chassis stiffness compared to the previous iteration steel spaceframe chassis. This project has also resulted in the development of new design tools specifically catered for the design of a composite chassis, which will be of major assistance to future monocoque designers at Monash Motorsport.

# Acknowledgements

The authors would like to acknowledge the contributions of Dr. Scott Wordley and the entire Monash Motorsport team. In particular, the individual contributions of Nicholas McIver, Christopher Olorenshaw, Anesu Kusangaya, Andrew De Morton and Filip Surla for their mentorship over the years. The authors would also like to pay a special mention to Alan Coram and the Institute of Railway Technology, Santhosh Babu and the Mechanical Engineering Workshop staff, and Wayne Max and Tickford Racing for their support of this project.

# Table of Contents

List of Abbreviations

List of Figures and Tables

Figures

Tables

<b>Chapter 1 Background</b>	<b>1</b>
Formula Student	
Monash Motorsport	
Chassis Types	
<b>Chapter 2 Formula Student Rules</b>	<b>10</b>
SES	
<b>Chapter 3 Chassis Loads</b>	<b>17</b>
Chassis Deformation	
Load Cases	
<b>Chapter 4 Composite Theory</b>	<b>21</b>
Overview	
Classical Laminate Theory	
Beam Theory for Sandwich Panels	
SES Method	
Insert Theory	
<b>Chapter 5 Design</b>	<b>36</b>
Design Goals	
Design Constraints	
Manufacturing Considerations	
Material Selection	
Development of the Design	
Final Design	
<b>Chapter 6 Analysis</b>	<b>56</b>
MATLAB	
3 Point Bend FEA	
Chassis Torsion FEA	
<b>Chapter 7 Physical Testing</b>	<b>70</b>
Test Panel Production	
3 Point Bend Testing	



Perimeter Shear Testing	
Hardpoint Insert Testing	
Final Chassis Layup Schedule	
<b>Chapter 8 Production</b>	<b>85</b>
Manufacturing Proof of Concept	
Manufacturing Procedure	
<b>Chapter 9 Evaluation &amp; Review</b>	<b>96</b>
Evaluation	
Post-manufacture Inspection	
Torsion Bench Test	
Post-Driving Evaluation	
<b>Conclusion</b>	
<b>Chapter 11 Future Developments</b>	<b>107</b>
Chassis Design	
Analysis	
Manufacturing	
Testing and Validation	
<b>Chapter 12 References</b>	<b>113</b>

# List of Abbreviations

3PB	3 point bend
ACP	ANSYS Composite PrepPost
AIP	Anti-intrusion plate
AMTS	Ace Metal Treatment Services
ANSYS	Analysis System
ATTAR	Advanced Technology Testing and Research
CAD	Computer-aided design
CFRP	Carbon fibre reinforced polymer
CG	Centre of gravity
CNC	Computer numerical control
CCW	Counter clockwise
CTE	Coefficient of thermal expansion
CW	Clockwise
ECSS	European Cooperation for Space Standardization
EI	Flexural rigidity
EV	Electric vehicle
FBHS	Front bulkhead support structure
FDR	Final design review
FEA	Finite element analysis
FSA	Formula Student Austria
FSAE	Formula SAE
FSAE-A	Formula SAE-Australasia
FSG	Formula Student Germany
FSUK	Formula Student United Kingdom
FYP	Final year project
HP	Hardpoint
IA	Impact attenuator
IC	Internal combustion vehicle
IRT	Institute of Railway Technology
LLTD	Lateral load transfer distribution
MADA	Monash Art Design & Architecture
MMS	Monash Motorsport
M19-C	Monash Motorsport's 2019 Internal Combustion Vehicle
M19-E	Monash Motorsport's 2019 Electric Vehicle
NDT	Non-destructive testing
PS	Perimeter shear
RHS	Rectangular hollow section
SAE	Society of Automotive Engineers
SES	Structural equivalency spreadsheet
SIS	Side impact structure
TU	Technical University
UT	Ultrasonic
UTM	Universal testing machine
VSAL	Virtual swing arm length

# List of Figures and Tables

## Figures

Figure 1.1: Formula Student Germany, 2018 (©FSG Shidhartha). [1]	1
Figure 1.2: Snapshot overview of the Formula Student competition worldwide. [4]	1
Figure 1.3 Overview of events and points breakdown for Formula Student Germany. [4]	2
Figure 1.4: Monash Motorsport presenting at the Business Plan finals at Formula Student Austria, 2018. [6]	3
Figure 1.5: M17-C Engineering Design Event at Formula Student UK, 2018. [6]	3
Figure 1.6: M17-C Acceleration Event at Formula Student Germany, 2018 (©FSG Schulz). [1]	4
Figure 1.7: Endurance Event at Formula Student UK, 2018. [6]	5
Figure 1.8 The Monash Motorsport team at FSAE-Australasia, 2018. [6]	6
Figure 1.9: M17-E steel spaceframe chassis. [6]	7
Figure 1.10: McLaren MP4-1 composite monocoque chassis (foreground) with McLaren MP4-12 road car monocoque (background). [10]	8
Figure 1.11: Hybrid chassis of Rennteam Uni Stuttgart e.V. F0711-12, 2017. [11]	8
Figure 2.1: Primary structure elements in the Monash M17/18 steel spaceframe chassis design.	10
Figure 2.2: Cockpit opening template (left) and cockpit internal cross section template (right). [12]	12
Figure 2.3: Percy template placement in relation to driver controls. [12]	12
Figure 2.4: Workflow of the SES document.	13
Figure 2.5: SES Cover Sheet.	14
Figure 2.6: Panel comparison worksheet for the front hoop bracing structure.	15
Figure 2.7: The completed SES document for FSAE-A 2019 showing the panel comparison worksheet.	16
Figure 3.1: Steady State LLTD Tuning Range.	17
Figure 3.2: Points Delta to Target Stiffness.	18
Figure 3.3: Graphical illustration of chassis deformation types. [16]	19
Figure 3.4: Torsion FEA setup in ANSYS.	19
Figure 3.5: The Ring spreadsheet.	20
Figure 4.1: Fibre and matrix loading in parallel. [18]	21
Figure 4.2: Fibre and matrix loading in series. [18]	21
Figure 4.3: Strain and stress variation through the thickness of the laminate. [19]	22
Figure 4.4: Local and global axes of an angle lamina. [19]	22
Figure 4.5: (a) Simply supported beam, (b) cross section on A-A [20].	25
Figure 4.6: Facesheet yielding failure (compression). [22]	26
Figure 4.7: Intra-cell dimpling of the facesheet skins. [22]	26
Figure 4.8: Core shear or 'shear crimping'. [22]	27
Figure 4.9: Basic types of insert loading. [24]	28
Figure 4.10: Potting Geometry [24]	30
Figure 4.11: Failure modes of CFRP face sheets. [24]	31
Figure 4.12: Nomenclature for ultimate in-plane load against tensile failure. [24]	32
Figure 4.13: Stress concentration factor. [24]	32
Figure 4.14: Insert subjected to combined loading. [24]	34
Figure 5.1: Exploitation of monocoque geometry by TUfast for a high downforce aerodynamic package. [25]	37
Figure 5.2: Side view (top) and overhead view (bottom) showing cockpit template clearance.	37
Figure 5.3: Packaging of the combustion and electric powertrains in the 2017 chassis design.	38
Figure 5.4: Packaging of the KTM 690 and driveline.	38
Figure 5.5: Overhead view (left) and rear isometric view (right) of electric powertrain packaging.	39
Figure 5.6: M19 front suspension geometry as modelled in Susprog, a kinematic suspension design and analysis tool.	39
Figure 5.7: Changes in rear suspension packaging with 2017 (left) and 2019 (right).	40
Figure 5.8: MMS endurance drivers in the TUfast eb2018 during 2018 driver swap.	41
Figure 5.9: Clearance between seat and accumulator.	41
Figure 5.10: Early concept comparison of driver seating position.	42
Figure 5.11: Preliminary CAD design overlaid onto images taken from ergonomics rig bench testing.	42
Figure 5.12: Example test specimens from 2017 of a flat panel that has been 'cut' and 'folded'.	43
Figure 5.13: Edith Cowan University Racing 2014 cut and fold monocoque chassis. [27]	44
Figure 5.14: Monocoque plug and composite tool from Revolve NTNU, 2016. [28]	44
Figure 5.15: Placement of chassis inserts inside the mould, Revolve NTNU, 2014. [29]	45
Figure 5.16: RMIT Electric Racing R19e chassis mould, 2019. [30]	46

Figure 5.17: Radar chart for selection of manufacturing method.	47
Figure 5.18: Two halves, front and rear, of the RMIT Electric Racing R19e monocoque. [30]	48
Figure 5.19: Core selection spreadsheet developed by McIver, Olorenshaw and Kusangaya in 2016.	49
Figure 5.20: Initial concept from 21/04/2018.	50
Figure 5.21: Fifth iteration from 01/10/2018.	51
Figure 5.22: Eighth iteration from 01/01/2019.	51
Figure 5.23: Validation of driver seating position on the ergonomics rig.	52
Figure 5.24: Eleventh iteration from 13/01/2019.	52
Figure 5.25: Refinement of front wing mounting (top) and front bulkhead (bottom) of the monocoque.	53
Figure 5.26: Final design overview.	54
Figure 5.27: Render of the final design.	54
Figure 6.1: 3 point bend MATLAB script.	55
Figure 6.2: Comparison of MATLAB 3PB scripts for Cycom 970 sandwich panel strengths.	56
Figure 6.3: Comparison of Cycom 970 and GMS EP-270 sandwich panel strengths.	56
Figure 6.4: Preliminary chassis layup schedule.	57
Figure 6.5: Hardpoint insert MATLAB script by Kusangaya.	58
Figure 6.6: ANSYS Workbench for 3PB FEA.	60
Figure 6.7: ANSYS mesh setup.	61
Figure 6.8: 6 ply sandwich panel modelled in ACP, showing 0/45 degree fibre directions.	62
Figure 6.9: Model conditions in ANSYS Mechanical.	62
Figure 6.10: Ultimate load time step of the composite panel, showing full propagation of ply failure through the width of the panel.	63
Figure 6.11: Comparison of failure loads simulated using FEA and MATLAB.	64
Figure 6.12: (Left) Existing CAD of the M19 monocoque. (Right) Simplified monocoque CAD.	65
Figure 6.13: CAD representation of the powertrain.	65
Figure 6.14: CAD representation of the suspension.	66
Figure 6.15: ACP Layup thickness plot.	66
Figure 6.16: FEA Setup.	67
Figure 6.17: Compliance Distribution.	68
Figure 6.18: FEA results (Rigid Suspension) showing degrees of rotation along the monocoque.	68
Figure 7.1: Test panel manufacture showing core crush support frame (background) and MTA 240 adhesive film (foreground).	69
Figure 7.2: 3 point bend panel sample being loaded into the Monash University autoclave.	69
Figure 7.3: User interface of the Monash University autoclave automation software.	70
Figure 7.4: Speed test results for 3 point bending tests conducted in 2016.	70
Figure 7.5: 3 point bend test rig setup on the Instron 100kN UTM at the IRT Highbay Area.	71
Figure 7.6: User interface of Instron computer controller.	72
Figure 7.7: Steel baseline bend test setup (top) and force-displacement graph (bottom).	72
Figure 7.8: Composite panel specimen setup on the Instron UTM (note the modified panel supports).	73
Figure 7.9: Force-displacement graph for SES 3 point bend tests.	73
Figure 7.10: Results comparison between FEA, MATLAB and physical 3 point bend tests.	74
Figure 7.11: Panel stiffness comparison between FEA, MATLAB and physical 3 point bend tests.	75
Figure 7.12: Perimeter shear test setup on the Instron UTM.	76
Figure 7.13: Force-displacement graph for SES perimeter shear tests.	76
Figure 7.14: Insert pull-out test rig setup on the Instron UTM for inclined loading.	77
Figure 7.15: Hardpoint insert force-displacement graph.	78
Figure 7.16: Results comparison between MATLAB and physical hardpoint insert pull-out tests.	79
Figure 7.17: Insert stiffness comparison between MATLAB and physical hardpoint insert pull-out tests.	79
Figure 7.18: Detailed inspection of the hardpoint insert potting from the foaming adhesive.	80
Figure 7.19: Results comparison with modified MATLAB model.	81
Figure 7.20: Final chassis layup schedule for the combustion vehicle.	81
Figure 7.21: Final chassis layup schedule for the electric vehicle.	82
Figure 8.1: Mould test piece as constructed.	83
Figure 8.2: Test piece outcome.	84
Figure 8.3: CAD of M19-E monocoque mould.	85
Figure 8.4: Assembled mould for M19-C.	85
Figure 8.5: Proposed manufacturing timeline.	86
Figure 8.6: Revised manufacturing timeline.	86
Figure 8.7: Typical autoclave layup procedure.	87
Figure 8.8: Ply book for the production of the M19-C monocoque.	87
Figure 8.9: Composite plies nested onto the prepreg CFRP roll in NX 12.0.	88
Figure 8.10: Cutting instructions cover sheet with instructions.	88



Figure 8.11: Outer skin during layup.	89
Figure 8.12: Core chamfering geometry.	89
Figure 8.13: Front roll hoop, core and inserts cured and bonded in.	90
Figure 8.14: Vacuum bagging process for the mould.	91
Figure 8.15: Celebratory social media marketing post for the completion of the new monocoques.	91
Figure 9.1: First ply with bolt locating pins visible.	95
Figure 9.2: Prototype Dremel chamfering jig.	96
Figure 9.3: Core insertion process.	97
Figure 9.4: Test fitment of the front hoop and inserts.	97
Figure 9.6: First prepreg ply of the inner skin with adhesive film.	100
Figure 9.7: Delaminated samples.	101
Figure 9.8: Test setup.	102
Figure 9.9: Spreadsheet calculator for torsion testing.	103
Figure 9.10: Summary of hub-to-hub installation stiffness results.	104
Figure 9.11: Comparison of compliance distribution along the chassis longitudinal axis between physical and FEA results.	104
Figure 10.1: Conceptual front bulkhead size reduction.	106
Figure 10.2: Prototype waterjet cut CFRP hardpoint insert.	108
Figure 10.3: Constrained working conditions inside the mould.	109
Figure 10.4: Top and bottom chassis moulds from University of Auckland 2013. [40]	109
Figure 10.5: CNC ply cutting trial with Monash Food Innovation.	109
Figure 10.6: CNC routed aluminium honeycomb core.	110

## Tables

Table 4.1: Effect of sandwich components on insert load-bearing capability. [24]	29
Table 6.1: Critical wishbone chassis insert loads.	59
Table 6.2: Preliminary hardpoint sizing and failure loads.	59
Table 7.1: Hardpoint insert physical testing parameters.	78

# Chapter 1 Background

## Formula Student

### Overview



Figure 1.1: Formula Student Germany, 2018 (©FSG Shidhartha). [1]

Formula Student and Formula SAE are international engineering competitions where university students design, build, test and race their own formula style single seater race cars. Formula SAE was first established in the United States in 1981 [2] and has been growing ever since, with well over 950 teams now competing worldwide [3]. Official competitions are now held on nearly all continents across the globe in countries including but not limited to Australia, United States of America, United Kingdom, Germany, Austria and China.

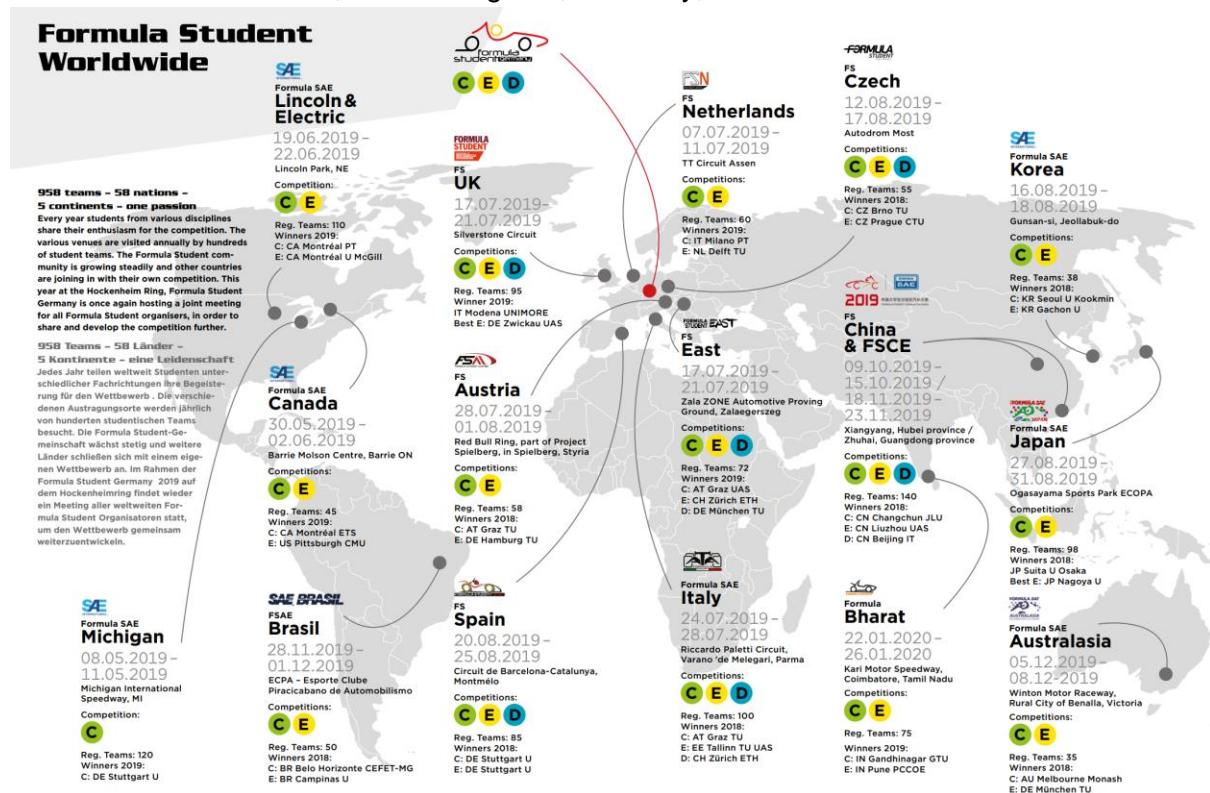


Figure 1.2: Snapshot overview of the Formula Student competition worldwide. [4]

The basic premise for Formula Student is that teams must design and manufacture a prototype vehicle for the non-professional, weekend, competition market [5]. The overall vehicle design places an emphasis on acceleration, braking and handling rather than top speed and power. Rules and guidelines are introduced to ensure the safety of drivers and spectators, however they are still relatively unrestrictive compared to other levels of motorsport and encourage students to explore and be creative in their designs.

## The Competition

The competition in itself is scored on multiple categories, with the overall winner being the team with the highest sum of points scored across all of these categories. There are two distinct scoring disciplines: static events and dynamic events.

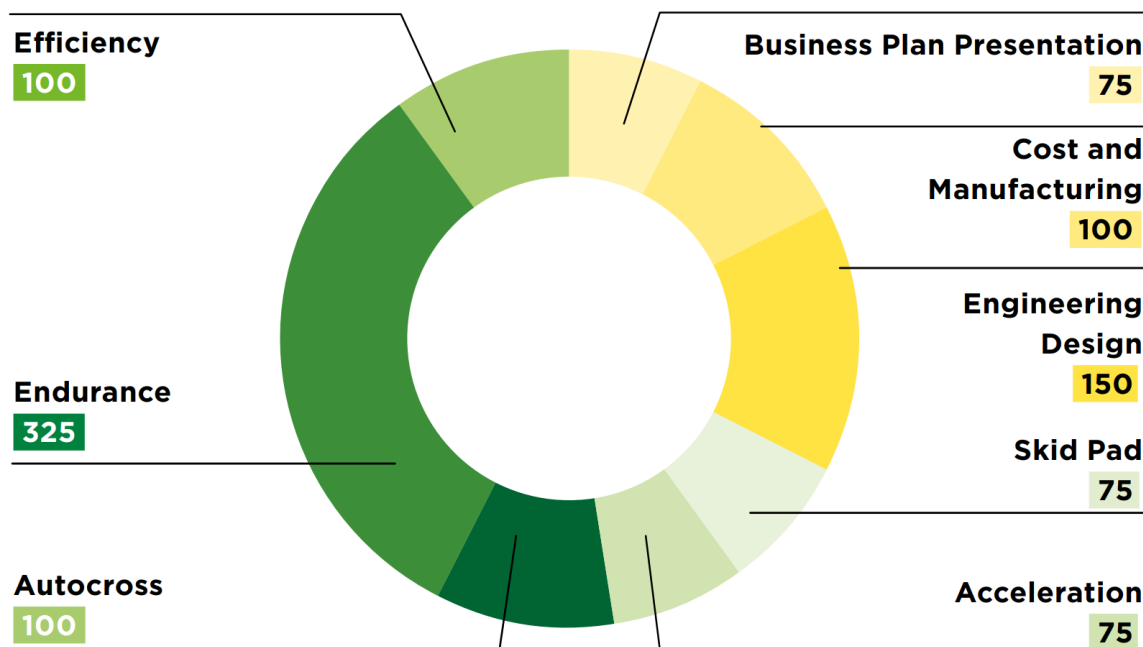


Figure 1.3 Overview of events and points breakdown for Formula Student Germany. [4]

### Static Events

Communication is an important part of an engineer's skill sets, and the competition recognises this, with up to 325 of the maximum 1000 points available being awarded for static events.

#### Business Plan Presentation

The team must devise a business logic case for which they can market their prototype race car to a target audience of amateur weekend racers. Presenters are given 10 minutes in front of a panel of judges 'Shark Tank' style to convince them that their investment in this pseudo-company is worthwhile.

#### Cost and Manufacturing

The overall finances in any large engineering project is often subject to high scrutiny. This case is no different for Formula Student. Teams must compile a report detailing the cost of each component as well as the associative labour and manufacturing costs and present these



Figure 1.4: Monash Motorsport presenting at the Business Plan finals at Formula Student Austria, 2018. [6]

findings to a panel of judges. The judges rank teams based on accuracy of the cost report as well as the level of understanding from the students of the manufacturing processes involved.

### Engineering Design

Teams must submit an eight page technical report detailing and justifying the overall design of their vehicle prior to competition. During the actual event, a panel of judges with a wide range of expertise ranging from vehicle dynamics, structures, aerodynamics, powertrain and ergonomics assess the students' knowledge and reasoning behind their design. Teams with well justified explanations and who show a high level of understanding of their vehicle will be awarded the highest scores.



Figure 1.5: M17-C Engineering Design Event at Formula Student UK, 2018. [6]

## Dynamic Events

The main component of the competition worth 675 points, the dynamic events aim to test the vehicles' acceleration, agility and efficiency in a series of events. Unlike most motorsport events, the drivers are all university students and mostly amateurs when it comes to racing. To promote clean racing, the track limits are marked by cones, and hitting those cones will result in time penalties.

### Skid Pad

The skid pad event places an emphasis on the cornering capabilities of the vehicle. Teams must drive in a tight figure 8 configuration, running two loops in one direction followed by two loops in the other. The average of the best runs in both the left and right directions is used as the final time.

### Acceleration

A straightforward 75 metre sprint, from a standing start. Extracting the maximum longitudinal grip from the tyre, as well as peak torque, is key to a good performance. Electric vehicles have an advantage in this area due to the immediate torque delivery from the motors. The best 4 wheel drive electric vehicles are capable of achieving times less than 3.25 seconds and cross the line with a top speed of 140kph.



Figure 1.6: M17-C Acceleration Event at Formula Student Germany, 2018 (©FSG Schulz). [1]

### Autocross

The autocross event is a one lap sprint on a challenging technical circuit with straights, high speed corners, hairpins, slaloms and chicanes. The finishing position in autocross also determines the starting order for the endurance event.

## Endurance

This event is the most challenging but also most rewarding for the teams, worth up to 325 of the available 1000 points at competition. It consists of a 22km sprint, including a pit stop for changing drivers. Speed and reliability are the necessary attributes a car must have to succeed.



Figure 1.7: Endurance Event at Formula Student UK, 2018. [6]

## Efficiency

This event is a measure of how efficient a vehicle is in terms of fuel or energy consumption relative to the speed. The consumption numbers are recorded as part of the endurance event and are used to calculate the scoring in this event.

# Monash Motorsport

Monash Motorsport (MMS) is a Formula Student team based out of Monash University's Clayton campus in Melbourne, Australia. The team is one of the select few in the world to field three vehicles across multiple classes: combustion (CV), electric (EV) and driverless (DV). There are over 100 active team members from a multitude of engineering disciplines (aerospace, mechanical, electrical, mechatronics...etc.), as well as commerce, law, design and science. As of October 2019, the combustion vehicle is ranked 2nd worldwide, while the electric vehicle is 7th [3].

## Team History

Monash Motorsport was first established in 2000 to compete in the Australian FSAE competition with a combustion vehicle. After a challenging first few years, the team achieved its first podium placing with a 3rd place overall in the 2007 FSAE-Australasia competition, before an incredible seven year winning streak in Australia between 2009 to 2015. During that



Figure 1.8 The Monash Motorsport team at FSAE-Australasia, 2018. [6]

period, the team also competed overseas in the United Kingdom and Germany, twice achieving a podium position competing amongst the top teams around the world. After a disappointing campaign in 2016 by Monash Motorsport's standards (3rd place in Australia), the team embarked on a new era, fielding an all-new electric vehicle in combination with the proven combustion vehicle. The team bounced back in style, cleaning up the 2017 Australasian competition with first place across both vehicle classes, the first team to do so in Australia. 2018 saw the team further solidify its position as one of the most successful Formula Student teams in the world, achieving 1st and 3rd at Formula Student UK and 2nd at Formula Student Austria, before again winning down under at the end of the year. In 2019, the team's new cars seek to integrate, refine and evolve from the successful 2017-18 design, including the addition of a new autonomous vehicle.

## Chassis Types

The main function of the chassis is to maintain driver safety at all times. Secondary to this is to be able to transfer the tyre loads both in the longitudinal and lateral directions, as well as to internally package the driver controls and powertrain systems. The Formula Student rules are very open to design freedom in that they allow for three main chassis configurations.

### Steel Spaceframe

This is the most commonly used chassis configuration in Formula Student. The spaceframe is a truss-like frame structure, usually welded together using mild steel or 4130 chromoly round steel tubing. This form of chassis is the least expensive to fabricate which is why it is so popular for many teams in Formula Student.

The usage of spaceframe chassis designs in the automotive industry dates back to the 1950s, with Mercedes being the first manufacturer to make use of a tubular spaceframe design in the 300SLR racing car, followed by the famous 300SL 'gullwing' road car [7]. Variations of the

tubular spaceframe are still used today in high performance vehicles, notably the Audi R8 sports car and the Australian Supercars Championship touring cars.

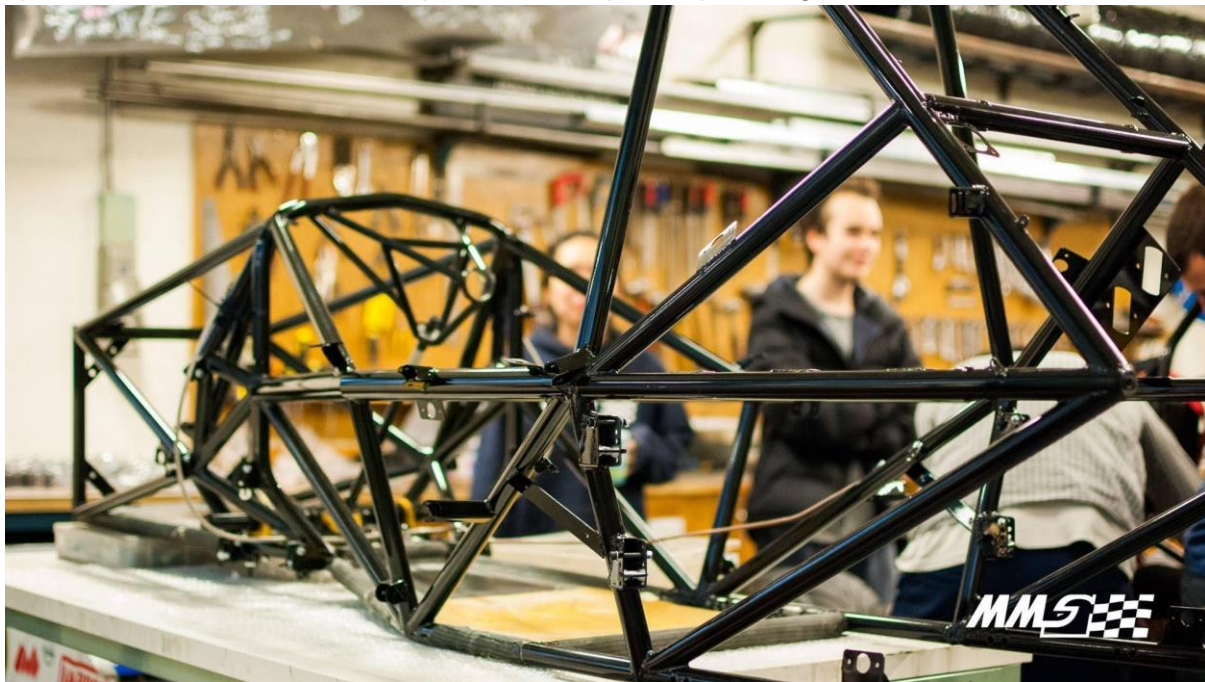


Figure 1.9: M17-E steel spaceframe chassis. [6]

## Composite Monocoque

The word *monocoque* is of French origin, and the literal translation to English is *single shell*. As the name suggests, a monocoque is a structural component in which the outer body shell or skin is fully load bearing.

The history of the monocoque originates in the naval and aviation sectors, with the first widely known usage of a composite monocoque in automobile chassis design taking the form of the McLaren MP4-1 Formula One racing car which competed in the 1981 Formula One season. Aluminium body monocoques had previously been used in motorsport as early as the 1960s with Lotus pioneering it in their Formula One cars [8]. The key motivator for moving to a monocoque design in a period when the spaceframe was standard was its lightness, stiffness and strength. This became very apparent early on to any doubters of the monocoque when John Watson crashed his McLaren MP4-1 heavily during practice for the 1981 Italian Grand Prix and walked away from the accident completely unscathed [9].

In modern day motorsport and Formula Student, the composite monocoque is nearly always constructed using sandwich panel technology. This consists of two composite laminates sandwiching an internal core structure in between. The external skins are usually constructed using carbon fibre reinforced polymers (CFRP) and the core using a honeycomb cell structure from either aluminium or Nomex aramid. Other less commonly used material constructions can include aramid fibres such as Kevlar and foam cores.

A major stepping stone to the widespread adoption of a monocoque chassis in the Formula Student community is cost, as well as manufacturing time. The relatively exotic production



methods, including the necessity for a composite autoclave for processing prepreg composites,



Figure 1.10: McLaren MP4-1 composite monocoque chassis (foreground) with McLaren MP4-12 road car monocoque (background). [10]

drives the cost and complexity of chassis manufacture well beyond what is required for a steel spaceframe.

## Hybrid

A less costly solution to a full monocoque chassis in Formula Student is a hybrid chassis consisting of a monocoque tub for the front half and a steel spaceframe or *rear subframe* at the back. Here the driver is still fully protected by the monocoque structure, with the powertrain assembly being mounted via the rear subframe. This particular chassis design is most popular with combustion vehicles where accessibility to the engine is a high priority and is much easier to achieve without a monocoque structure impeding it.

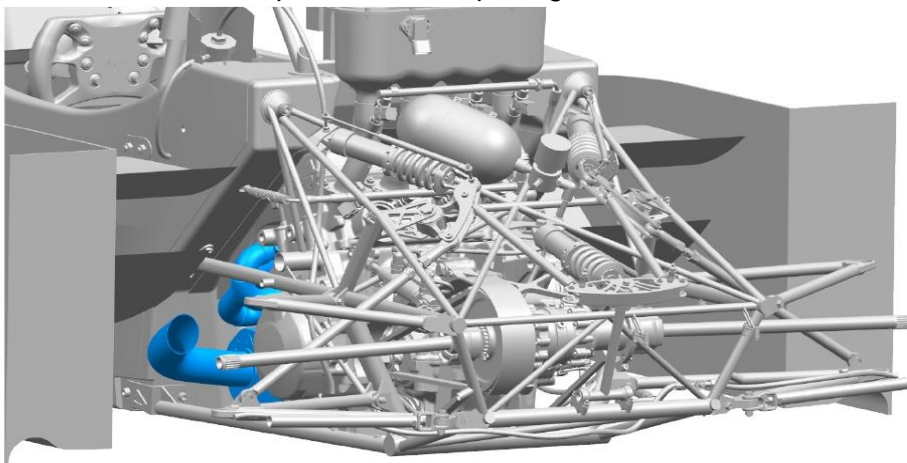


Figure 1.11: Hybrid chassis of Rennteam Uni Stuttgart e.V. F0711-12, 2017. [11]

## Summary

In 2019 Monash Motorsport has designed two new vehicles from a clean slate: one combustion and one electric. In a continuation from the 2017-18 design philosophy, the team has placed a large emphasis on part compatibility and interchangeability between the two cars, as this reduces the manufacturing and design burden on the team as well as making spare components easier to come by. The decision was made very early in the design process at the end of 2018 for Monash Motorsport to move away from a steel spaceframe chassis design to a full monocoque chassis design for both cars.

# Chapter 2 Formula Student Rules

The Formula Student rulebook is a 133 page document [12] outlining both technical and administrative requirements for teams, vehicles and the competition format. A separate rulebook published by the Formula SAE also documents the technical and administrative regulations, albeit with slight deviations. Different competitions organised around the world generally use one or the other ruleset as their base before adding additional addendums to suit the local competition. For instance, competitions held in Australia and the USA utilise the SAE ruleset, while the UK, Germany and the rest of continental Europe follow Formula Student rules. In Monash Motorsport’s situation, the team must design their cars to be rules compliant with both rulesets given they compete both in Australia and in Europe.

From a structural perspective, the basic premise for the composite monocoque chassis in Formula Student is that it must be structurally equivalent or stronger than a baseline rules compliant steel spaceframe chassis. The reasoning behind this is purely for the safety of the vehicle’s occupant. Variations in panel thickness throughout the monocoque chassis are permitted under the current ruleset.

In Formula Student, a baseline steel spaceframe chassis does not require calculations to be performed to prove its strength as long as the design is fully adherent to the rules in terms of tube profile dimensions and position placement. This primary structure is defined as having the following components:

- Main hoop
- Front hoop
- Roll hoop braces and supports
- Side impact structure
- Front bulkhead
- Front bulkhead support structure
- Driver harness attachments

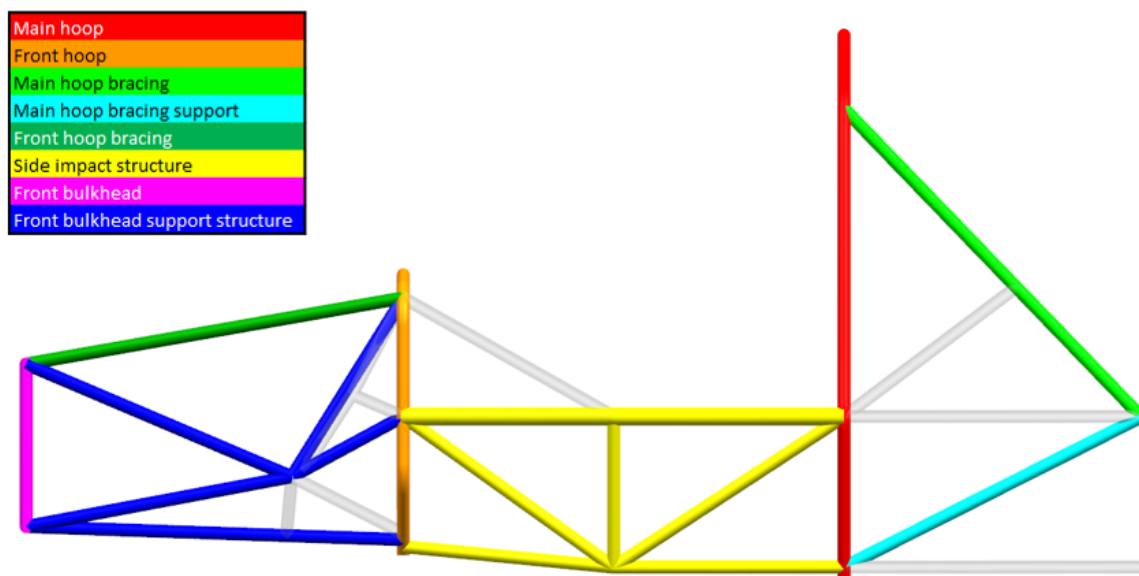


Figure 2.1: Primary structure elements in the Monash M17/18 steel spaceframe chassis design.

## Primary Structure for Monocoques

### Main Hoop

The monocoque main hoop must be constructed from steel tubing as no allowance is made for composite structures in the roll over protection structure. It must fully extend to the bottom of the monocoque on both sides, and be securely and mechanically attached. In total six attachment points are required, three on each side, with each attachment point required to be able to support 30kN in any direction.

### Front Hoop

The front hoop must be metallic, meaning materials other than steel, such as aluminium or titanium tubing, may be used. The same attachment rules as the main hoop apply to the front hoop, with the addition of the allowance of laminating the hoop into the composite monocoque structure.

### Hoop Bracing

Any roll hoop bracing structures must be steel tubing equivalent to the baseline requirements and must attach to the monocoque with the same requirements as the roll hoops.

### Side Impact Structure

The side impact structure is defined as being the structure bounded by the front and main hoops, as well as 320mm above the lowest inside chassis point. The vertical component of the SIS must have an EI equivalent to two baseline steel tubes and half the horizontal floor must have an EI equivalent to one baseline steel tube. The vertical SIS must also have an absorbed energy equivalent to two baseline steel tubes. A further requirement is that in a perimeter shear scenario (see pg. ), the SIS must have a strength greater than 7.5kN. The definition of the SIS differs slightly in the SAE rules. The height of the SIS is defined as being 350mm to the ground, rather than 320mm from the lowest inside chassis point.

### Front Bulkhead

The front bulkhead, when modelled as an L section, must have an equivalent EI to the baseline front bulkhead steel tubing about both the vertical and lateral axes. It must also have the same out of plane shear strength as a 1.5mm thick steel plate.

### Front Bulkhead Support Structure

The FBHS must have an EI equivalent to the sum of the six baseline steel tubes that it replaces. As with the SIS, there is a perimeter shear strength requirement to be greater than 4kN.

### Driver Harness Attachments

The attachment points for the belts must not fail in a collision, otherwise it would severely compromise driver safety. The attachment points for the shoulder and lap belts must be able to withstand 13kN, while the anti-submarine belts must support 6.5kN before failure.

## Additional Rules

Aside from structural regulations, the chassis design is also constrained by driver cockpit rules. The vehicle must be able to accommodate drivers ranging from 5th percentile female to 95th percentile male as a minimum. All of the driver accommodation rules are centred on ensuring that all sized drivers are able to egress out of the vehicle in an emergency without being impeded by any objects within the cockpit. To enforce this, there are several ‘templates’ that must fit within the driver compartment. These are:

- Cockpit opening template
- Cockpit internal cross section template
- 95th percentile male template (colloquially known as *Percy*)

The cockpit opening template concerns the seating area of the cockpit and is particularly important for driver egress in an emergency. It dictates the minimum horizontal area that must be made available. The cockpit internal cross section template stipulates the minimum vertical area of the driver footwell, and is also important for driver egress.

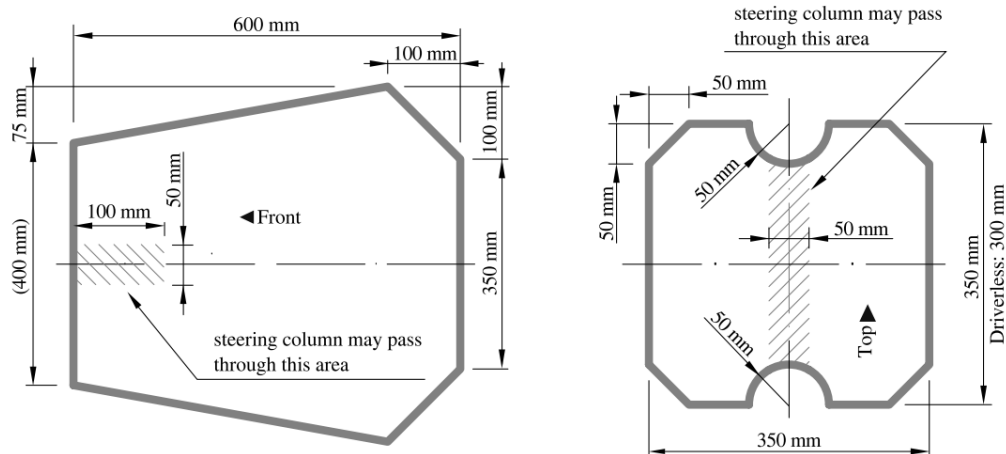


Figure 2.2: Cockpit opening template (left) and cockpit internal cross section template (right). [12]

The Percy template is used to ensure the 95th percentile male fully packages within the vehicle rollover envelope and interfaces with all driver controls such as the head restraint, steering and pedals. Both the cockpit templates and Percy template are used in mechanical scrutineering at the competition to ensure rules compliance has been satisfied on the final vehicle.

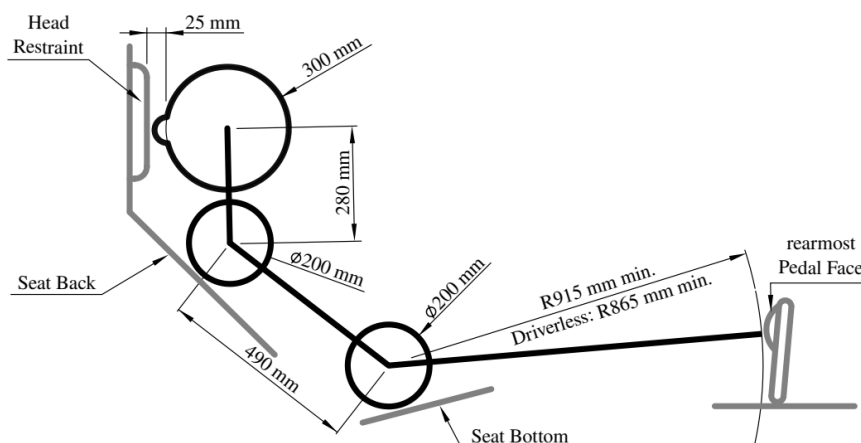


Figure 2.3: Percy template placement in relation to driver controls. [12]

# SES

## Overview

In order to prove that a composite monocoque chassis is structurally equivalent, the Formula Student and SAE organisers have developed a Microsoft Excel spreadsheet calculator, known as the Structural Equivalency Spreadsheet (SES) where teams can input composite material data derived from physical tests to demonstrate equivalency. The SES is a rules required document that must be submitted to the organisers of the competition and be approved by scrutineers before they are allowed to drive in dynamic events.

The SES document breaks down the design of the chassis into its primary structure components, regardless of whether it is a composite monocoque structure or a steel spaceframe. There are two different formats depending on which ruleset is used, following SAE's introduction of a new template for 2019. For the current 2019 Formula Student ruleset and previous SAE rulesets, the SES document workflow is explained below.

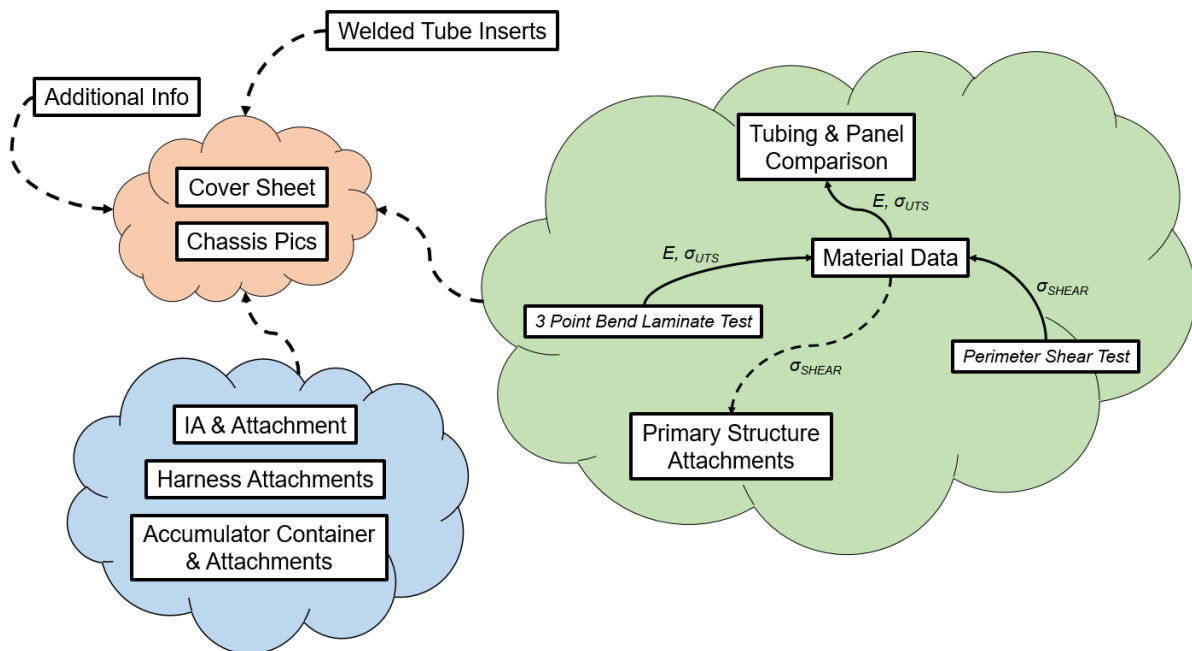


Figure 2.4: Workflow of the SES document.

## Cover Sheet and Chassis Pics

These two sheets in Excel give a general outline of the chassis design, both in terms of structural equivalency compliance as well as a graphical overview of the chassis, similar to the image shown in Figure 2.1. The cover sheet displays all items that have meet equivalency with green cells, while items to be scrutinised in detail or rejected will be shown as orange or red cells, respectively.

## Material Data

The material data worksheet stores all mechanical properties for materials used in the chassis, including steel, aluminium and composite materials. For composite materials, the mechanical

10 In the event that the FS Technical Committee requests additional information or calculations, teams have seven days from the date of request to submit the requested information.

11

12

13

14 University Name [Redacted] Car No (s) & Event(s) [Redacted]

15 Team Contact [Redacted] Email Address [Redacted]

16 Faculty Advisor [Redacted] Email Address [Redacted]

17 Powertrain Type Electric Vehicle

18 Is proof of equivalency for your design required for any of the rules?

19 No. Chassis does not deviate from baseline requirements

Baseline Material Used	Alternative Material Used	Rule No.	Rule Description	Design Description and/or Material Name	Tube and Laminate Equivalency						Tube 1		Tube 2		Tube 3		Composite								
					Area	Yield	UTS as Welded	UTS as Welded with opening correction	UTS as Welded with correction at 100% efficiency	UTS as Welded with correction at 100% efficiency with fillet weld	Tube Material	Tube type	Outside Dimension	Wall Thickness	Tube Material	Tube type	Outside Dimension	Wall Thickness	Tube Material	Tube type	Outside Dimension	Wall Thickness	Material	Panel Thickness	Inner Skin Thickness
YES	NO	T3.8	Main Roll Hoop Tubing	[Redacted]	NA	NA	NA	NA	NA	NA	Steel	Round	25.0	2.50											
YES	NO	T3.9	Front Roll Hoop Tubing	[Redacted]	NA	NA	NA	NA	NA	NA	Steel	Round	25.0	2.50											
YES	NO	T3.10	Main Roll Hoop Bracing Tubing	[Redacted]	NA	NA	NA	NA	NA	NA	Steel	Round	25.4	1.60											
YES	NO	T3.10.5	Main Hoop Bracing Support - Tube Frames	[Redacted]	NA	NA	NA	NA	NA	NA	Steel	Round	25.4	1.20											
YES	NO	T3.11	Front Hoop Bracing - Tube Frames	[Redacted]	NA	NA	NA	NA	NA	NA	Steel	Round	25.4	1.60											
YES	NO	T3.13	Front Bulkhead - Tube Frames	[Redacted]	NA	NA	NA	NA	NA	NA	Steel	Round	25.4	1.60											
YES	NO	T3.14	Front Bulkhead Support - Tube Frames	[Redacted]	NA	NA	NA	NA	NA	NA	Steel	Round	25.4	1.20											
YES	NO	T3.15	Side Impact Structure - Tube Frames	[Redacted]	NA	NA	NA	NA	NA	NA	Steel	Round	25.4	1.60	Steel	Square	25.4	1.60							
YES	NO	T4.5	Shoulder Harness Bar	[Redacted]	NA	NA	NA	NA	NA	NA	Steel	Round	25.0	2.50											
YES	NO	T3.17.3	Impact Attenuator Anti-Intusion Plate	[Redacted]	NA																				
N/A	N/A	T3.11/T3.5	Front Hoop Bracing - Monocoques	[Redacted]	NA	NA	NA	NA	NA	NA	NA														
N/A	N/A	T3.13/T3.5	Front Bulkhead - Monocoques	[Redacted]	NA	NA	NA	NA	NA	NA	NA														
N/A	N/A	T3.14/T3.5	Front Bulkhead Support - Monocoques	[Redacted]	NA	NA	NA	NA	NA	NA	NA														
N/A	N/A	T3.15/T3.5	Side Impact Structure - Monocoques_Side	[Redacted]	NA	NA	NA	NA	NA	NA	NA														
N/A	N/A	3.15/T3.5	Side Impact Structure - Monocoques_Floor	[Redacted]	NA	NA	NA	NA	NA	NA	NA														
N/A	N/A	T3.10.5/T3.5	Main Hoop Bracing Support - Monocoques	[Redacted]	NA	NA	NA	NA	NA	NA	NA														
N/A	N/A	T3.16	Main Hoop Attachment - Monocoques	[Redacted]	NA																				
N/A	N/A	T3.16	Front Hoop Attachment - Monocoques	[Redacted]	NA																				
N/A	N/A	T3.16	Hoop Bracing Attach - Monocoques	[Redacted]	NA																				
N/A	N/A	T1.2.1/T4.8	Firewall	[Redacted]	FA																				
N/A	N/A	T3.17.5	Impact Attenuator Attachment - Monocoques	[Redacted]	NA																				
N/A	N/A	T4.5	Safety Harness Attachment - Monocoques	[Redacted]	NA																				
N/A	N/A	EV 5.5	Accumulator Container	[Redacted]																					
N/A	N/A	EV 5.5	Accumulator Attachment	[Redacted]																					
YES	NO	EV5.5.18.2	Accumulator Protection	[Redacted]	NA	NA	NA	NA	NA	NA	Steel	Round	25.4	1.60											
YES	NO	EV5.4	Tractive System Protection	[Redacted]	NA	NA	NA	NA	NA	NA	Steel	Round	25.4	1.20											

51 Attachment Checklist (make sure all are included in your report)

52 ✓ Receipt, data sheets or proof for Alternative Materials (T3.3) or for non-steel materials (composite, honeycomb).

53 ✓ Properties for all non-steel materials

54 ✓ Monocoque Laminate Test data and pictures

55 ✓ Holes -4mm drilled in any regulated tubing require proof of equivalency, include area and moment of inertia

56 ✓ IAD JOINT TEST for standard monocoque parts

Read\_Me Version History Rules Clarifications **Cover Sheet** Chassis Pics MaterialData T3.8 Main Hoop Tubing T3.9 Front Hoop Tubing T3.10 Main Hoop Bracing T3.10.5 T3.5 MHOop Brace Spt T3.11 T3

Figure 2.5: SES Cover Sheet.

properties must be derived from physical tests performed by the team instead of online resources.

### 3 Point Bend Laminate Test

The 3 point bend laminate test is used to derive the Young's modulus  $E$  and ultimate tensile strength  $\sigma_{UTS}$  of a composite skin laminate. The test mandates testing a composite panel with specified length and width dimensions as well as a specified panel support span. This test must be repeated for every deviation in panel construction, whether it by skin thickness (i.e. composite ply count) or core height.

### Perimeter Shear Test

The skin shear strength  $\sigma_{shear}$  is derived by performing a shear test. This type of test is akin to a punching shear test for civil concrete structures, and involves penetrating a die through a composite panel. The Formula Student rules dictate the diameter of the penetrating die as well how the panel is supported. Again, repeat tests are mandatory for any panel deviations.

### Tubing and Panel Comparison

In this category there are multiple worksheets, each of which describes the design of each individual primary structure component of the chassis. Either tubular steel dimensions or composite panel material and dimensions may be entered into the worksheet, and by feeding in material properties listed in the material data worksheet, compares the proposed design with a baseline rules compliant design. To meet structural equivalency, the team's design, whether it be an alternative steel tube or a composite panel, must be assessed on six properties:

1. Flexural rigidity
2. Yield tensile strength
3. Ultimate tensile strength
4. Maximum bending load
5. Maximum deflection at baseline steel load
6. Energy absorbed

All but the maximum deflection criteria must exceed the value of the baseline chassis, while the deflection must be lower, in order to be equivalent.

#### Front Hoop Bracing

		Enter construction type <b>Tubing only</b>							
Material Property		Baseline	Your Tube	Your Composite	Your Total	Outer		Inner	
Material type	Steel	Steel	Steel	Composite 1		b (m)	0.1	0.1	
Tubing Type	Round	Round	Round	NA		h (m)	0.002	0.002	
Material name /grade	Steel	Steel	Steel	T3.5_Laminate		A <sub>1</sub> (m <sup>2</sup> )	2.00E-04	I <sub>1</sub> (m <sup>4</sup> )	6.67E-11
Youngs Modulus, E	2.00E+11	2.00E+11	2.00E+11	0.00E+00		A <sub>2</sub> (m <sup>2</sup> )	2.00E-04	I <sub>2</sub> (m <sup>4</sup> )	6.67E-11
Yield strength, Pa	3.05E+08	3.05E+08	3.05E+08	0.00E+00		z <sub>1</sub> (m)	0.001	I <sub>c1</sub> (m <sup>4</sup> )	2.01E-08
UTS, Pa	3.65E+08	3.65E+08	3.65E+08	0.00E+00		z <sub>2</sub> (m)	0.021	I <sub>c2</sub> (m <sup>4</sup> )	2.01E-08
Yield strength, welded, Pa	1.80E+08	1.80E+08	1.80E+08	N/A		Centroid (m)	0.0110	I <sub>c12</sub> (m <sup>4</sup> )	4.01E-08
UTS welded, Pa	3.00E+08	3.00E+08	3.00E+08	N/A					
Number of tubes	1	1							
Tube OD, mm	25.4	25.4							
Wall, mm	1.60	1.6							
Thickness of panel, mm				22					
Thickness of core, mm				18					
Thickness of inner skin, mm				2					
Thickness of outer skin, mm				2					
Panel height, mm (half width across top of chassis)				100					
OD, m	0.0254	0.0254							
Wall, m	0.0016	0.0016							
I, m <sup>4</sup>	8.51E-09	8.51E-09		Tubing Only	8.51E-09				
EI	1.70E+03	1.70E+03			1.70E+03				100.0
Area, mm <sup>2</sup>	119.6	119.6			119.6				100.0
Yield tensile strength, N	3.65E+04	3.65E+04			3.65E+04				100.0
UTS, N	4.37E+04	4.37E+04			4.37E+04				100.0
Yield tensile strength, N as welded	2.15E+04	2.15E+04			2.15E+04				100.0
UTS, N as welded	3.59E+04	3.59E+04			3.59E+04				100.0
Max load at mid span to give UTS for 1m long tube, N	9.78E+02	9.78E+02			9.78E+02				100.0
Max deflection at baseline load for 1m long tube, m	1.20E-02	1.20E-02			1.20E-02				100.0
Energy absorbed up to UTS, J	5.86E+00	5.86E+00			5.86E+00				100.0

Figure 2.6: Panel comparison worksheet for the front hoop bracing structure.

For electric vehicles only, there are additional structural elements for accumulator protection and tractive system protection.

## Impact Attenuator and Attachment

The design and attachment of the vehicle's front impact protection structure, known as the impact attenuator, must also be documented in SES. Critical dimensions of the anti-intrusion plate, attachment point location and type are examples of items to be recorded.

## Primary Structure Attachment

This worksheet only concerns monocoque chassis designs. The rules specify that both the front and rear roll hoop structures must be of metallic construction. The method of attachment for these structures to the monocoque chassis must meet certain strength requirements. Laminate material properties drawn from the material data worksheet is also required.

## Harness Attachments

The harness attachment worksheet is also only relevant to monocoques. Similar to the laminate tests for composite sandwich panels, a physical test must be performed for a representative attachment point of the shoulder harness, lap belt, and anti-submarine belt to demonstrate that it is sufficiently strong enough in the event of a crash.

## Accumulator Container and Attachment

For electric vehicles only, the accumulator container must be sufficiently strong to prevent any damage to the battery cells in the event of a collision. The attachment of the container to the chassis must also be sufficiently strong to not fail in impact.



## Welded Tube Inserts

Any inserts for various attachments of other components that require drilling and welding into steel tubing of the chassis must be documented in this worksheet. Simple calculations must be performed to show that the tube with welded insert meets equivalency to the baseline steel tube for the same six properties as used in the panel comparison worksheets. For the 2019 monocoque chassis this worksheet is no longer necessary to be filled in, however was used frequently in the previous Monash Motorsport steel spaceframe chassis designs.

## Additional Info

Material receipts and data sheets for any non-baseline items must be provided in SES to as proof of the materials used in the manufactured chassis.

## Comparison with SAE

The workflow of the SES document for SAE competitions is largely identical to Formula Student. The only major differences are that the layout is condensed into fewer worksheets, with all the panel comparison worksheets being compressed into one master worksheet; while accumulator and tractive system related items for electric vehicles are placed into a separate EV only SES document.

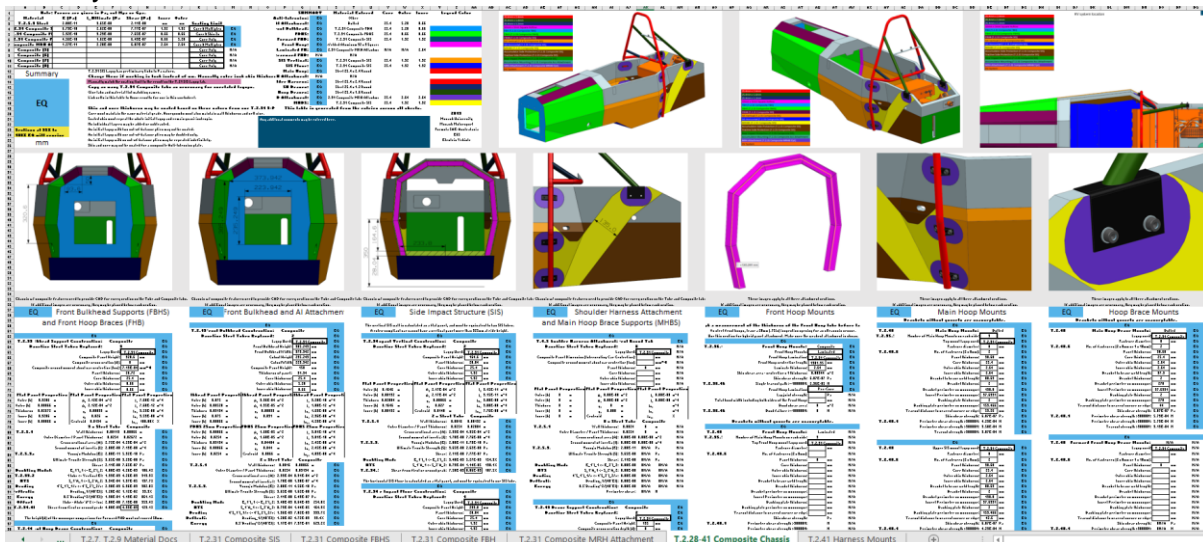


Figure 2.7: The completed SES document for FSAE-A 2019 showing the panel comparison worksheet.

# Chapter 3 Chassis Loads

Chassis stiffness and deformation are important factors when designing a chassis as they affect the responsiveness of the car while in transient states such as cornering [13]. The aim is to create a structure that is stiff enough to adequately distribute the loads so that adjustments made to the suspension setup can be seen on the track. The trade off with adding stiffness is generally mass and the team has conducted points-based analysis to determine where the line lies, as shown in Figure 3.2. The team has found that a value of  $R=3$ , where  $R$  represents the ratio of chassis stiffness to roll stiffness, is the ideal stiffness target.

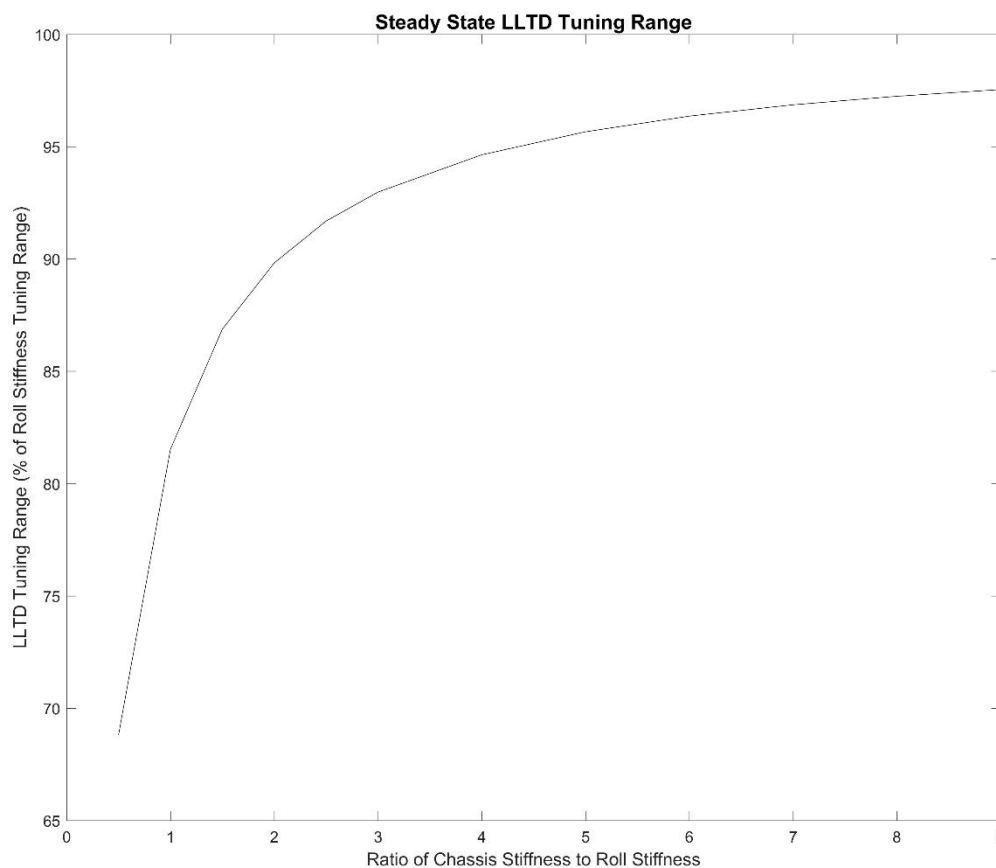


Figure 3.1: Steady State LLTD Tuning Range.

## Chassis Deformation

The chassis sees four main globalised deformation modes, longitudinal torsion, vertical bending, lateral bending and horizontal lozenging (see Figure 3.3).

*Longitudinal torsion* is generally regarded as the most important of the four. Lateral torsion is caused by a moment around the front axle that is as a result of opposite vertical forces that are applied to the front suspension, thus inducing twisting in the chassis. A good example of this is load case. The chassis can be modelled as a torsional spring, if not sufficiently stiff enough changes to the lateral load transfer distribution won't be able to be seen. The *responsiveness* of the car is affected by the lateral load transfer distribution which can most effectively be tuned by adjusting the roll stiffness when the chassis is sufficiently stiff [13] [14].

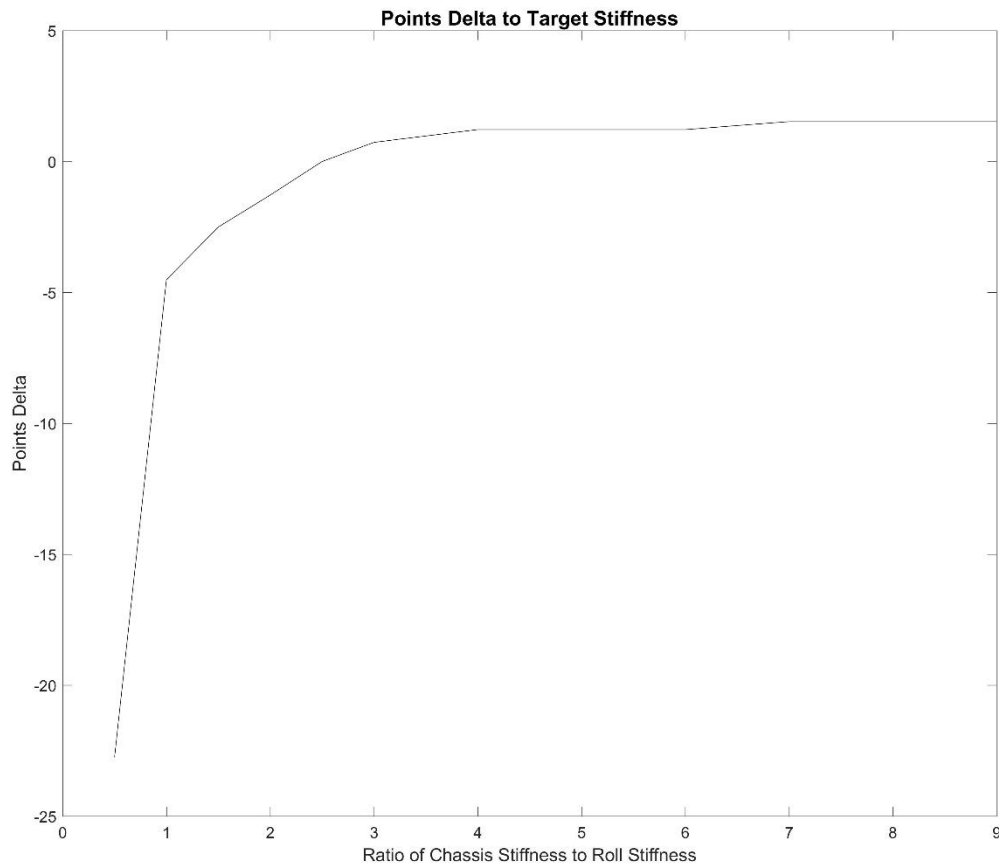


Figure 3.2: Points Delta to Target Stiffness.

This is important because it affects how much grip each tyre has and again how the car handles dynamically [15].

There are both static and dynamic causes for *vertical bending*. Static loads that induce vertical bending are from heavy objects inside the car such as the driver and powertrain package, these create a three point bend. Dynamic loads that can create vertical bending occur during acceleration where the car 'squats' and during braking or deceleration where the car 'dives' [15]. Both of which can be accounted for during suspension setup.

*Lateral bending* occurs during cornering where the centrifugal force at the centre of gravity of the car is balanced by the reacting forces of the tyres on the ground. Lateral bending doesn't play much of an effect on the vehicle dynamics. *Horizontal Lozenging* is a result of uneven forces acting on the left side of the car compared to the right. This can easily occur if one of the front wheels 'grips up' more than the other.

The load case considered of most importance is torsional rigidity, which can be simulated using FEA and validated through physical testing. For both simulation and physical testing, the vehicle is constrained at one of the rear outboards, while the other only has one degree of freedom in the lateral direction. Two point loads are applied at the front outboards in opposite directions, which generates a moment about the centre point of the front hubs. The loading scenario used in physical testing is 800N per outboard, which is replicated in the FEA simulation. An image of the torsion FEA using ANSYS ACP to model the composite sandwich panel in the monocoque is shown in Figure 3.4.

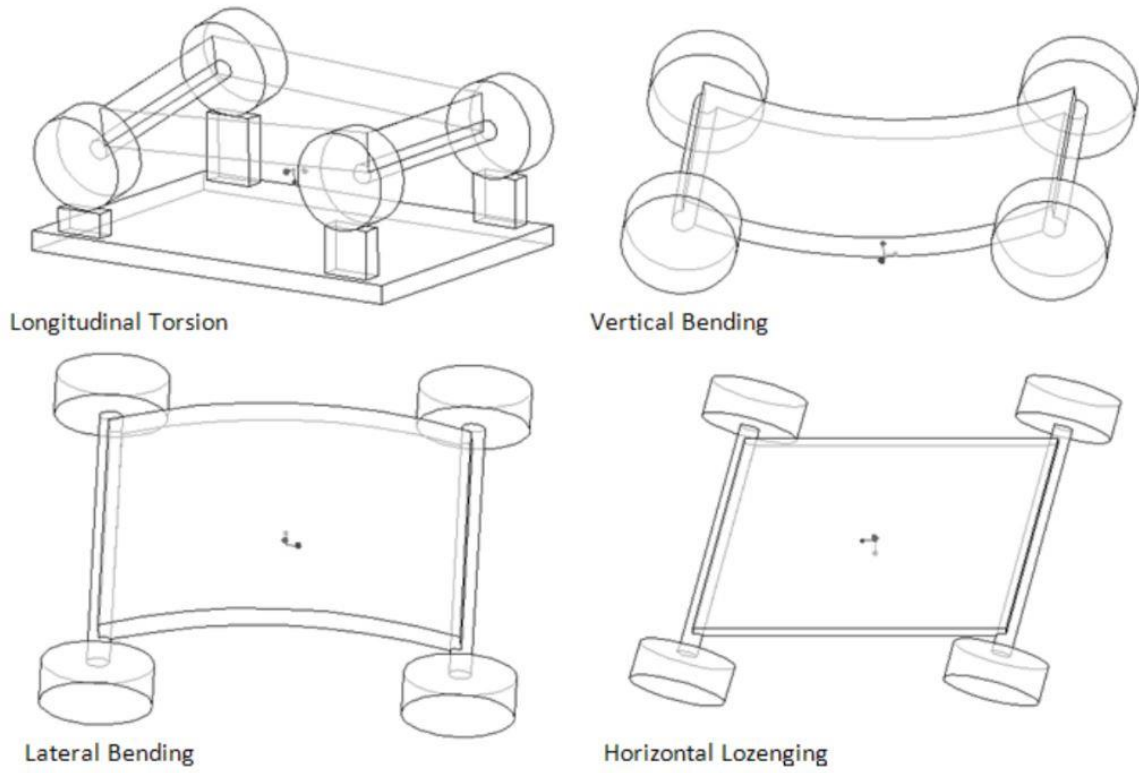


Figure 3.3: Graphical illustration of chassis deformation types. [16]

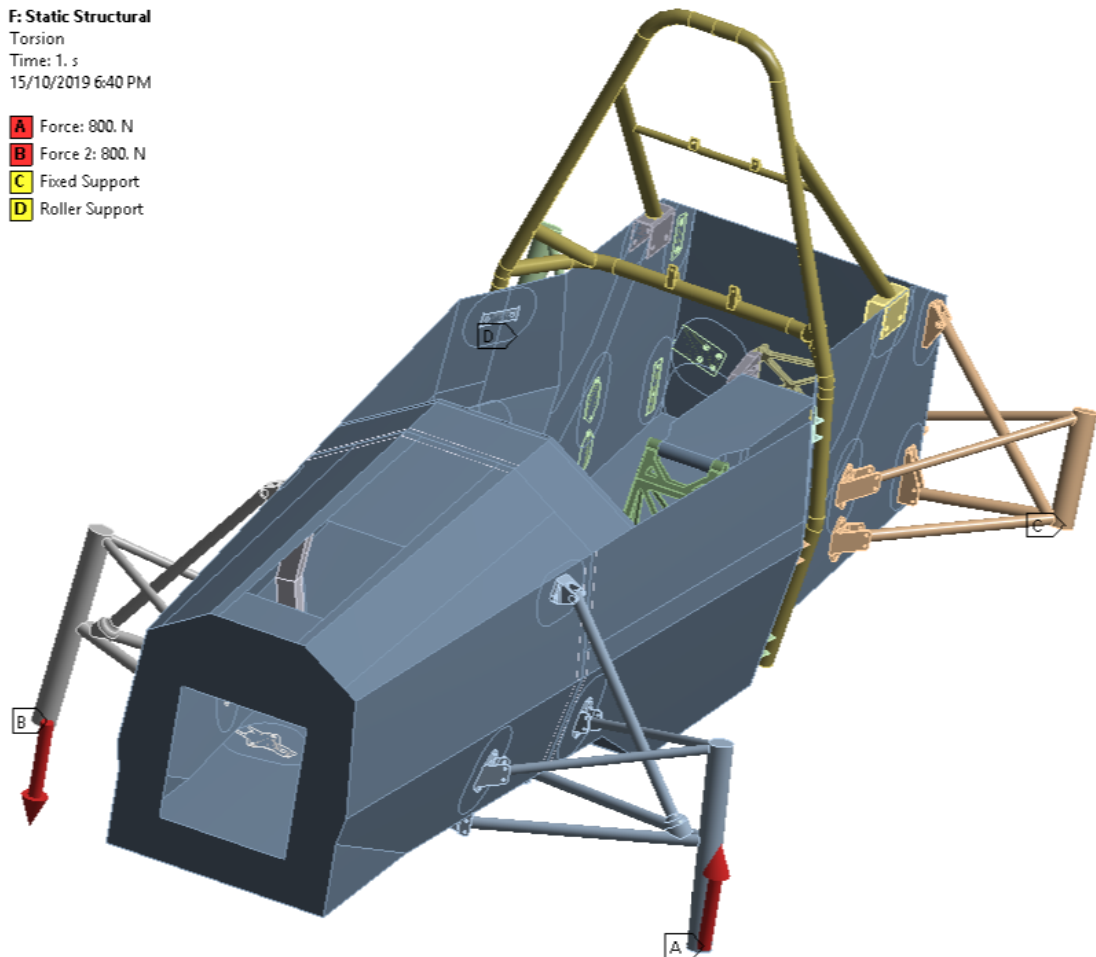


Figure 3.4: Torsion FEA setup in ANSYS.

# Load Cases

In addition to the torsion analysis of the chassis, localised loading from wishbones, the driver and harness attachments, driveline, and the powertrain package will also need to be analysed. The wishbone forces are all documented in the MMS self-developed *The Ring* spreadsheet. An example screenshot of the spreadsheet is shown below in Figure 3.5. The driveline forces are also documented in a self-developed driveline calculations spreadsheet.

*The Ring* was created in order to curb the effect of unrealistic assumptions, loads and boundary conditions that people were using to design suspension components around. The Excel spreadsheet utilizes 3D free body diagrams in order to provide estimates of loads throughout critical points of the suspension. All it requires is the location of the suspension points. The benefit of *The Ring* in comparison to previous analysis of loads is that it is applicable when the car is performing manoeuvres such as braking, accelerating, cornering or even a combination. The spreadsheet has been utilized for many years, providing the team with a great deal of confidence when designing lightweight, strong and durable components.

Geometry, external forces						Solution (forces acting on upright)			Magnitude					
Upper wishbone Outboard		Lower wishbone Outboard		Tie rod/toe link Outboard		Contact patch Location		Upper wishbone						
x	y	z	x	y	z	x	y	z	x	y	z			
1557.2	480.675	345.901	1511.673	490.701	183.257	1626.66	480.69	240.55	x	-694.454		1549.090479	-89.2271	1699.973096
Fore		Fore		Inboard		Force (acting ON CP)		Lower wishbone						
x	y	z	x	y	z	x	y	z	x	y	z			
1250	245	263.74	1250	245	159.96	1550	222.65	174.64	x	1920.263		-235.9246047	-1153.25	2252.346462
Aft		Aft						Tie rod/toe link						
x	y	z	x	y	z	Hub		Downforce (per wheel)						
1540	240	272.66	1480	240	157.33	Outboard		531.6840278						
Upper normal - 3D		Orientation - fore		Hub		Shock		Solution (axial wishbone forces)						
x	y	z	x	y	z	Outboard		Upper						
-2513.03	-21086.466	69881.75	261.673	245.701	23.297	Inboard		Fore		Aft				
Orientation - fore		Unit orientation - fore		Shaft torque		Inboard		1097.578		-2307.723313				
x	y	z	x	y	z	Viewed from outboard		Fore		Aft				
307.2	235.675	82.161	0.727475	0.683071	0.064768	+ value for counterclockwise		-3027		3201.087918				
Unit orientation - fore		Orientation - aft		Orientation - tie/toe		Orientation		Lower						
x	y	z	x	y	z	Unit Orientation		Pushrod						
0.776131	0.59542568	0.207577	31.673	250.701	25.927	0.276613		-1338.515583						
Orientation - aft		Unit orientation - aft		Orientation - hub		0.087657								
x	y	z	x	y	z	Unit Orientation								
17.2	240.675	73.241	0.124687	0.986932	0.102067	0.639273								
Unit orientation - aft		Upper Outboard distance to CP		Orientation - tie/toe		0.276613								
x	y	z	x	y	z	0.931088								
0.068211	0.95445447	0.290455	-7.2	119.325	-345.901	0.237824								
Moment induced by DF		Orientation - hub		Unit Orientation										
x	y	z	Unit Orientation											
			x	y	z									
			0	1	0									
			x	y	z									
			0	1	0									

Figure 3.5: *The Ring* spreadsheet.

Although *The Ring* cannot directly evaluate loads through the chassis but it does output the forces which the linkages will apply to the chassis; these loads are what are used during FEA analysis of the chassis [17].

# Chapter 4 Composite Theory

## Overview

Fibre reinforced polymers, in particular carbon fibre reinforced polymers, possess superior mechanical properties to steel and other metallic materials but only if applied and manufactured in the correct way. Below is some important theory that must be understood before using CFRP as a structural element. The overall modulus of a composite depends on the orientation of the fibres to the load. When both the fibres and resin matrix are loaded together in parallel, they will exhibit greater stiffness and strength compared to loading in a transverse direction. This is evident in Figure 4.1 and Figure 4.2.

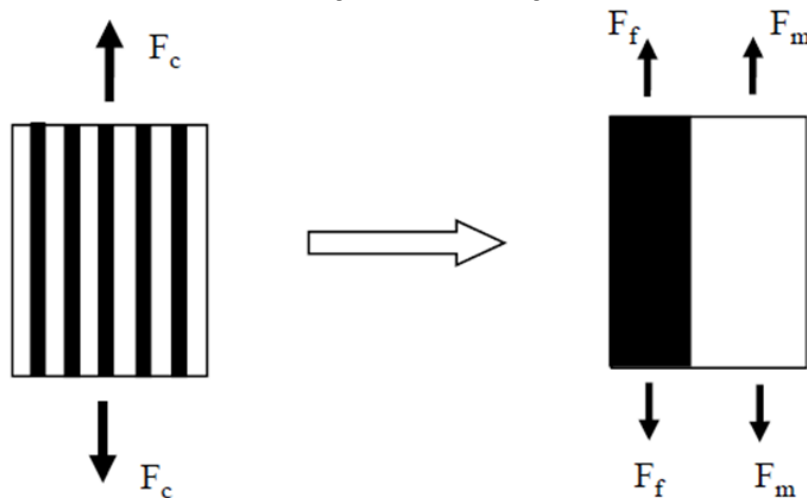


Figure 4.1: Fibre and matrix loading in parallel. [18]

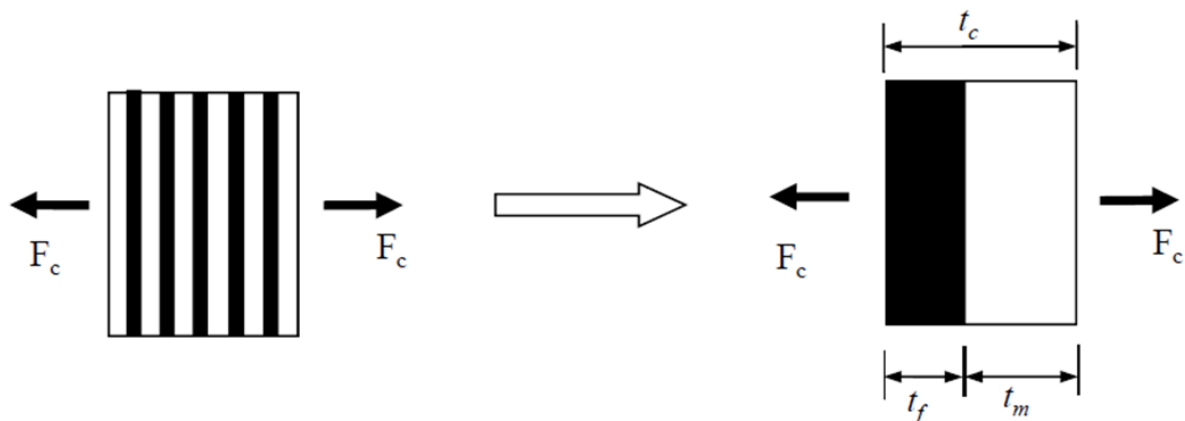


Figure 4.2: Fibre and matrix loading in series. [18]

## Classical Laminate Theory

Classical laminate theory can be used to determine the stresses and strains a laminate will theoretically see under specific loads. A laminate consists of multiple composite plies that have been stacked together in specific orientations in order to improve the overall mechanical properties of the material. It takes into consideration the material properties, orientation and vertical position of each ply to define the elastic properties of the whole laminate. There is a

variation of stress and strain throughout the thickness of the laminate, as can be seen in Figure 4.3. It is this variation that can lead to individual ply failures within a laminate, sometimes resulting in a full laminate failure.

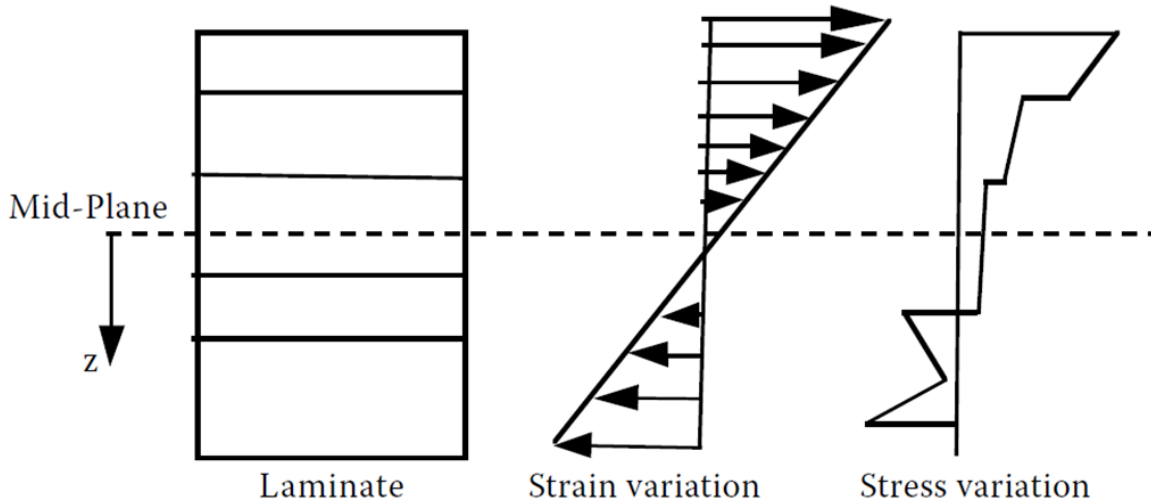


Figure 4.3: Strain and stress variation through the thickness of the laminate. [19]

Because a laminate commonly consists of varied angle laminae, it is necessary to develop stress-strain relationships to work in both a global laminate and local ply coordinate system. Figure 4.4 is a graphical illustration showing the difference in these two coordinate systems. The  $x$ - $y$  coordinate system is known as the global axes, while the 1-2 coordinate system is the local axes. Direction 1 is parallel to the fibre or *longitudinal* direction while direction 2 is perpendicular or *transverse* to the axis of the fibre. The global and local stresses and strains can be related to each other via the transformation matrix  $[T]$ , which is defined as in Equation 4.1. We will make full use of this in the full analysis procedure for a laminate detailed next.

$$[T] = \begin{bmatrix} c^2 & s^2 & 2sc & s^2 & c^2 & -2sc \\ -2sc & -sc & sc & c^2 & -s^2 \end{bmatrix} \quad (4.1)$$

$$c = \cos \theta$$

$$s = \sin \theta$$

$$(4.2a,b)$$

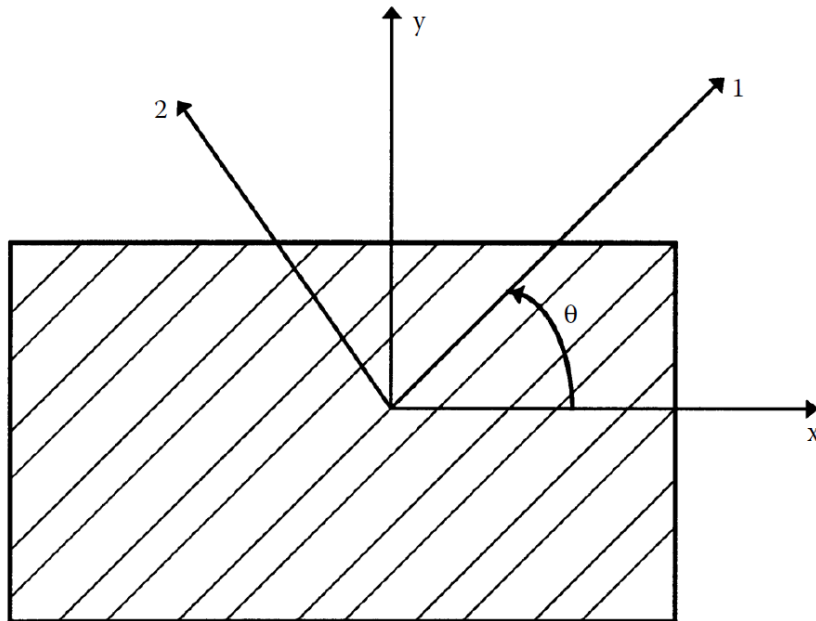


Figure 4.4: Local and global axes of an angle lamina. [19]

## Laminate Analysis Procedure

The general procedure for analysing a laminate [19] can be described as follows:

1. Find the reduced stiffness matrix  $[Q]$  using the four elastic moduli  $E_1$ ,  $E_2$ ,  $\nu_{12}$  and  $G_{12}$ .

$$\begin{aligned} Q_{11} &= \frac{E_1}{1 - \nu_{21}\nu_{12}} \\ Q_{12} &= \frac{\nu_{12}E_2}{1 - \nu_{21}\nu_{12}} \\ Q_{22} &= \frac{E_2}{1 - \nu_{21}\nu_{12}} \\ Q_{66} &= G_{12} \end{aligned} \quad (4.3a-d)$$

2. Find the transformed reduced stiffness matrix  $[\underline{Q}]$  for each ply using and known ply angles.

$$\begin{aligned} \underline{Q}_{11} &= Q_{11}c^4 + Q_{22}s^4 + 2(Q_{12} + 2Q_{66})s^2c^2 \\ \underline{Q}_{12} &= (Q_{11} + Q_{22} - 4Q_{66})s^2c^2 + Q_{12}(c^4 + s^4) \\ \underline{Q}_{22} &= Q_{11}s^4 + Q_{22}c^4 + 2(Q_{12} + 2Q_{66})s^2c^2 \\ \underline{Q}_{16} &= (Q_{11} - Q_{12} - 2Q_{66})c^3s - (Q_{22} - Q_{12} - 2Q_{66})s^3c \\ \underline{Q}_{26} &= (Q_{11} - Q_{12} - 2Q_{66})s^3c - (Q_{22} - Q_{12} - 2Q_{66})c^3s \\ \underline{Q}_{66} &= (Q_{11} + Q_{22} - 2Q_{12} - 2Q_{66})s^2c^2 + Q_{66}(s^4 + c^4) \end{aligned} \quad (4.4a-f)$$

3. Determine the coordinates of the top and bottom surface of each ply consisting of  $n$  plies and from a known ply thickness  $t$ .

Ply 1:

$$h_0 = -\frac{h}{2} \text{ (top surface)}$$

$$h_1 = -\frac{h}{2} + t_1 \text{ (bottom surface)}$$

Ply  $k$ : ( $k = 2, 3, \dots, n-2, n-1$ )

$$h_{k-1} = -\frac{h}{2} + \sum_{i=1}^{k-1} t \text{ (top surface)}$$

$$h_k = -\frac{h}{2} + \sum_{i=1}^k t \text{ (bottom surface)}$$

Ply  $n$ :

$$h_{n-1} = -\frac{h}{2} - t_n \text{ (top surface)}$$

$$h_n = \frac{h}{2} \text{ (bottom surface)} \quad (4.5)$$

4. Generate the three stiffness matrices  $[A]$ ,  $[B]$  and  $[D]$  from  $[\underline{Q}]$  and the known ply coordinates.

$$A_{ij} = \sum_{k=1}^n [(\underline{Q}_{ij})]_k (h_k - h_{k-1}) \quad i = 1,2,6; \quad j = 1,2,6, \quad (4.6)$$

$$B_{ij} = \frac{1}{2} \sum_{k=1}^n [(\underline{Q}_{ij})]_k (h_k^2 - h_{k-1}^2) \quad i = 1,2,6; \quad j = 1,2,6, \quad (4.7)$$

$$D_{ij} = \frac{1}{3} \sum_{k=1}^n [(\underline{Q}_{ij})]_k (h_k^3 - h_{k-1}^3) \quad i = 1,2,6; \quad j = 1,2,6. \quad (4.8)$$

5. Substitute the stiffness matrices and applied forces and moments into Equation 4.9 and solve the simultaneous equations to find midplane strains and curvatures.



$$\begin{aligned} & [N_x \ N_y \ N_{xy} \ M_x \ M_y \ M_{xy}] \\ & = [A_{11} \ A_{12} \ A_{16} \ B_{11} \ B_{12} \ B_{16} \ A_{12} \ A_{22} \ A_{26} \ B_{12} \ B_{22} \ B_{26} \ A_{16} \ A_{26} \ A_{66} \ B_{16}] \end{aligned} \quad (4.9)$$

6. Find the global strains in each ply.

$$[\varepsilon_x \ \varepsilon_y \ \gamma_{xy}] = [\varepsilon_x^0 \ \varepsilon_y^0 \ \gamma_{xy}^0] + z[\kappa_x \ \kappa_y \ \kappa_{xy}] \quad (4.10)$$

7. Find the global stresses in each ply.

$$[\sigma_x \ \sigma_y \ \tau_{xy}] = \begin{bmatrix} Q_{11} & Q_{12} & Q_{16} & Q_{12} & Q_{22} & Q_{26} & Q_{16} & Q_{26} & Q_{66} \end{bmatrix} [\varepsilon_x \ \varepsilon_y \ \gamma_{xy}] \quad (4.11)$$

8. Find the local strains in each ply using  $[T]$ .

$$[\varepsilon_1 \ \varepsilon_2 \ \gamma_{12}/2] = [T] \left[ \varepsilon_x \ \varepsilon_y \ \frac{\gamma_{xy}}{2} \right] \quad (4.12)$$

9. Find the local stresses in each ply.

$$[\sigma_1 \ \sigma_2 \ \tau_{12}] = [T][\sigma_x \ \sigma_y \ \tau_{xy}] \quad (4.13)$$

10. Apply a failure mode criterion to determine if a failure in a composite ply exists. There are a number of different failure theories, however one of the most robust failure mode criteria and the one used in this scenario is the Tsai-Wu failure theory. Here a composite is considered to be safe if the Tsai-Wu constant is less than a value of 1. The Tsai-Wu constant is calculated from a summation of the Tsai-Wu coefficients which are a function of the laminate material properties, in addition to the calculated laminate stresses.

$$H_1 = \frac{1}{(\sigma_1^T)_{ult}} - \frac{1}{(\sigma_1^C)_{ult}}$$

$$H_{11} = \frac{1}{(\sigma_1^T)_{ult}(\sigma_1^C)_{ult}}$$

$$H_2 = \frac{1}{(\sigma_2^T)_{ult}} - \frac{1}{(\sigma_2^C)_{ult}}$$

$$H_{22} = \frac{1}{(\sigma_2^T)_{ult}(\sigma_2^C)_{ult}}$$

$$H_{66} = \frac{1}{(\tau_{12})_{ult}^2}$$

$$H_{12} = -\frac{1}{2} \sqrt{\frac{1}{(\sigma_1^T)_{ult}(\sigma_1^C)_{ult}(\sigma_2^T)_{ult}(\sigma_2^C)_{ult}}} \quad (4.14a-f)$$

$$H_1\sigma_1 + H_2\sigma_2 + H_6\tau_{12} + H_{11}\sigma_1^2 + H_{22}\sigma_2^2 + H_{66}\tau_{12}^2 + 2H_{12}\sigma_1\sigma_2 < 1 \quad (4.15)$$

## Beam Theory for Sandwich Panels

Consider a simply supported sandwich beam of span  $L$  and width  $b$  loaded in 3 point bending with a central load  $W$  per unit width as illustrated in Figure 4.5. The skins each have thickness  $t$  and are separated by a thick layer of honeycomb core of thickness  $c$ .

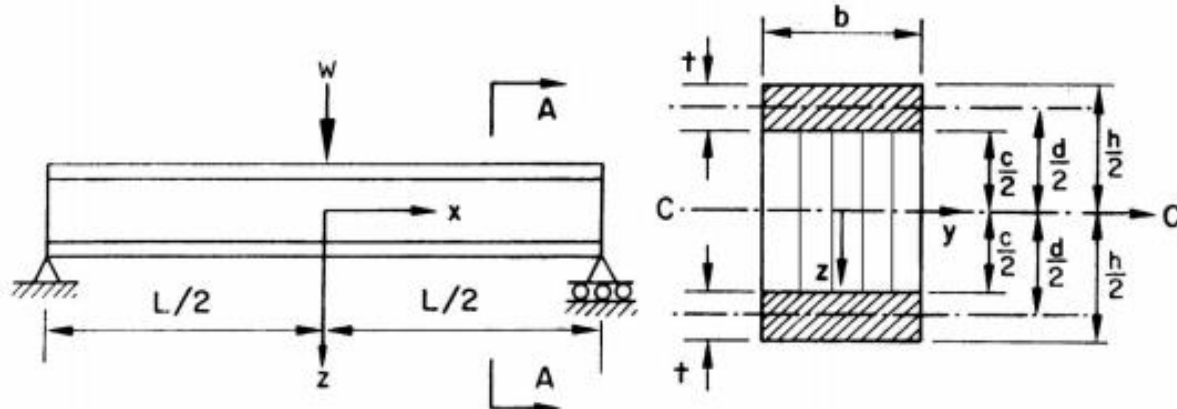


Figure 4.5: (a) Simply supported beam, (b) cross section on A-A [20].

The flexural rigidity  $D$  of the sandwich beam is then given by:

$$D = E_f \frac{bt^3}{6} + E_f \frac{btd^2}{2} + E_c \frac{bc^3}{12} \quad (4.16)$$

where  $E_f$  is the in-plane Young's modulus of the facesheet,  $E_c$  is the core modulus and  $d$  is the distance between the top and bottom facesheet midplanes. The three terms on the right hand side of the equation each correspond to a different rigidity component. They are the stiffness of the facesheet skins about their centroid, stiffness of the facesheet skins about the panel's centroid, and stiffness of the core about the panel's centroid, respectively. The first and third terms in the equation have negligible contributions because the facesheet centroid is extremely small in most cases, as is the core modulus [21]. The flexural rigidity of the sandwich beam can therefore be rewritten as:

$$D = E_f \frac{btd^2}{2} \quad (4.17)$$

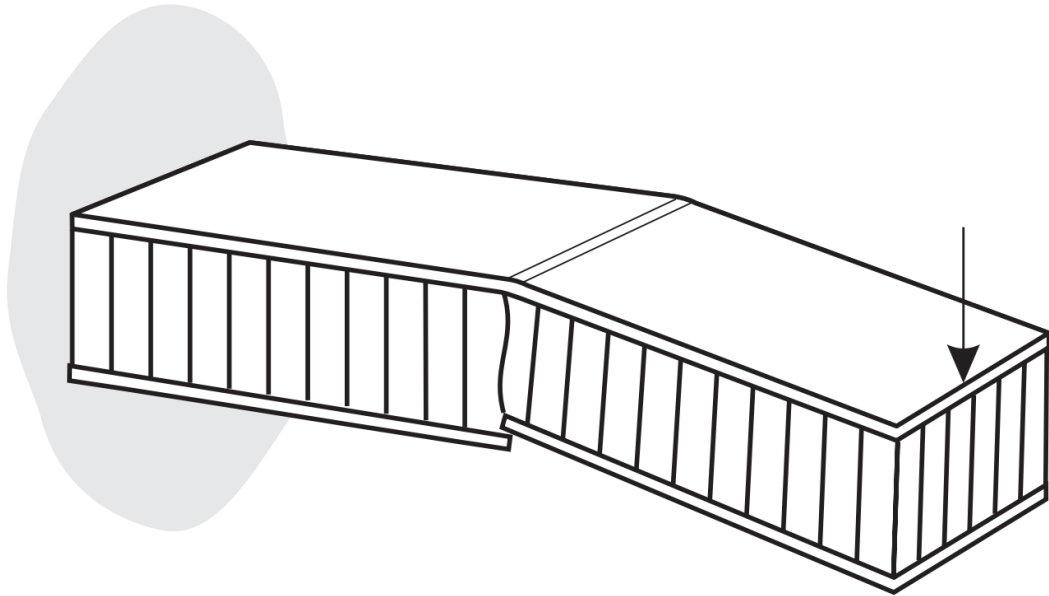
When this equation is combined with the simple mechanics of materials solution for the deflection of a beam at its centre, the panel stiffness in 3 point bending is given as:

$$\frac{W}{\Delta} = 24 \frac{E_f btd^2}{L^3} \quad (4.18)$$

## Failure Loads

The composite sandwich panel can fail in a number of different modes, with the failure modes that are of most importance in designing for the monocoque chassis being as follows.

## Face Yielding



### Skin compression failure

Figure 4.6: Facesheet yielding failure (compression). [22]

Face yielding failure occurs in the top skin when the axial stress in either of the skins reaches the in-plane strength  $\sigma_{fx}$  of the face material for loading along the beam axis. It is assumed that the skin behaves in a brittle manner. The stresses and strains of the facesheet are calculated in the same manner as outlined on pg. , working backwards to find the failure load. The normal load applied onto the facesheet laminate,  $N_x$ , is given by [22]:

$$N_x = \frac{WL}{4hb} \quad (4.19)$$

### Intra-cell Dimpling

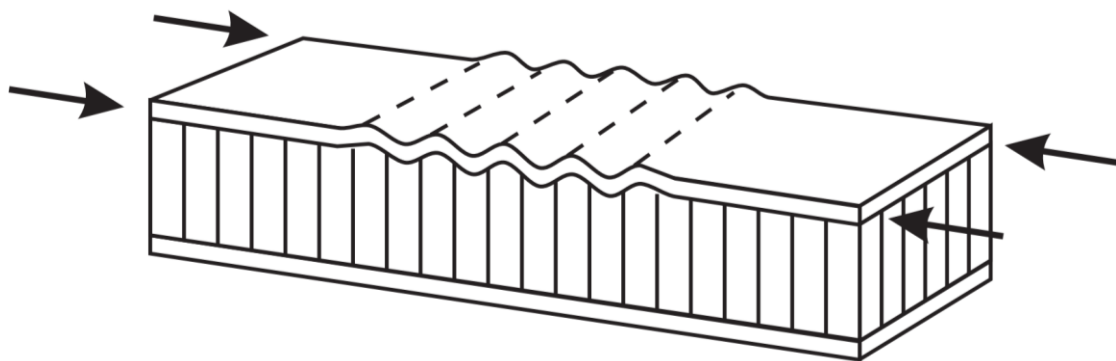


Figure 4.7: Intra-cell dimpling of the facesheet skins. [22]

Intra-cell dimpling failure is the buckling of the face where it is unsupported by the walls of the honeycomb. This type of failure mode can typically be negated or made redundant by reducing the cell size of the honeycomb. The critical normal stress load for intra-cell dimpling proposed by Thomsen and Banks [23] can be expressed as:

$$N_{cr} = \frac{K_{Dimp} D_{22}}{b^2} \quad \text{where}$$

$$K_{Dimp} = \pi^2 \left[ \frac{D_{11}}{D_{22}} \left( \frac{b}{a} \right)^2 + \frac{8(D_{12} + 2D_{66})}{D_{22}} + \frac{16}{3} \left( \frac{a}{b} \right)^2 \right] \quad \text{where } \frac{a}{b} = 0.577 \quad (4.20)$$

## Core Shear

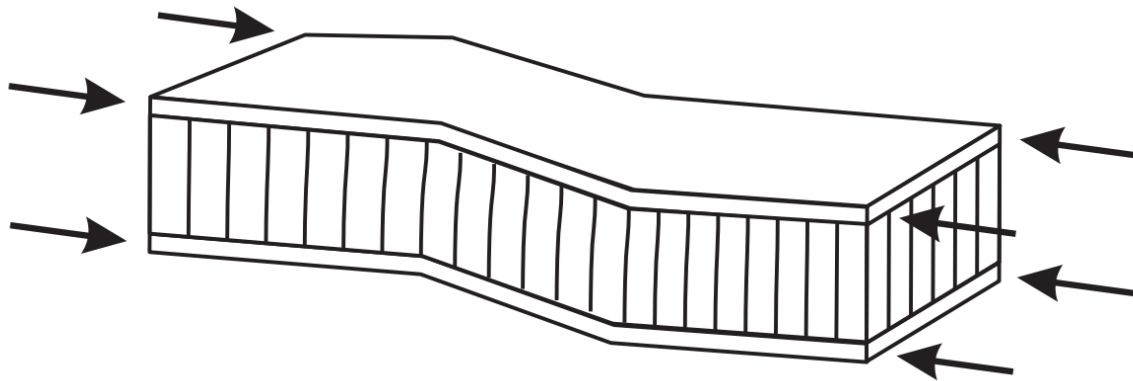


Figure 4.8: Core shear or 'shear crimping'. [22]

Low density Nomex aramid honeycombs are particular susceptible to core shear [20] as discovered in physical tests conducted by MMS dating back in 2015, but are also relevant for other material cores. The critical core shear load  $P_{max}$  is given by:

$$P_{max} = 2F_c hb \quad (4.21)$$

where  $F_c$  is the ultimate shear strength of the core.

## SES Method

As mentioned on pg. , equivalency of a monocoque panel is proven through six parameters as calculated in SES. The calculations for them are detailed below.

### Flexural Rigidity

The flexural rigidity  $EI$  of the panel is calculated from the skin elastic modulus (Pa) as derived from physical 3 point bend laminate tests and the panel second moment of area ( $m^4$ ), which itself is a function of the panel thickness and the effective panel height on the actual monocoque.

$$EI = E_{skins} \times I_{panel} \quad (4.22)$$

### Yield Tensile Strength

The yield tensile strength of the panel (N) is calculated from the skin yield tensile strength derived (Pa) from physical 3 point bend laminate tests and the effective skin cross sectional area ( $mm^2$ ) from given skin thickness and effective panel height on the actual monocoque.

$$F_{yield} = \frac{\sigma_{Y,skins} \times A_{skins\ cross-section}}{10^6} \quad (4.23)$$

### Ultimate Tensile Strength

The ultimate tensile strength of the panel (N) is calculated in the same manner as the yield tensile strength, but using the skin ultimate tensile strength (Pa) derived from physical 3 point bend laminate tests instead.

$$F_{UTS} = \frac{\sigma_{UTS,skins} \times A_{skins\ cross-section}}{10^6} \quad (4.24)$$

## Maximum Bending Load

The maximum bending load (N) at the mid span of a panel is calculated from the skin ultimate tensile strength (Pa), panel second moment of area (m<sup>4</sup>), panel thickness (mm) and panel length (m), in this case equal to 1m.

$$F_{max} = \frac{4 \times \sigma_{UTS,skins} \times I_{panel}}{0.001 \times 0.5 \times t_{panel} \times L} \quad (4.25)$$

## Maximum Deflection at Baseline Steel Load

The maximum deflection (m) of the composite panel is calculated from the maximum bending load (N) of the baseline steel tube, panel length (m), and panel flexural rigidity  $EI$  from earlier.

$$\Delta = \frac{F_{steel,max} \times L^3}{48 \times EI} \quad (4.26)$$

## Energy Absorbed

The panel energy absorption (J) is calculated from the maximum bending load (N) of the panel, panel length (m) and panel flexural rigidity  $EI$ .

$$Energy_{panel} = 0.5 \times F_{max} \times \frac{F_{max} \times L^3}{48 \times EI} \quad (4.27)$$

## Insert Theory

Nearly all of the loads applied onto the monocoque chassis from components such as the wishbones or driver harness attachments can be considered as point loads acting on the faces of the monocoque panels. Unfortunately, a composite sandwich panel is inherently poor at handling concentrated loads due to its very thin skin laminates and thin-walled honeycomb cores. As a result, a method of efficiently transferring these localised loads into the monocoque structure is required, and the most widely used and accepted method is through the use of solid hardpoint inserts embedded into the honeycomb core structure. The basic mechanisms in which these solid inserts can be loaded in a sandwich panel are shown in Figure 4.9 below.

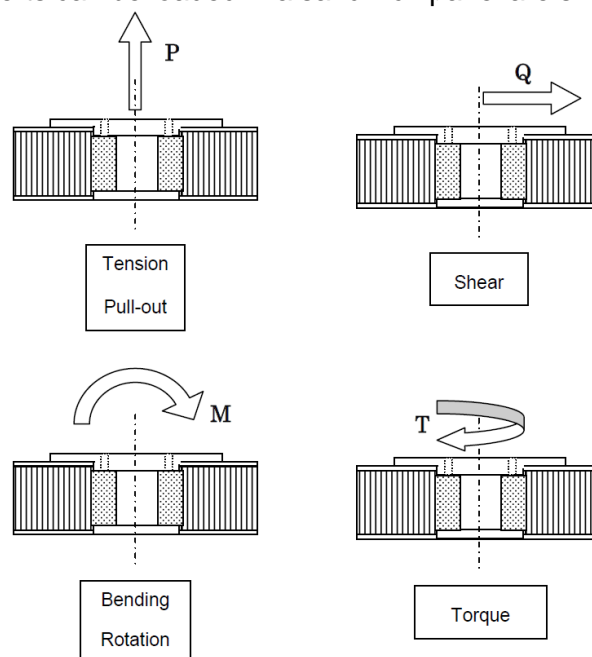


Figure 4.9: Basic types of insert loading. [24]

The strength and load-bearing capability of an insert is affected by both the insert design itself as well as the characteristics of the composite sandwich panel. The skin face sheets and the honeycomb core have different contributions to the overall insert capability under different loading scenarios, as summarised below in Table 4.1.

Table 4.1: Effect of sandwich components on insert load-bearing capability. [24]

Load Type	Contribution of sandwich component to insert load-bearing capability		
	Core	Face sheet	Core/face bond
Tension	High	Medium	Very low
Compression	High	Medium	Low
Shear	Low	High	Very low
Bending	High	Medium	Low
Torsion	High	Low	Low

## Analysis

Much of the literature revolving around insert design is heavily based from the ECSS-HB-32-22A Insert Design Handbook [24]. This handbook documents the basic design guidelines and theory for preliminary insert design, and will be summarised and discussed below.

### Basic Parameters

#### Core Shear Modulus

The core shear modulus affects the way load is distributed from the insert and into the face sheets and core. The greater the core stiffness, the lower the load contribution of the face sheets to the overall insert loading capacity is, and vice versa [24]. The Insert Design Handbook concluded from their own tests that the core shear modulus values provided by manufacturers do not follow any standards and are too high to provide accurate analytical determination of insert strength. Instead, a conservative effective core shear modulus is defined and used for all calculations:

$$G_c = \frac{G_W}{3} \quad (4.28)$$

where  $G_W$  is the core shear modulus in the  $W$  or ribbon direction.

#### Core Shear Strength

Under tensile or compressive loading, the loading capacity of the insert is dictated by the core shear strength. The insert system fails by shear rupture of the core surrounding the insert when the load is transferred from the insert to the core via the potting compound. Both the expansion and ribbon directions of the core foils contribute to the ultimate shear strength, and because in a hexagonal honeycomb core the number of single foils in the L or expansion direction is 72% more than the ribbon direction, an effective core shear strength is defined as follows:

$$\tau_{c \text{ crit}} = 1.36\tau_{w \text{ crit}} \quad (4.29)$$

## Potting Geometry

The potting compound, essentially the bonding adhesive between the insert and the core, has an effective radius that influences the total area that load can be distributed to. This potting radius has a value that is marginally larger than the insert radius, and accounts for the differences in the cell wall geometry of the honeycomb core in the expansion and ribbon directions. Due to the nature of the hexagonal honeycomb core processing, there are double cell walls where two foils are adhered together and are much stiffer and stronger than the single cell walls.

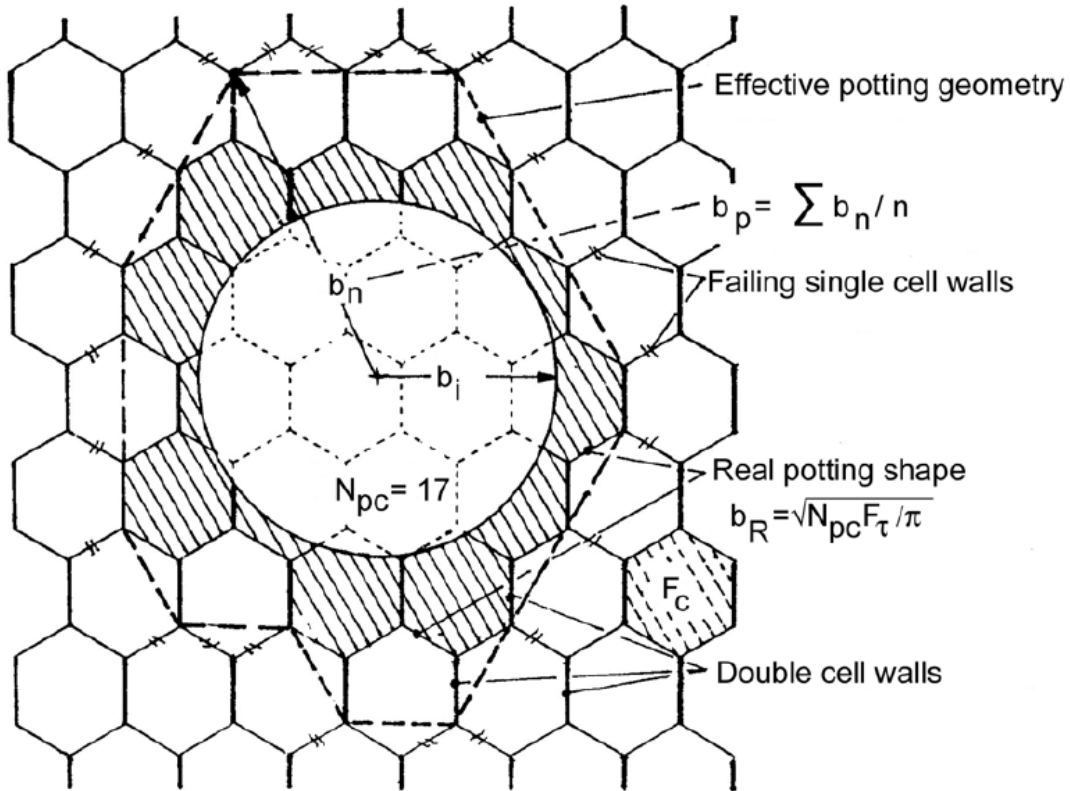


Figure 4.10: Potting Geometry [24]

The effective potting radius  $b_p$  is defined as the average distance of the nearest single cell walls surrounding the potting from the centre of the insert, and is depending on the insert radius  $b_i$  and size of the core cell  $S_c$ .

$$b_p = \frac{1}{n} \sum b_n \quad (4.30)$$

Additionally, a minimum effective potting radius  $b_{pmin}$  is obtained for a certain position of the insert centre within a hexagonal honeycomb cell. This value gives the greatest margin of safety and is the most conservative value for calculations.

$$b_{pmin} = 0.93192b_i + 0.874S_c - 0.66151 \quad (4.31)$$

## Out-of-plane Loading

As previously mentioned, under out of plane loading, the insert system fails by shear rupture of the core surrounding the insert. The shear stresses in the potting compound bonding the core to the insert is typically higher than it is at the core, however guidelines dictate that the chosen potting compound will have its maximum shear strength capability to be higher than

the core, and so failure will therefore always occur at the core interface and typically with the single foil cells. The core shear stress  $\tau_{cmax}$  calculation is performed as follows:

$$\tau_{cmax} = \tau_c(r = b_p) = \frac{P}{2\pi b_p d} \quad (4.32)$$

Failure of the insert system occurs when the core shear stress reaches the critical effective core shear strength.

$$P_{crit} = 2\pi b_p d \tau_{ccrit} \quad (4.33)$$

## In-plane Loading

Under in-plane loading scenarios, the honeycomb core is unable to transfer any stresses, and so all of the in-plane loads are carried by the face sheets. There are four in-plane failure modes for CFRP face sheets that must be accounted for, as discussed below.

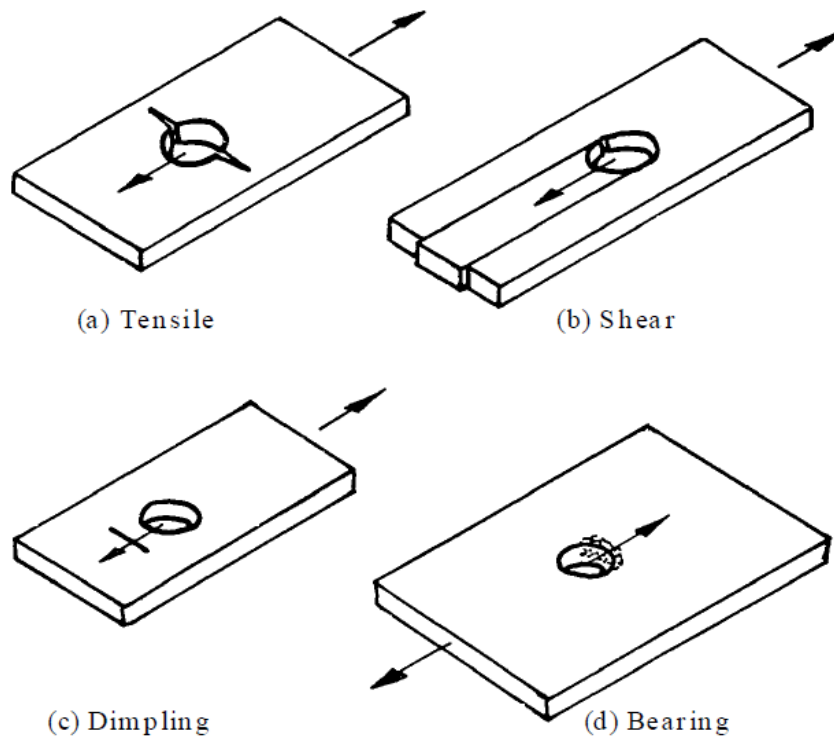


Figure 4.11: Failure modes of CFRP face sheets. [24]

### Tensile Failure (Tension)

A tensile failure can occur in a large panel with a sufficiently large edge distance. The failure occurs locally at the edge of the hole. The basic equation for the maximum in-plane load  $Q_t$  against failure in tension is:

$$Q_t \leq \frac{1}{K'_e} (w - b_i) t_s \sigma_{t,ult} \quad (4.34)$$

where:

$K'_e$	stress concentration factor
$w$	panel width
$b_i$	insert diameter (also denoted as $d$ )
$t_s$	face sheet thickness
$\sigma_{t,ult}$	UTS of face sheet
$e$	edge distance



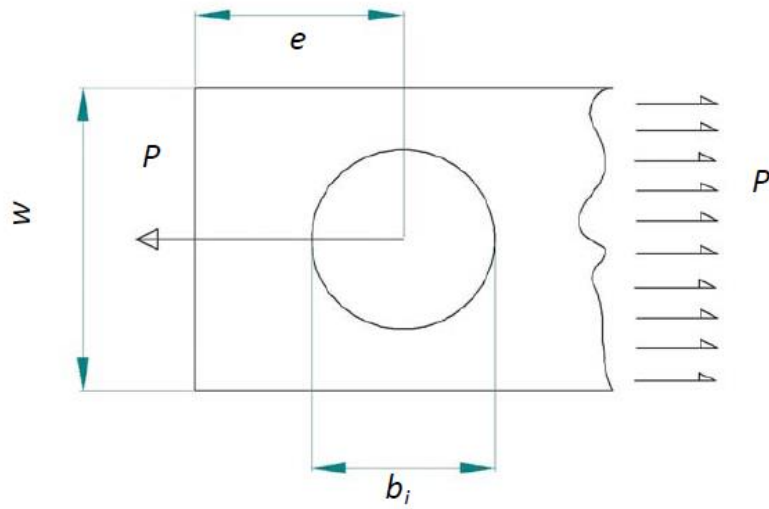


Figure 4.12: Nomenclature for ultimate in-plane load against tensile failure. [24]

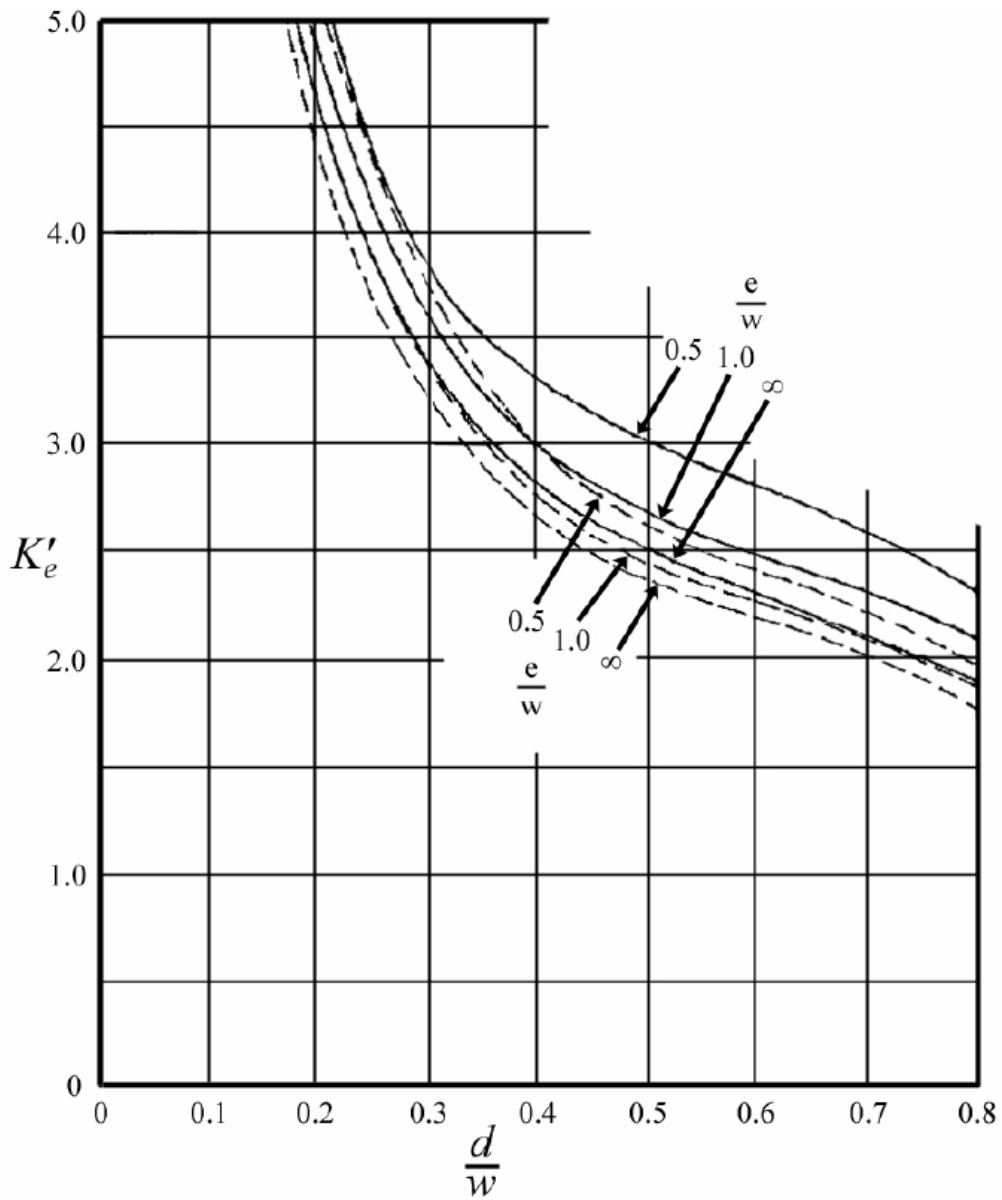


Figure 4.13: Stress concentration factor. [24]

### Shear Out Failure (Tension)

The shear out failure occurs in panels with small edge distances and can be at any angle of the face sheet laminate. The basic equation for the maximum in-plane load  $Q_s$  against shear-out failure is:

$$Q_s \leq 2t_s \left( e - \frac{b_i}{2} \right) \frac{1}{\cos \alpha \cos \alpha} \tau_s \quad (4.35)$$

where:

- $\alpha$  angle of failure direction
- $\tau_s$  CFRP in-plane shear strength

### Dimpling Failure (Compression)

Dimpling or buckling of the facesheet can occur under compression loading. It typically doesn't lead to failure under the amplitude of the dimples become very large in a phenomenon known as wrinkling. The equation to calculate the maximum in-plane load  $Q_d$  at which dimpling occurs is an empirically derived expression, and is given as:

$$Q_d \leq \frac{2}{\pi} b_p t_s K_D \frac{E_s}{1 - \nu_s^2} \left( \frac{t_s}{S_c} \right)^2 \quad (4.36)$$

where:

- $b_p$  typical potting radius
- $t_s$  face sheet thickness
- $E_s$  Young's modulus of CFRP face sheet
- $\nu_s$  Poisson's ratio of CFRP face sheet
- $S_c$  core cell size
- $K_D$  dimpling coefficient (empirical value of 2.0)

### Bearing Failure (Tension or compression)

Bearing failure is typically non catastrophic in a composite structure and occurs when both the edge distance and panel width are very large compared to the insert diameter. Nevertheless, it is still calculated and the basic equation for the maximum in-plane load  $Q_b$  against bearing failure is:

$$Q_b \leq K_b \frac{2}{\pi} b_i t_s \sigma_{comp} \quad (4.37)$$

where:

- $K_b$  coefficient (empirical value of 2.2)
- $b_i$  insert diameter
- $t_s$  face sheet thickness
- $\sigma_{comp}$  ultimate compressive strength of face sheet

### Bending or Torsional Loading

The Insert Design Handbook does not recommend the usage of single inserts under bending or torsional loads. Rather insert groups converting the loads to tension or compression are preferred. Where this is not possible, it is recommended that the footing area of the part attaching to the panel be as large as possible and at least as large of the potting diameter of the insert. The critical bending load  $M_{ss}$  and torsion load  $T_{crit}$  are given as:

$$M_{crit} = P_{crit} b_i \quad (4.38)$$

$$T_{crit} = 4\pi b_R^2 t_0 \tau_{0crit} \quad (4.39)$$

where:

- $P_{crit}$  critical out-of-plane load from (insert eq from Out-of-plane loading)
- $b_i$  insert diameter
- $b_R$  real potting radius
- $\tau_{0crit}$  effective core shear strength

## Total Loading Capacity

It is highly unlikely that loads applied onto the monocoque are all purely out-of-plane, in-plane, bending or torsion loads. It is therefore necessary to develop a relation to find the total loading capacity of the insert under combined loading scenarios.

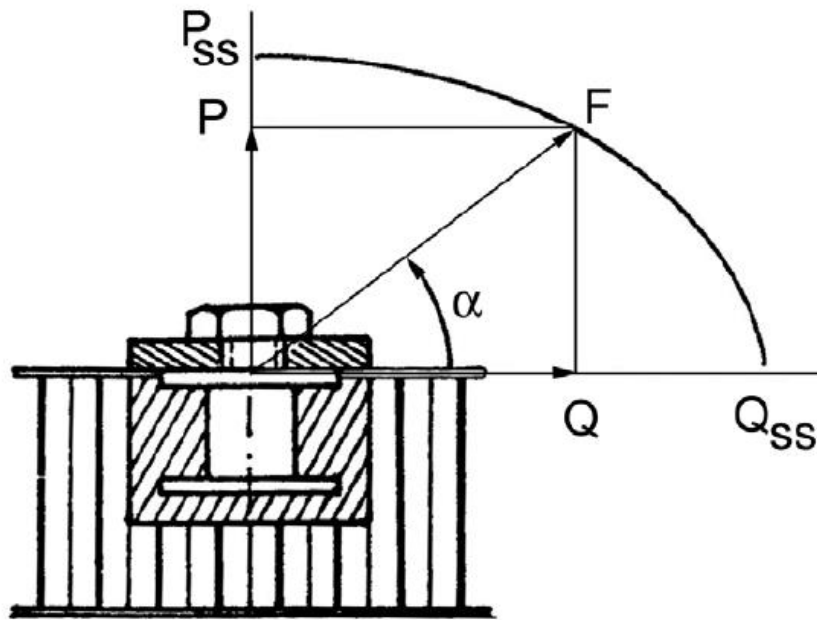


Figure 4.14: Insert subjected to combined loading. [24]

The total capacity of an insert can be expressed as:

$$\left(\frac{P}{P_{SS}}\right)^2 + \left(\frac{Q}{Q_{SS}}\right)^2 + \left(\frac{M}{M_{SS}}\right)^2 + \left(\frac{T}{T_{SS}}\right)^2 \leq 1 \quad (4.40)$$

where the denominator in each term is the maximum permissible load for that loading scenario.

## Insert Groups

There will be situations on the monocoque where it is either desired or necessary for insert groups to be used for the attachment of components. Because there will be stressed inserts in close proximity to each other, a reduction in the static strength capability must be applied to compensate for this. For two inserts loaded in the same direction, the load capacity is given as:

$$P_{SS1}^* = \eta_{IS1} P_{SS1} \quad (4.41)$$

where:

- $P_{SS1}^*$  reduced load capacity of insert 1 due to insert 2
- $\eta_{IS1}$  interference coefficient of insert 1 when loaded in conjunction with insert 2
- $P_{SS1}$  initial load capacity of insert 1 in isolation

When the two inserts are grouped close together, the interference coefficient is given as:

$$\eta_{IS1} = \frac{\frac{b_{p1}}{b_{p2}}}{1 + \frac{b_{p1}}{b_{p2}}} \left( 1 + \frac{a}{5b_{p1}} \frac{1}{1 + \frac{b_{p1}}{b_{p2}}} \right) \quad (4.42a)$$

when:

$$a \leq 5(b_{p1} + b_{p2}) \quad (4.42b)$$

where:

- $b_{p1}$  effective potting radius for insert 1
- $b_{p2}$  effective potting radius for insert 2
- $a$  distance between insert centres

For insert distances greater than the condition in Equation 4.42b, the influence of both inserts on each other is negligible.

Other insert load capacity reduction expressions are given for scenarios such as two inserts loaded in opposite directions, series of inserts, equal or equidistant inserts etc. These will not be discussed here but are available from the Insert Design Handbook.

# Chapter 5 Design

## Design Goals

The monocoque chassis has a number of design goals that it must meet to function as the team requires it to for 2019. These are outlined below.

### Concept Requirements

The chassis must conceptually function as the skeleton to which all vehicle components mount to, in particular the suspension, powertrain, driver controls and the driver itself. It must also adhere to safety requirements such as protecting the driver in the case of crash or rollover scenario, and allow the driver an easy egress in the case of an emergency evacuation. The 2019 chassis is to place more of a focus on the aerodynamics of the car requiring specific geometries that would exploit a high downforce aerodynamics concept. As MMS has to design and manufacture for two cars with different powertrain packages, it is heavily desired for them to have as many common parts as possible to reduce the burden of manufacturing and for ease of spare parts and maintenance. This desire is no different for the chassis.

### Assembly Requirements

The focus around the monocoque assembly is to allow easy access to critical components that require frequent service checks and maintenance. These include but aren't limited to the pedal assembly, engine, drivetrain and accumulator. The cockpit opening area must be sufficiently large enough for the accumulator to be easily removed and placed back in as well as to ensure drivers can get in and out of the vehicle easily.

### Performance Targets

Performance plays a huge part in the design of any race car and it is no different for M19-C and M19-E. A mass target of 35kg or less was set for both monocoques, including roll hoop structures. This target was set with the intent to match or better (i.e. decrease) the weight of the previous year's steel spaceframe chassis, and not create a detrimental effect on the overall performance of the vehicle in comparison to the year before. Another key performance target that was set was the hub-to-hub installation stiffness (i.e. torsional stiffness) to be greater than 3300Nm/deg. This target is carried over from the previous spaceframe target, which was determined through previous analysis conducted by the team that found that the optimum installation stiffness factoring in mass for a steel spaceframe chassis was approximately twice that of the suspension roll stiffness. This is to ensure an adequate response from front to rear tyres during cornering. The *responsiveness* of the car is affected by the lateral load transfer distribution which can most effectively be tuned by adjusting the roll stiffness when the chassis is sufficiently stiff [13] [14]. Lastly, the ease of manufacturing has been considered as a performance target. This is because time is a valuable and limited resource that every Formula Student team must take into account when making high level design decisions. To minimise the time needed to manufacture the monocoques the team would utilise standard chassis inserts, simple mould design and construction, and a full monocoque design with near identical designs for both cars.

## Design Constraints

The high downforce aerodynamics concept for 2019 is the major influencer on the geometry of the monocoque. Design features such as narrowing the chassis to allow for more side airflow, raising the nose to channel more flow to the underbody, and raking the rear floor are just some notable features that can improve the potential of the vehicle aerodynamic package. However, there are a number of constraints placed on the geometry that are non-negotiable, as explained in detail below.

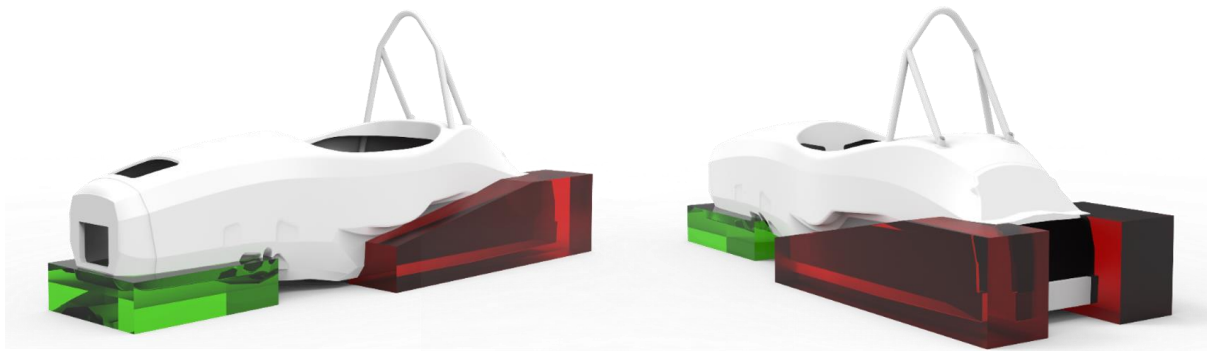


Figure 5.1: Exploitation of monocoque geometry by TUFast for a high downforce aerodynamic package. [25]

## Rules Constraints

As alluded to on pg. , there are a number of primary structure elements that must feature in the monocoque chassis. The most limiting in terms of geometry is the side impact structure which has specified minimum panel heights that must be fulfilled in the design. The minimum volume in the driver footwell and cockpit are dictated by the cockpit templates that must be allowed to be passed through unobstructed. The minimum width of the chassis at the rear is also constrained by a minimum main hoop width of 380mm which is only specified for FSAE.

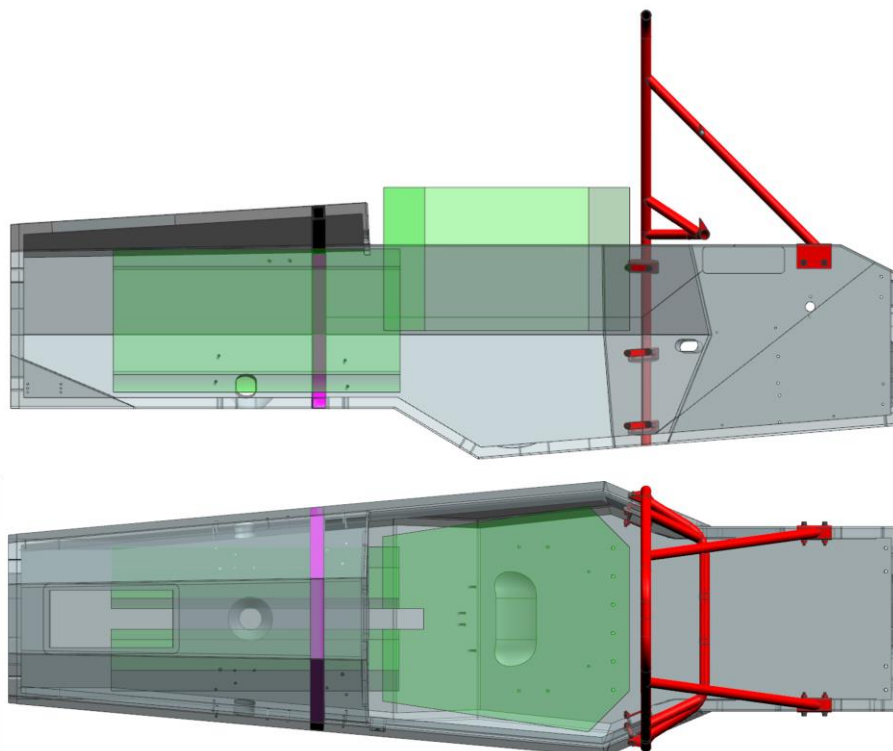


Figure 5.2: Side view (top) and overhead view (bottom) showing cockpit template clearance.

## Powertrain Packaging

The two different powertrain packages, combustion and electric, pose different constraints and design challenges for the rear of the chassis. On one hand, the KTM 690 Duke engine is one of the largest (and tallest) single cylinder combustion engines found in Formula Student, while on the other hand the electric powertrain with its large accumulator energy cell storage container is both long and wide. Accommodating for both in the same design chassis required careful thought and planning. For the previous iteration of chassis this was achieved with a wide rear subframe with no raking for the undertray.

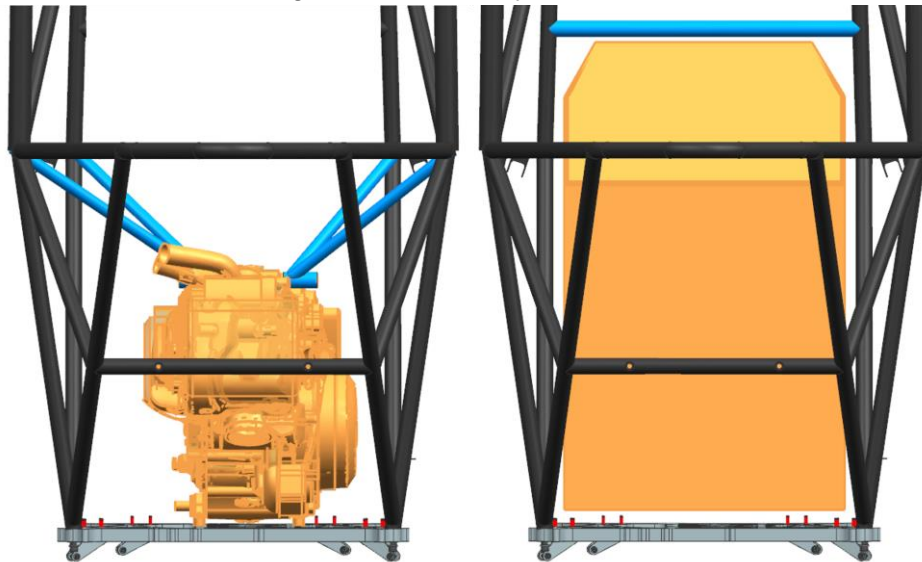


Figure 5.3: Packaging of the combustion and electric powertrains in the 2017 chassis design.

For 2019 with the aim of introducing the raked chassis at the rear whilst still keeping the CG of the KTM 690 as low as possible, the majority of the panel thickness in the floor below the engine has been removed, leaving only a thin walled skin laminate and an access/drainage hole. The height of the engine and its proximity to the shoulder harness mounting position also resulted in an exposed section at the top, with the shoulder harness mounting achieved with a braced bent tube welded to the main hoop. If the engine was not as tall, it would have been possible to use a composite sandwich panel for the shoulder harness mounting. The driveline system remains on the exterior of the chassis to reduce the overall monocoque length.

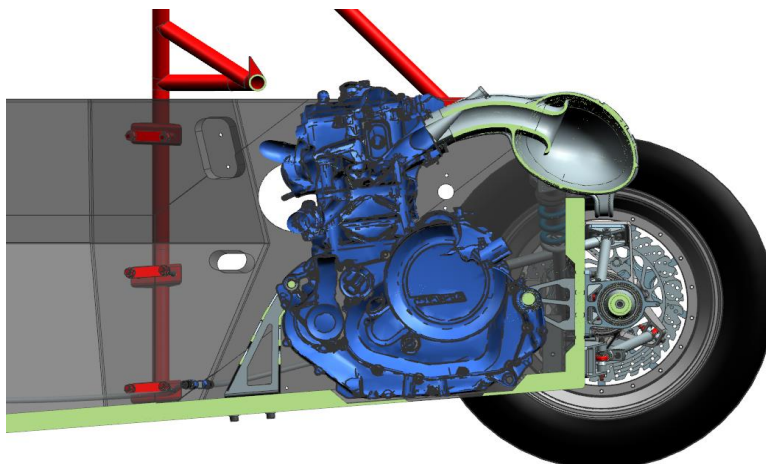


Figure 5.4: Packaging of the KTM 690 and driveline.

The electric powertrain was the limiting factor in determining the minimum width of the rear of the monocoque. To reduce the overall length of the chassis the entire tractive system, including the motor and accumulator, is repositioned to be forward of the driveline system, as opposed to the previous iteration where a rear cage structure was bolted on the rear of the subframe to act as rear tractive system protection. The accumulator, which is mounted to the monocoque through the floor, fits snugly in the rear of the monocoque, and fully envelopes itself around the motor to best utilise the internal space of the monocoque. As a result, the driveline is able to share the same configuration as the combustion car.

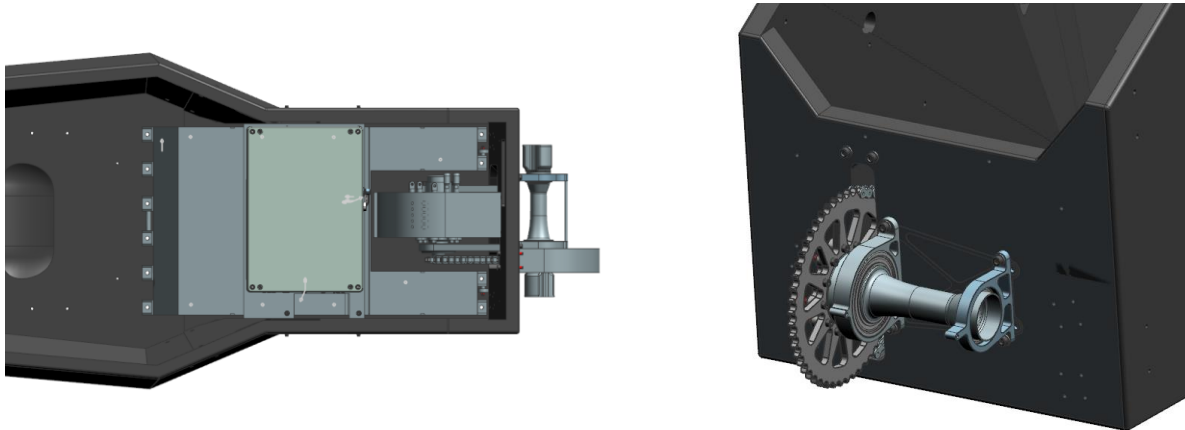


Figure 5.5: Overhead view (left) and rear isometric view (right) of electric powertrain packaging.

## Suspension Packaging

The role of the suspension in a racing car is very critical to overall performance. The geometry of the suspension and where it attaches to the chassis, the link between the front and rear axles, has a direct effect on the vehicle handling. Key parameters such as roll centre heights, camber gain in roll and VSALs must have goals set and targeted in the design. In 2019, a move to a new tyre compound and manufacturer (13" Goodyear D2704 from 10" Hoosier R25B), combined with the new high downforce aerodynamics goals saw a complete rework of suspension geometry.

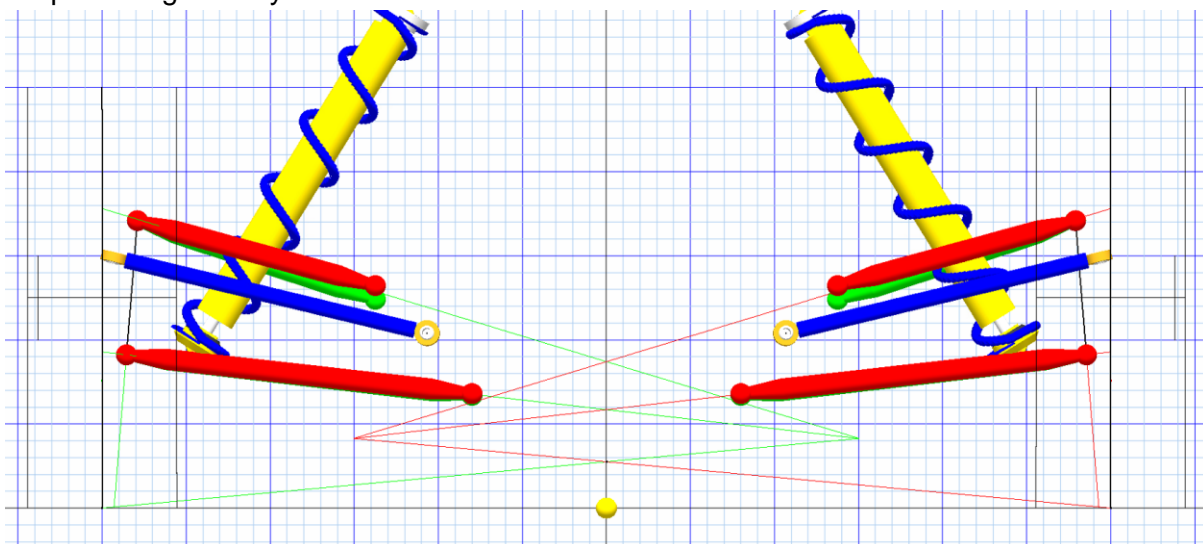


Figure 5.6: M19 front suspension geometry as modelled in Susprog, a kinematic suspension design and analysis tool.



The majority of the work was emphasised on the front suspension geometry, which with the raised nose for aerodynamic reasons would result in significantly higher roll centre heights. To keep the front roll centre height within allowable upper limits, the decision was made to put the lower wishbone mounting points on the underside of the monocoque floor, which also worked favourably with transferring the forces from the wishbone into predominantly in-plane loading on the monocoque panel. The main goal for the steering geometry was to maintain and carry over a zero scrub radius from the previous geometry. To cater for this, the optimal steering rack location was situated inside the monocoque and wishbone A-arms. Were it possible it would have been advantageous from a driver packaging perspective to position the steering rack outside of the monocoque for easier clearance of cockpit templates, however this was a necessary compromise in the 2019 design.

As for the rear of the vehicle, the mounting locations of the fore wishbones were moved rearwards and off the main hoop as was the case in steel spaceframe chassis designs, allowing for more activities for side aerodynamics and cooling componentry.

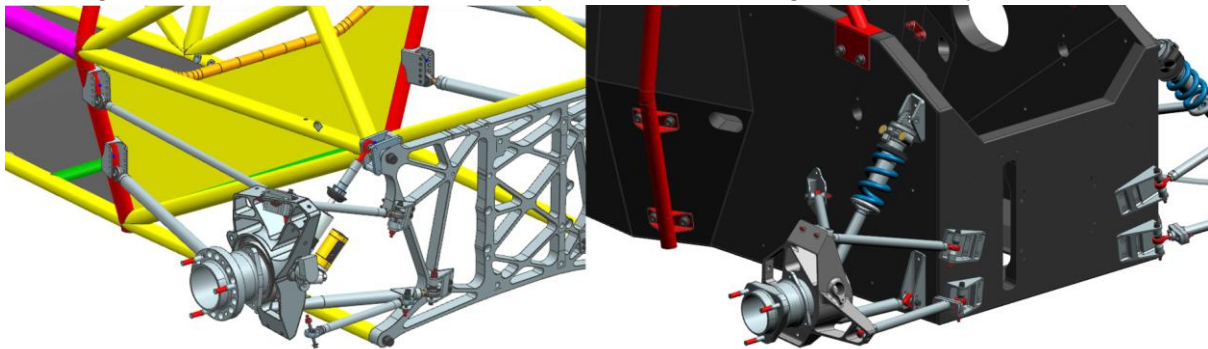


Figure 5.7: Changes in rear suspension packaging with 2017 (left) and 2019 (right).

## Driver Ergonomics

One of the downfalls of the 2017 chassis package was the different ergonomic configurations between the combustion and electric vehicles. The ergonomic package that was tested on a rig with driver input was only implemented on the combustion vehicle, with the electric vehicle having the driver positioned approximately 50 mm further forwards due to packaging interference with the inverter and accumulator. The intent was to create an ergonomics package that is the same across both cars. Given that the electric powertrain is inherently longer due to the need to package the accumulator (making the accumulator shorter and wider poses more issues with suspension geometry and room for aerodynamic performance) the seat back angle needed to be adjusted in order to increase packaging space.

Between 2015 and 2018, the seat back angle was set at 37°, a reclined seating position. From our own driver feedback after driving the TUfast eb2018 car, which featured a much more upright driving position, they were able to have a much better field of view of both the car and the track. The main selling point was the ability to see the outside edge of the front wing allowing for pinpoint positioning of the car around tight corners or slaloms, something that is much more difficult to do in the Monash cars. The reason why Monash had the seat back angle set in a reclined position in the first place was a) to lower the centre of gravity and b) to increase flow to the rear wing due to the driver's head positioned lower in the car. In 2015, research and testing into this by McIver and Paine [26] saw only an 8 point increase moving from a back angle of 43° to 37°.



Figure 5.8: MMS endurance drivers in the TUFast eb2018 during 2018 driver swap.

In order to package the accumulator, an upright seat back angle of  $50^\circ$  has been implemented. Doing so moves the driver's torso and head further forward, providing crucial packaging space. It also allows for the shoulder harness to be mounted in a much better position that will satisfy rules (in the 2017 chassis the harness position barely passed for our tallest driver). The original argument that lowering the back angle and driver's head would increase rear wing flow and therefore better performance is not lost on this upright seating position concept either. With the driver further forward, the headrest is also allowed to move further forward, and hence the rear wing is allowed to be longer. This allowed for a larger mainplane as well as longer endplates, both of which serve to increase rear wing performance.

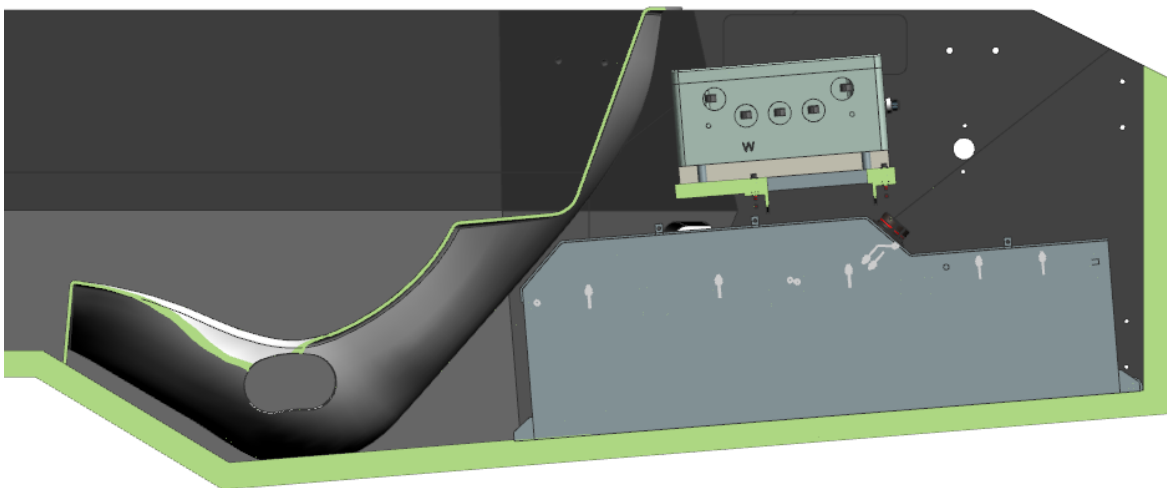


Figure 5.9: Clearance between seat and accumulator.

Figure 5.10 is an image showing the increased packaging space available with an upright seating position. The seat is the old seat back angle while the 2D sketch represents our shortest and tallest drivers with the new seating position. It can also be noted the extra space behind the headrest where the rear wing can now be positioned, a distance of approximately 165 mm.

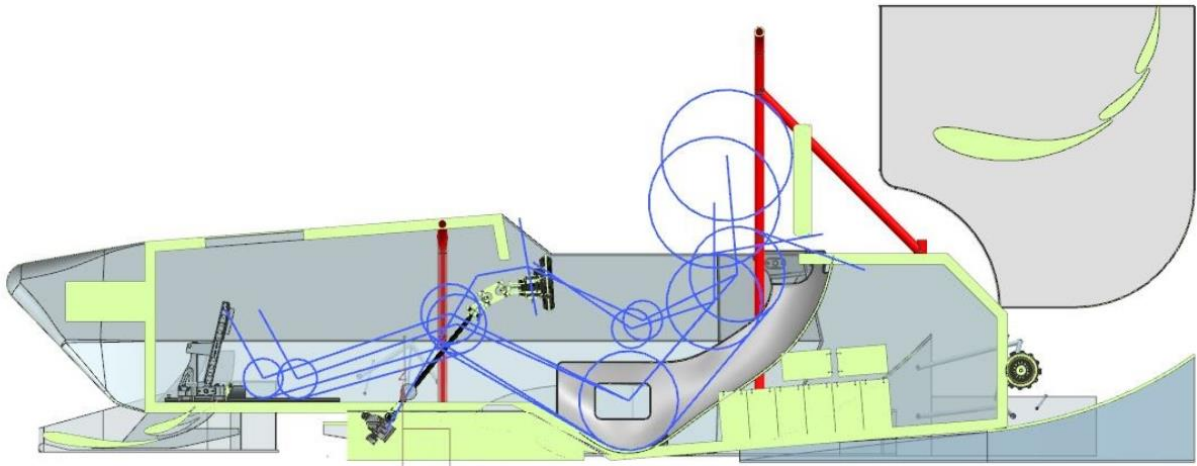


Figure 5.10: Early concept comparison of driver seating position.

The steering wheel and pedal box positions have also changed slightly with the high nose concept and were tested on a bench rig with a driver. It was found that the pedal box height had no impact on comfort, only potential egress issues but that can be worked around with practice and the drivers getting used to the new position. The steering wheel would have to be positioned a bit further forwards and upwards since the torso and the shoulders are further forwards and upwards, but again there was no loss in comfort.

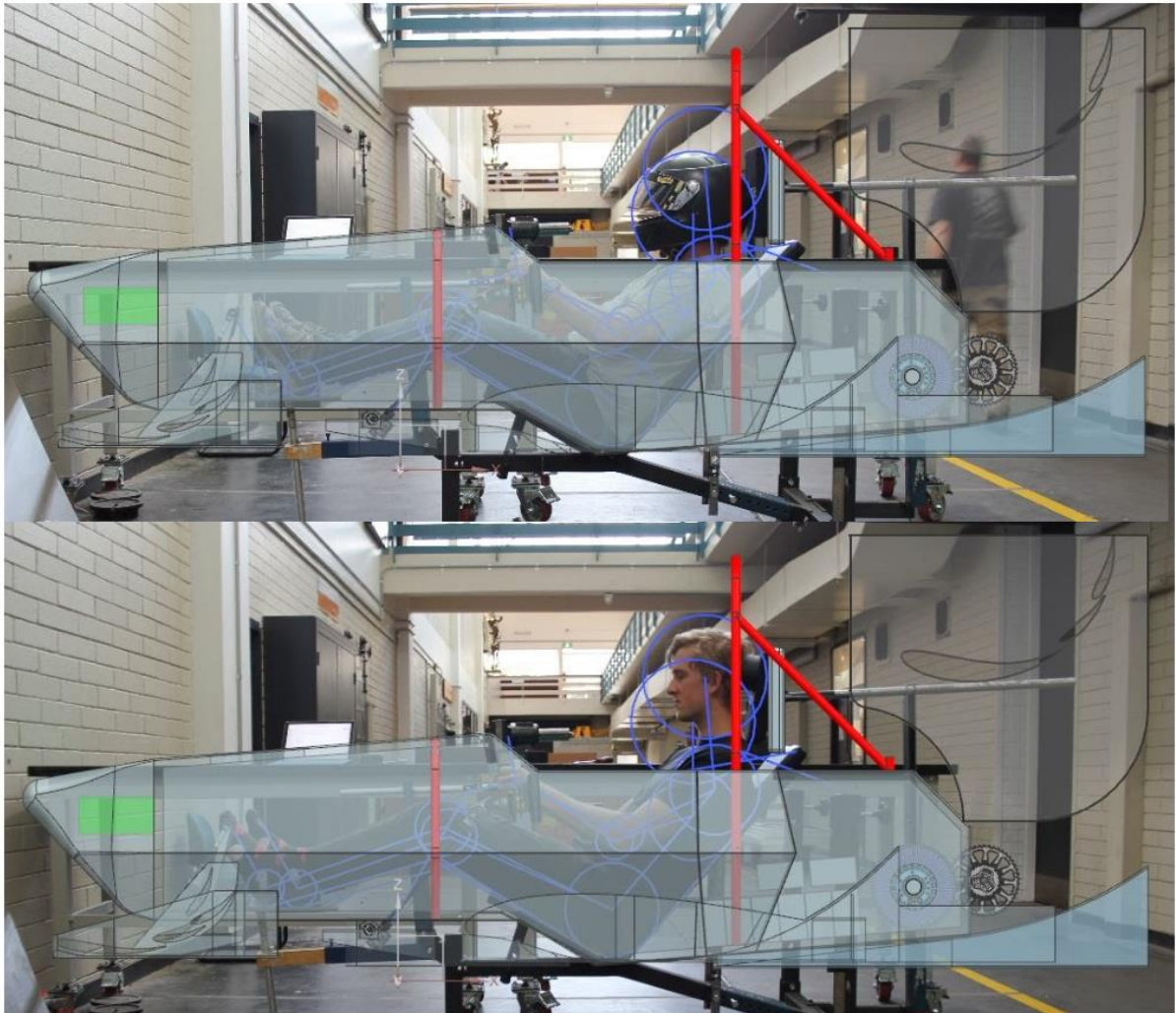


Figure 5.11: Preliminary CAD design overlaid onto images taken from ergonomics rig bench testing.

## Manufacturing Considerations

There are several approaches to manufacturing the monocoque chassis, each with their own set of advantages and disadvantages that must be considered.

### Cut and Fold

The cut and fold method was first pioneered along with the first ever composite monocoque chassis in the McLaren MP4-1 Formula One racing car. All modern day aluminium monocoque chassis designs use this technique. This manufacturing method involves taking a full size stock panel, followed by the removal of a strip of material from the inside of the bend to be formed. The panel is then folded over to form the desired angle of bend and a reinforcing strip of material is added to stiffen the bend.

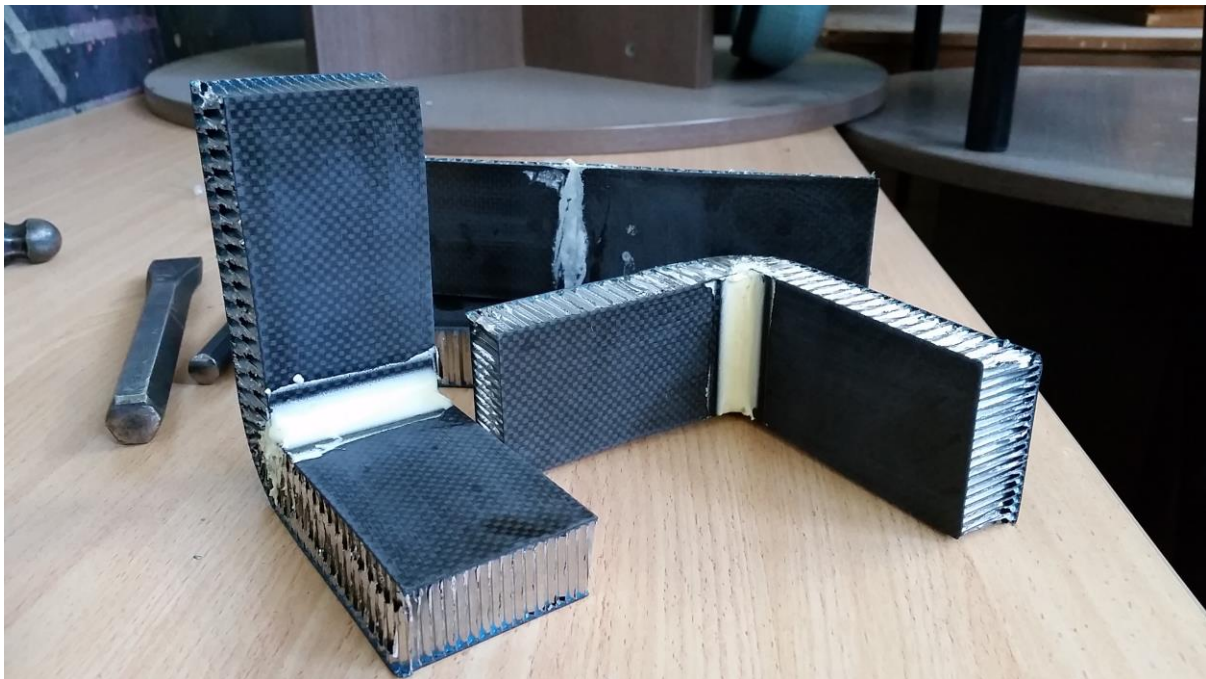


*Figure 5.12: Example test specimens from 2017 of a flat panel that has been 'cut' and 'folded'.*

The best method for cutting out the flat pattern of the chassis from the sandwich panel is CNC routing. Once the panel is routed, a series of jigs is used to assist in bending the panel into its correct position. Epoxy filler is applied to the insides of the folds to provide initial stiffening of the bends and to form a corner radius which the reinforcement carbon can conform to.

The completed chassis for ECU-R's 2014 car is shown in Figure 5.13. The benefit of the cut and fold method is that it is a low cost and fast way of manufacturing a monocoque. Theoretically a single sandwich panel cure could be enough to manufacture an entire monocoque. However practically that is not really the case due to honeycomb sheet sizes available and different laminate stack-up requirements through the monocoque. In addition to this, manufacturing accuracy is a concern, along with manufacturing repeatability and hardpoint installation accuracy. The structural integrity of the cut and fold bend itself also requires validation.



Figure 5.13: Edith Cowan University Racing 2014 cut and fold monocoque chassis. [27]

## Moulded

This is the preferred manufacturing method for a monocoque chassis and is the most popular method for Formula Student and is used everywhere in the upper tiers of motorsport such as Formula 1, IndyCar, Formula E and LMP1.

The first step in the process is the manufacture of a plug. This is typically CNC machined out of a tooling material such as epoxy tooling board or polyurethane tooling board. MDF is also an option. The pricing varies depending on the type of material and its temperature resistance rating and can be very costly for high temperature solutions. The plug is usually sanded and finished with a coat of paint.



Figure 5.14: Monocoque plug and composite tool from Revolve NTNU, 2016. [28]

Once the plug is completed, a mould is manufactured from it using composite materials. Either fibreglass or CFRP can be used, fibreglass obviously being the cheaper option, however a special tooling resin must be used. This tooling resin is able to be cured at near room temperature but must also be able to sustain the high autoclave temperatures and pressures for the final cure. The composite tool can be manufactured either with a resin infusion lay up or with prepreg tooling. The composite mould requires at least 4-5 mm of thickness to be sufficiently stiff and reduce springback or twist and warping under temperature and pressure. For high end automotive and aerospace applications, it is typical to use a matching material for the mould and the final part, as the two will share the same thermal expansion characteristics. An additional benefit of a moulded manufacturing method is that the hardpoint locations for important components such as wishbone mounting points can be machined into the plug. High precision fit dowel pins are inserted into the plugs, and the tooling mould is created with the pins going through them. When the tooling is cured, it is demoulded with the dowel pins still inserted. Then for the outer skin laminate of the monocoque is being placed down, it can be done so around the dowel pins along with the inserts in their correct position.

The cure schedule for a moulded monocoque chassis is typically first achieved with an outer skin laminate cure, followed by the bonded inserts and core, and finally the inner skin laminate. Normally in flat panel sandwich panel construction the two skins are pre-cured first, then trimmed and bonded to the honeycomb core in a second cure. With laying up into a mould however, the outer skin must be cured first in the mould separate to the inner skin.



Figure 5.15: Placement of chassis inserts inside the mould, Revolve NTNU, 2014. [29]

The advantages of the moulded manufacturing method are manufacturing accuracy and lack of constraints on geometry. While the cut and fold method limits the monocoque to be comprised of flat panels with radiused edges and corners, a moulded monocoque can have any number of bends and curved faces, so long as the part can be demoulded. Some

monocoque moulds consist only of two parts while more advanced geometries require at least five parts for the entire tub. Due to the complexity of the process, manufacturing time is significantly increased over the cut and fold method in almost every aspect, from mould construction time to layup time. The only time saving step in the process would be the insertion/lamination of inserts into the chassis.

## Hybrid Concept

This manufacturing method was first made noticeable by RMIT Electric Racing in 2018 for their R18e chassis. It is a hybrid concept of the cut and fold manufacturing process and the moulded concept. The monocoque itself is still a moulded chassis, however instead of using a CNC machined mould as is common in industry, the mould is constructed from laser cut and folded aluminium sheet. While this does limit the geometry of the monocoque to have the same limitations as a cut and fold monocoque, it does allow for hardpoint locations to be located into the mould, different laminate stackups to be implemented and has a higher structural integrity. The most time consuming stage in the moulded monocoque manufacturing method is the mould construction, and with this concept it drastically reduces it from months to a matter of days.



Figure 5.16: RMIT Electric Racing R19e chassis mould, 2019. [30]

## Selection of Manufacturing Method

To select the desired manufacturing method for the 2019 monocoques, weightings for each method were assigned to various key candidate criteria. The best ranked method based off these weightings would be selected.

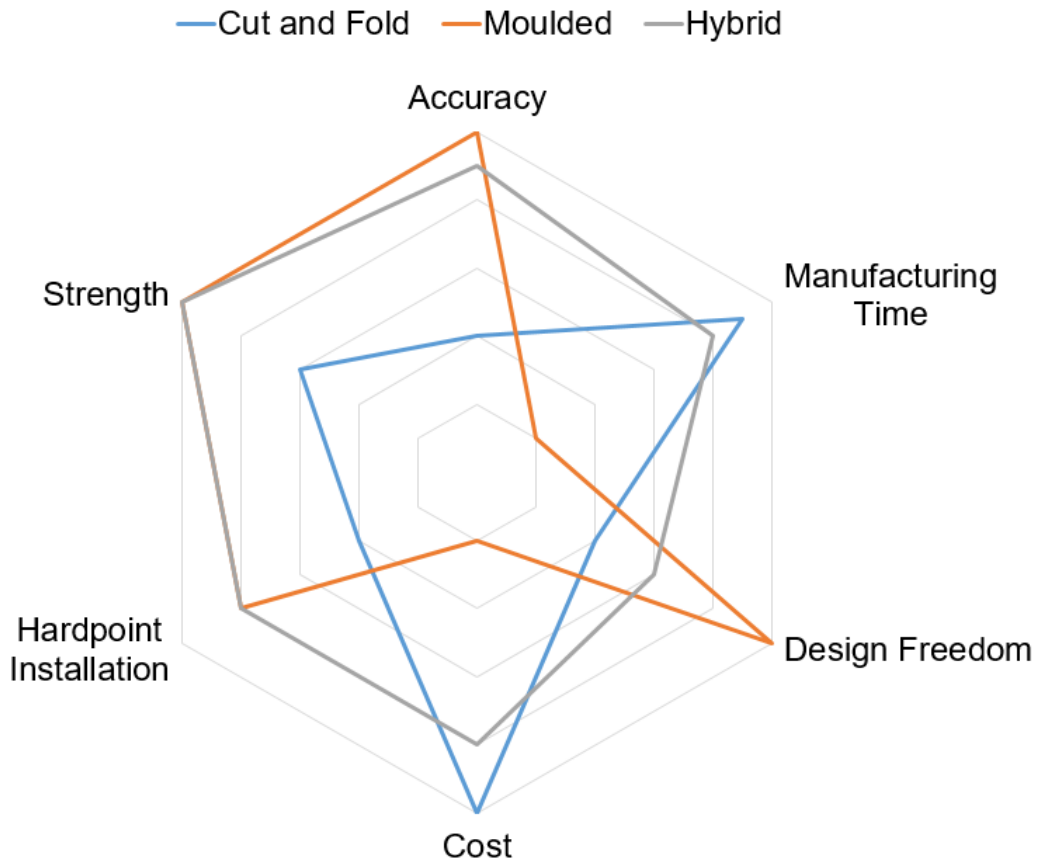


Figure 5.17: Radar chart for selection of manufacturing method.

The assigned relative weightings are shown in Figure 5.17 above. As alluded to earlier, it can be seen that the cut and fold method is both cheaper and less time intensive to manufacture, the moulded method is the most accurate and structurally sound, while the hybrid method combines the advantages of both. Because of this, the hybrid manufacturing method was the chosen concept for the 2019 monocoques.

The last key piece of information with regards to manufacturing the monocoque is sourcing a suitable autoclave facility to cure the monocoque. Monash University has an autoclave for research use however its size places heavy limitations on the geometry of the monocoque and restricts its length to being a half length monocoque. This would require to monocoque halves to be cured separately and then bonded afterwards, similar to what RMIT Electric Racing has for their monocoque. Further testing would be required to validate joint strength which places an unnecessary burden on the team. External large scale autoclaves were next considered. Daniel Young Composites based in Carrum Downs is a small scale operation catering to Supercars race car composites production. Preliminary talks were promising and a usage fee of \$100/hr was quoted. The other option was the Tickford Racing autoclave in Campbellfield. They offered to cure the monocoques for free, and so this was the selected manufacturing facility. The only design constraint imposed by their autoclave size was the overall length of the monocoque being restricted to 2650mm, 350mm more than the Daniel Young Composites autoclave.





Figure 5.18: Two halves, front and rear, of the RMIT Electric Racing R19e monocoque. [30]

## Material Selection

### Prepreg CFRP

Donated high temp prepreg carbon fibre had been used for physical testing and concepts in previous years at Monash. However, due to its high 177oC curing temperature, it is not the ideal material for manufacturing with an aluminium mould that has a significantly higher coefficient of thermal expansion of around 6 times in magnitude [31]. The effects of differing CTEs are much less significant at lower temperatures, and so a low temperature curing prepreg was sought after.

Two prepreg options were considered. The first was the SE84LV prepreg with RC200T twill weave fabric from Gurit (warehouse in Sydney), with a variable cure temperature ranging from 80°C to 120°C. The team has previously used Gurit as the main supplier of dry woven fabrics and wet laminating/infusion resins, so there was a good working relationship with the company. The other product considered was the EP-270 prepreg with Toray T300 standard modulus twill weave fabric, manufactured in-house by GMS Composites in Dandenong South, Victoria. This product also has a variable cure temperature range of 70°C to 130°C. The mechanical properties of the two options were very similar to each other and also comparable, if not higher performing, compared to the Cycom 970. Ultimately the local stock and customer support from GMS Composites was the distinguishing factor between the two and so that was the selected prepreg for the 2019 monocoques.

### Honeycomb Core

Research completed by Mclver and Paine [26] in 2015 revealed that there were significant mass savings of up to 10kg between aramid Nomex and aluminium honeycomb core materials. At the time tests were only completed with Nomex cores with disappointing results. It was clear at that stage that aluminium honeycomb cores, as frequently used by nearly all Formula Student monocoque teams and in high end motorsport, would be required to achieve the performance goals of the team.

The selected aluminium honeycomb for 2019 was first assessed and chosen by Mclver, Olorenshaw and Kusangaya in 2016. A 3 point bending MATLAB simulator [32] was used to sweep through a range of aramid, fibreglass and aluminium honeycomb core options from many suppliers to determine the best performing core in terms of overall strength, cost and mass savings. The results of the simulator sweeps were compiled in an Excel spreadsheet and analysed. From their analysis, the Plascore PAMG-XR1 5056 grade aluminium honeycomb with a cell size of 1/8", a nominal density of 4.5 pcf (pounds per cubic foot) and a thickness of 1" was chosen.

Company	Product	Compressive Strength (MPa)	Compressive Modulus (GPa)	Ribbon Strength (N)	Ribbon Modulus (GPa)	Expansion Strength (N)	Expansion Modulus (GPa)	Density (kg/m³)	Cell Size (mm)	Specific Compress (kg/m³)	Minimum Ply for Pass SIS Vlt	4	5	6	7	Displacement correlation ratio 30°	Force correlation ratio 30°	Displacement correlation ratio 30° 30°	Force correlation ratio 30° 30°	Displacement correlation ratio 45°	Force correlation ratio 45°	Displacement correlation ratio 45° 30°	Force correlation ratio 45° 30°				
HexTech	Flex Core 5052	3.6	1275.5	1.8	296.5	1.0	117.2	85.7	5.0	0.055	S	F	F	F	10.65305694	3.1375	15298.80864	2015.81	9.83951	3.89581	15449.3	6179.63	7.52325	5.18009	15699.4	7064.27	6.33
HexTech	Flex Core 5052	3.6	1344.5	2.1	310.3	1.3	137.9	88.9	5.0	0.052	S	F	F	F	11.28222451	3.72313	16580.24975	2473.81	10.0851	5.04043	16703.5	6888.61	9.13512	6.1108	19885.9	8948.64	7.6
HexTech	Flex Core 5056	3.2	861.8	1.4	220.6	0.8	89.6	49.7	5.0	0.064	0N/A	F	F	F	9.05209474	2.98073	12339.04716	803.88	8.22546	3.38893	12339.3	4943.73	6.52747	2.83738	12559.5	5051.27	5.59
HexTech	Flex Core 5056	4.7	1275.5	2.1	310.3	1.4	137.2	85.7	5.0	0.071	S	F	F	F	11.62210623	3.89391	16880.24975	2473.81	10.421	5.16879	16703.5	6888.61	10.0299	6.03146	20922.9	9438.61	8.46
HexTech	Flex Core 5056	5.4	1344.5	2.6	324.1	1.7	137.9	88.9	5.0	0.078	S	F	F	F	11.28222451	3.72313	16580.24975	2473.81	10.0851	5.04043	16703.5	6888.61	11.3391	5.19259	21319	11305.5	9.66
Plascore	PAMG-XR1 5056	2.3	668.8	1.7	310.3	1.1	137.9	49.7	3.175		S	F	F	F	10.68894722	3.52889	15705.43591	1382.79	9.83981	3.89591	15964.1	6385.62	7.45233	5.03595	16222.7	7300.21	6.34
Plascore	PAMG-XR1 5056	4.1	1241.1	2.8	468.8	1.7	186.2	70.5	4.7625		S	F	F	F	10.78406741	3.50874	16580.24975	2473.81	9.59548	3.89642	16703.5	6888.61	10.9048	4.90717	25341.1	11480.51	9.12
Plascore	PAMG-XR1 5056	8.9	2094.0	4.4	703.3	2.6	262.0	97.7	3.175		S	F	F	F	10.37205779	4.42278	16580.24975	2473.81	9.38357	3.87934	16703.5	6888.61	10.3958	4.83313	25341.1	11480.51	11.2
Plascore	PAMG-XR1 5056	10.5	2999.2	6.2	986.0	3.6	351.6	129.7	3.175		S	F	F	F	10.37205779	4.42278	16580.24975	2473.81	9.38357	3.87934	16703.5	6888.61	10.3958	4.83313	25341.1	11480.51	11.2
Plascore	PAMG-XR1 5056	1.1	310.3	1.0	186.2	0.6	89.6	32.0	4.7625		0N/A	F	F	F	10.11477636	3.03773	16580.24975	2473.81	8.93283	3.17379	16703.5	6888.61	9.91489	4.86167	25341.1	11480.51	10.5
Plascore	PAMG-XR1 5056	2.3	668.8	1.8	310.3	1.1	137.9	49.7	4.7625		0N/A	F	F	F	6.398027544	2.11215	8612.658402	2842.81	5.82353	2.52941	8754.48	3501.79	4.62362	3.08865	8896.31	4001.34	3.95
Plascore	PAMG-XR1 5056	4.1	1241.1	2.8	468.8	1.7	186.2	70.5	4.7625		S	F	F	F	10.68894722	3.52889	15705.43591	1382.79	9.83981	3.89591	15964.1	6385.62	7.45233	5.03595	16222.7	7300.21	6.34
Plascore	PAMG-XR1 5056	6.3	1861.6	4.0	648.1	2.3	248.2	91.3	4.7625		S	F	F	F	10.78406741	3.50874	16580.24975	2473.81	9.59548	3.89642	16703.5	6888.61	10.9048	4.90717	25341.1	11480.51	9.12
Plascore	PAMG-XR1 5056	0.7	306.8	0.6	137.9	0.4	82.7	25.6	6.35		0N/A	F	F	F	10.43824092	4.84132	16580.24975	2473.81	9.23922	3.89591	16703.5	6888.61	10.3789	4.8705	25341.1	11480.51	11.2
Plascore	PAMG-XR1 5056	1.4	399.9	1.2	220.6	0.7	103.4	36.8	6.35		0N/A	F	F	F	4.8958139	1.54807	6079.523578	2086.31	4.20101	1.4889	6179.64	2473.81	3.95596	3.95926	6279.75	2825.86	2.88
Plascore	PAMG-XR1 5056	2.7	792.9	2.0	344.7	1.2	151.7	54.5	6.35		S	F	F	F	7.650531161	2.52498	10639.16628	3510.81	6.94098	2.77939	10814.4	4325.74	5.4989	2.6659	10989.9	4945.1	4.83
Plascore	PAMG-XR1 5056	4.0	1185.9	2.8	461.9	1.7	186.2	88.9	6.35		S	F	F	F	11.30754804	3.66589	16580.24975	2473.81	9.91209	3.96881	16703.5	6888.61	8.22731	5.19259	18153.9	8481.37	6.86
Plascore	PAMG-XR1 5056	4.0	1185.9	2.8	461.9	1.7	186.2	88.9	6.35		S	F	F	F	10.78406741	3.50874	16580.24975	2473.81	9.59548	3.89642	16703.5	6888.61	10.9092	4.90411	25119	11305.51	8.9
Plascore	PAMG-XR1 5056	3.4	1383.8	3.4	579.2	2.1	220.6	83.3	6.35		S	F	F	F	10.56167385	4.48233	16580.24975	2473.81	9.37339	3.84921	16703.5	6888.61	10.5761	4.72923	25341.1	11480.51	10.7

Figure 5.19: Core selection spreadsheet developed by Mclver, Olorenshaw and Kusangaya in 2016.

## Filming Adhesives

An adhesive film is required for bonding the carbon skin laminates to the honeycomb core. Monash has had experience using the Cytec MTA 240 (as recommended by Boeing with a flexible cure between 80°C and 177°C) and Gurit SA 80 adhesive films. The MTA 240, while three times the price, is substantially better to handle when manufacturing due to its scrim film carrier. It also exhibits better flow through the cell walls of the honeycomb when cured. Another option was the GMS Composites EP-272 product which is around the same price as the Gurit SA 80 adhesive film, although when initially tested the panels suffered from a delamination failure mode, with little damage to the CFRP skins or core. This suggests that the new adhesive film, whilst cheaper, would not be suitable for use in the monocoque. Therefore, MTA 240 was selected as the adhesive film of choice.

Another type of adhesive is required for splicing together separate segments of honeycomb core within the monocoque. A Hexcel HexBond 212-NA foaming adhesive was recommended and purchased from GMS Composites for this purpose. The adhesive is able to be inserted during the layup and expands at temperature to form a complete bond between pieces of core. It can also be used for bonding hardpoint inserts to the core.

## Development of the Design

The initial development of the monocoque geometry began in early 2018, and steadily progressed into the beginning of 2019. The development process required frequent iterations and changes to find the best compromise between aerodynamic goals and the packaging of the driver, powertrain and suspension.

### Initial Concept

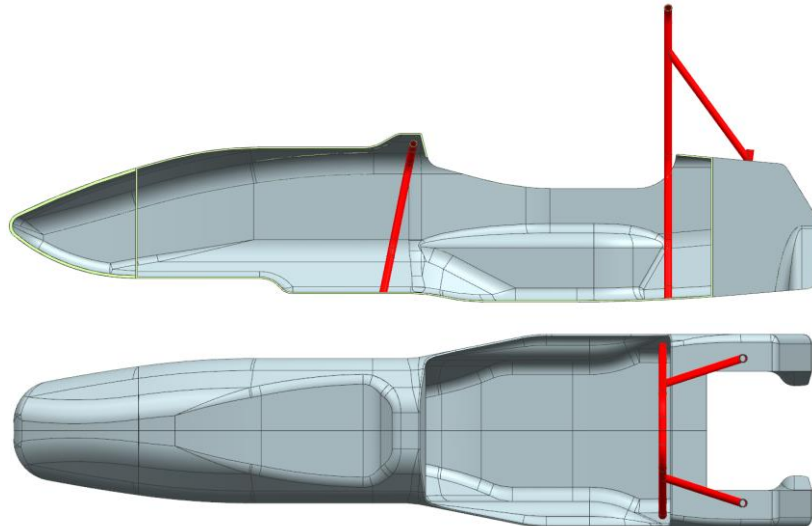


*Figure 5.20: Initial concept from 21/04/2018.*

The initial concept featured a low nose, side undercut of the cockpit section and an open rear section for powertrain packaging, drawing inspiration from TU Graz and TU Munich combustion vehicles. The driver ergonomics package remained the same as from 2015 to 2018. The rear features a rake angle similar to the 2015 spaceframe chassis. The suspension package is able to be mounted at similar angles to previous vehicles as well.

### Fifth Iteration

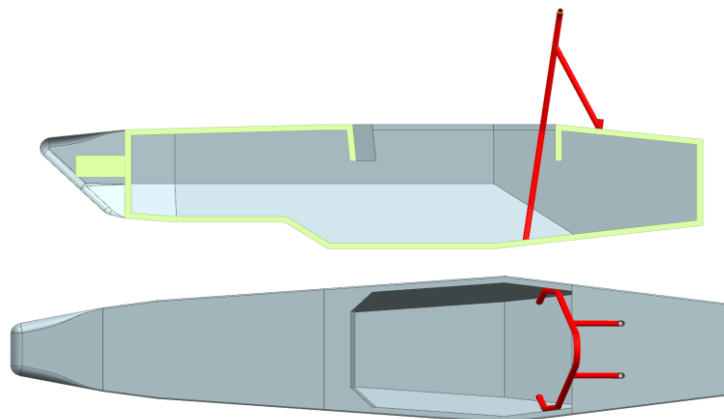


*Figure 5.21: Fifth iteration from 01/10/2018.*

The fifth iteration incorporates the selected hybrid manufacturing method pioneered by RMIT Electric Racing. The mould is a laser cut and bent aluminium sheet mould, limiting the monocoque geometry to flat panels. The design draws inspiration from Global Formula

Racing's monocoque designs since 2015, with a flat top section and high cockpit sides. The chassis now has a high nose along with an even more raised pedal position, as well as increased rear rake angle all aimed at increasing the aerodynamic potential of the vehicle.

## Eight Iteration

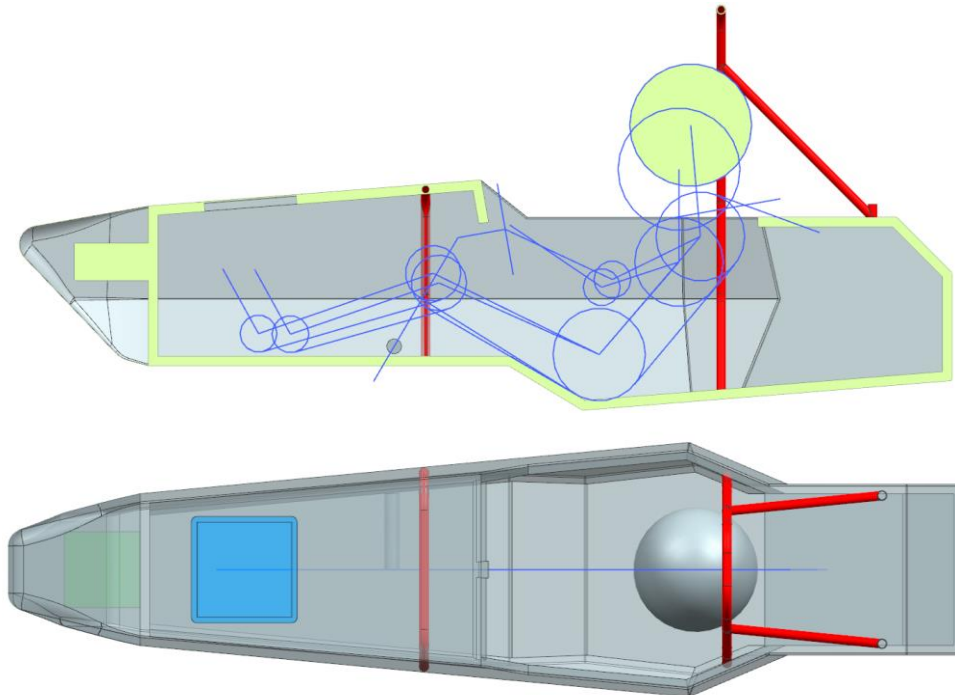


Figure 5.22: Eight iteration from 01/01/2019.

The geometry developed in this concept brings the design much closer to the final design as initial powertrain and suspension concepts had begun and were able to be integrated in. This concept significantly narrowed the rear section of the monocoque for aerodynamic reasons and moved the roll hoop bracing pickup point on the monocoque further rearwards to fully protect the KTM 690 within rollover envelope. It also has the driveline mounted to the outside of the chassis, reducing its overall length. The rear rake section has been further simplified by making the entire floor flat. In order to package the accumulator and motor within the monocoque without increasing the wheelbase of the vehicle, the driver seat back angle has been made more upright. This has changed from  $37^\circ$  to  $50^\circ$ . This upright seating position has been validated on an ergonomics rig and poses no issues to the driver.

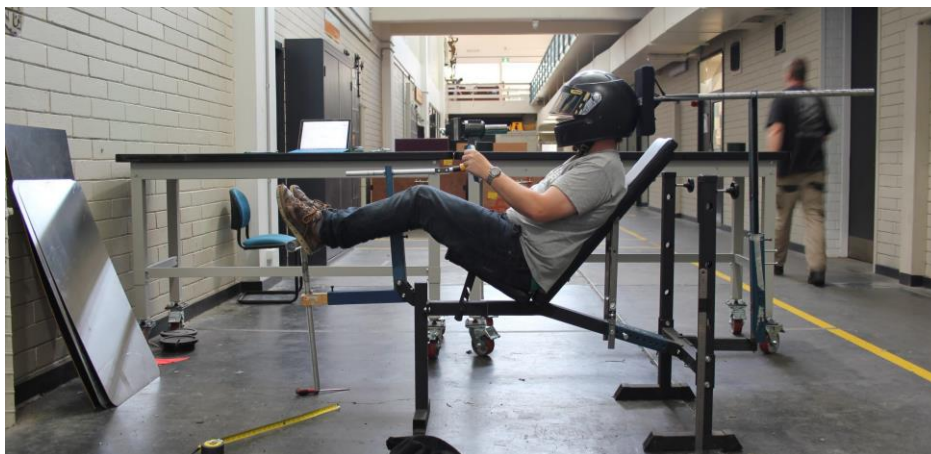


Figure 5.23: Validation of driver seating position on the ergonomics rig.

## Eleventh Iteration

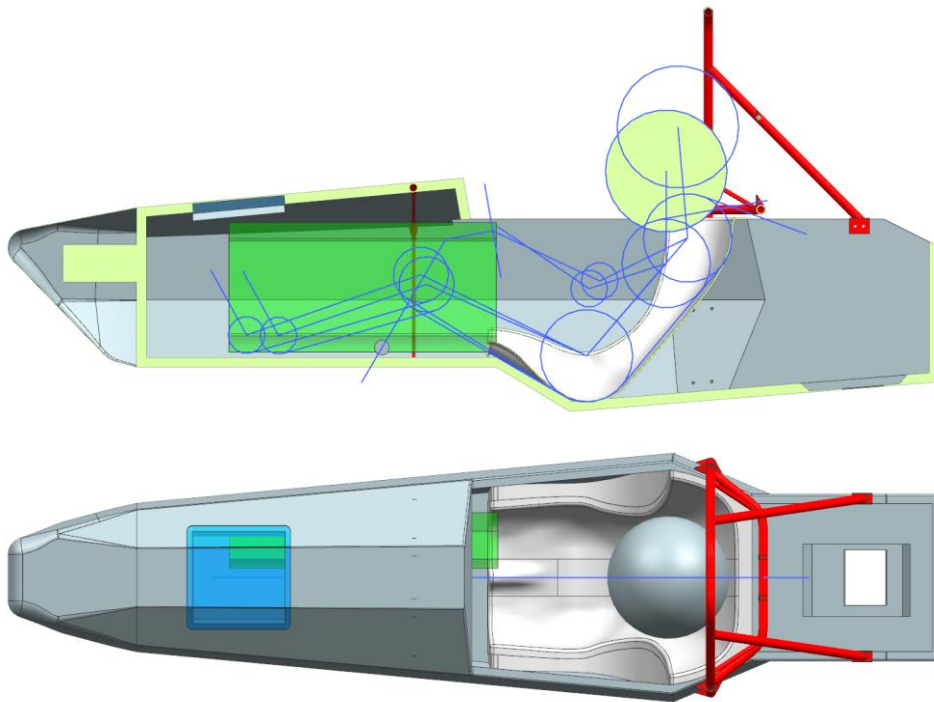
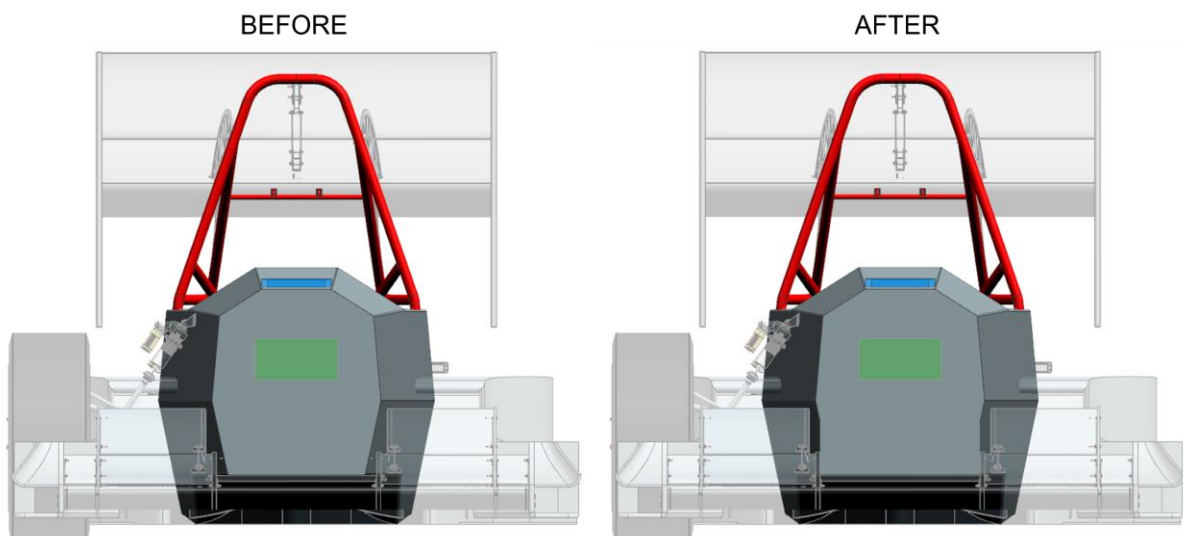


Figure 5.24: Eleventh iteration from 13/01/2019.

The last iteration before the final design saw the main roll hoop has been moved to the outside of the monocoque to both widen it and provide clearance with the driver. The main hoop bracing tubes have also been moved onto the vertical panel section, taking inspiration from TU Delft's monocoque the 2008-2012 era. The shoulder harness panel has been replaced with a bent steel tube to provide more clearance with the engine. At the front, the roll hoop has been made taller to provide more freedom for steering wheel sizing. To minimise the loss of forward driver visibility with the high nose, the top section has been chamfered downwards.

## Final Design



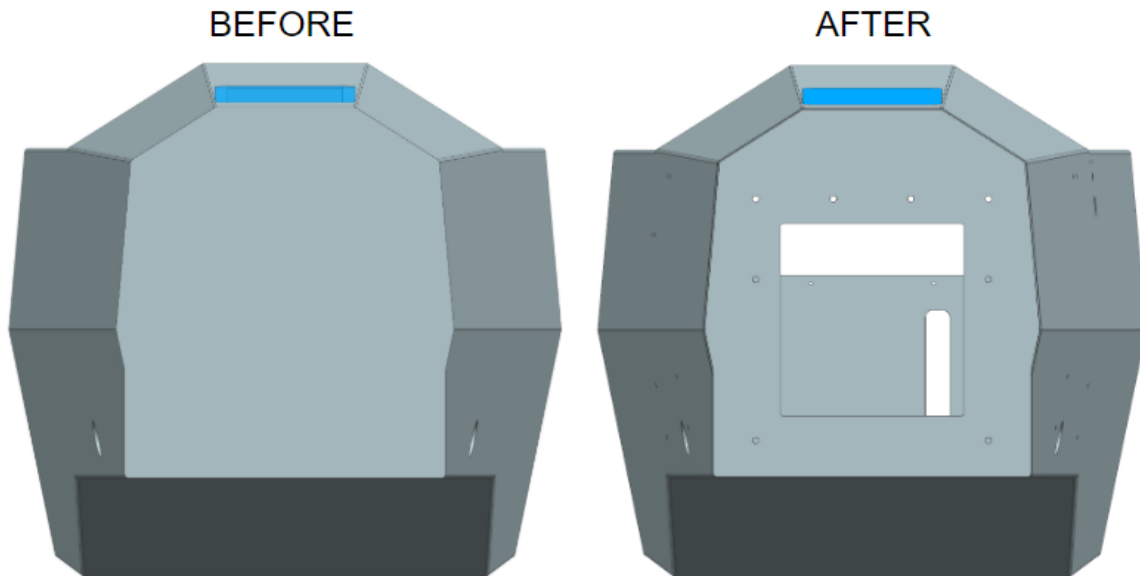


Figure 5.25: Refinement of front wing mounting (top) and front bulkhead (bottom) of the monocoque.

The final design saw some minor refinements to the overall geometry to better integrate with the rest of the car. The front of the car was reworked slightly to allow the front wing and its inner endplates to mount more easily to the sides of the car, while a cutout was introduced in the front bulkhead to increase accessibility to the pedal box. The cutout on the roof of the monocoque above the pedal box was narrowed to increase the effective panel width of the front hoop bracing panel. Lastly, to increase the ease of laminating the front hoop into the monocoque the bent tubular hoop was changed to a welded aluminium SHS section.

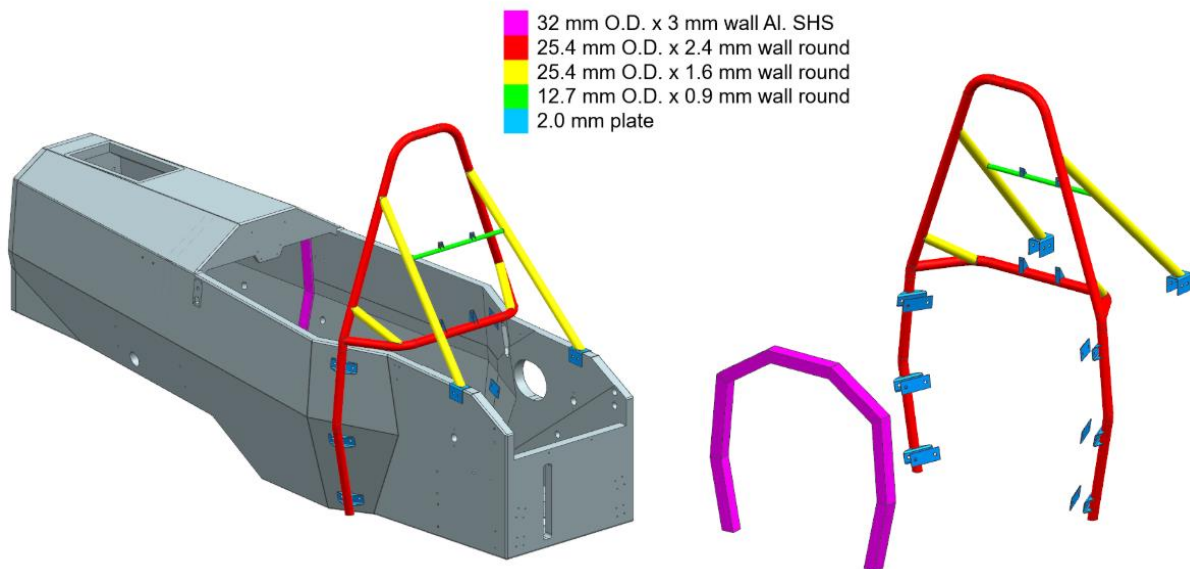
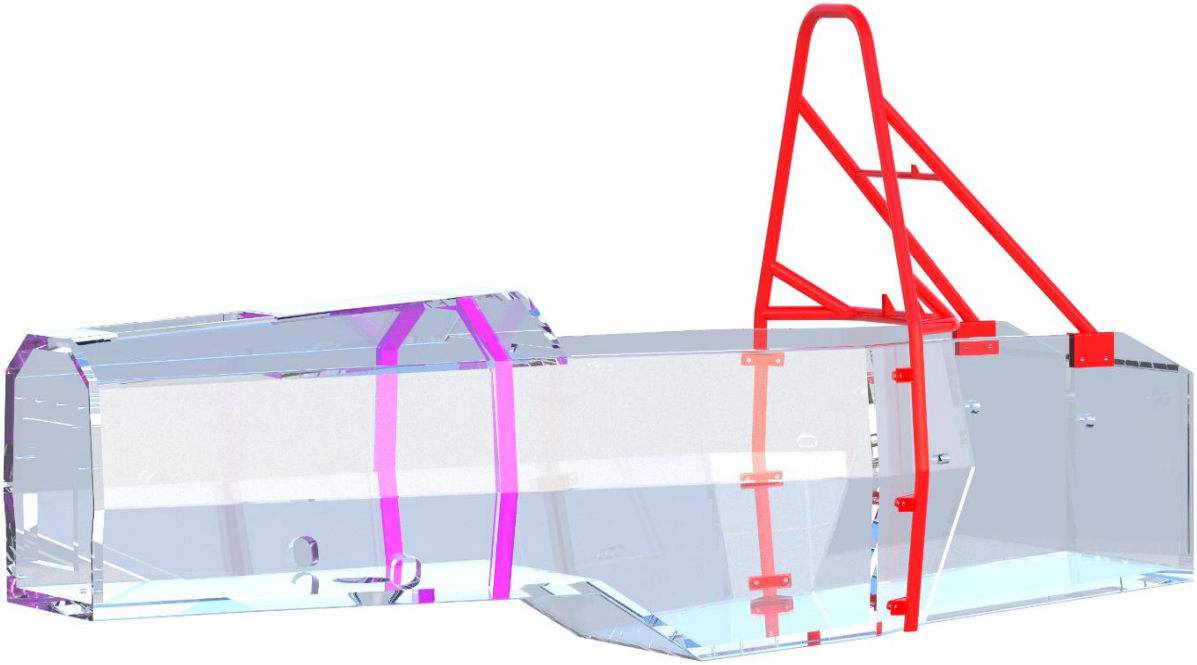


Figure 5.26: Final design overview.

With the geometry of the monocoque finalised, the remaining steps before manufacture were structural analysis and physical testing to validate the final design.



*Figure 5.27: Render of the final design.*

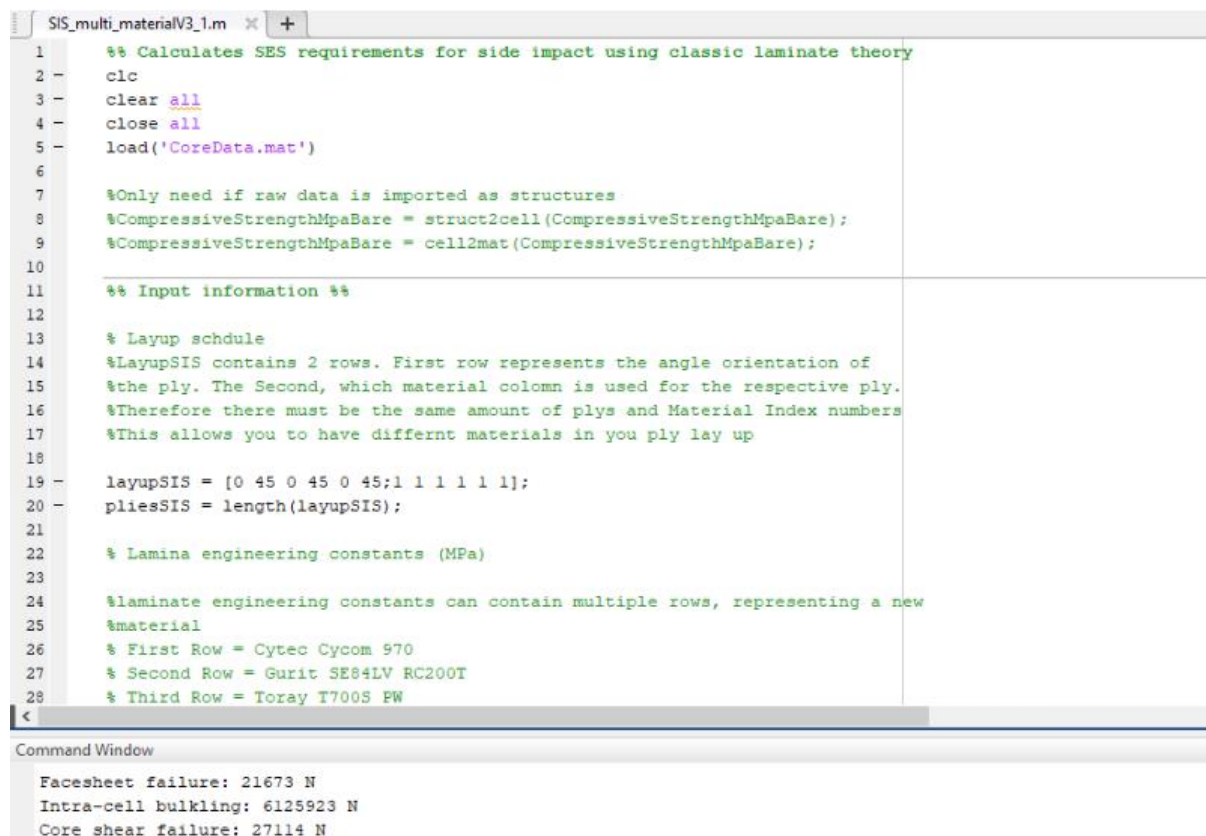
# Chapter 6 Analysis

## MATLAB

To assist with preliminary design and sizing of components, various scripts were written by previous MMS chassis engineers in MATLAB to computationally solve equations based on the composite theory researched in Chapter 4. These have been slightly updated in 2019 to better suit our requirements as design tools.

### 3 Point Bend

The 3 point bend laminate script was created by De Morton as part of a previous final year project [32]. The tool was used to conduct preliminary investigations on suitable ply arrangements and materials to be used in the monocoque chassis. As mentioned on pg. , this tool was used to select the Plascore 5056 grade aluminium honeycomb used in the 2019 monocoques. The MATLAB code uses calculations based on the theory developed in Chapter 4, requiring inputs for material properties, ply stackup and panel dimensions, and outputting failure load and deflection for the specified panel.



```

1 %% Calculates SES requirements for side impact using classic laminate theory
2 - clc
3 - clear all
4 - close all
5 - load('CoreData.mat')
6
7 %Only need if raw data is imported as structures
8 %CompressiveStrengthMpaBare = struct2cell(CompressiveStrengthMpaBare);
9 %CompressiveStrengthMpaBare = cell2mat(CompressiveStrengthMpaBare);
10
11 %% Input information %%
12
13 % Layup schedule
14 %LayupSIS contains 2 rows. First row represents the angle orientation of
15 %the ply. The Second, which material column is used for the respective ply.
16 %Therefore there must be the same amount of plies and Material Index numbers
17 %This allows you to have differnt materials in you ply lay up
18
19 - layupSIS = [0 45 0 45 0 45;1 1 1 1 1 1];
20 - pliesSIS = length(layupSIS);
21
22 % Lamina engineering constants (MPa)
23
24 %laminat engineering constants can contain multiple rows, representing a new
25 %material
26 % First Row = Cytec Cycom 970
27 % Second Row = Gurit SE84LV RC200T
28 % Third Row = Toray T700S FW

```

Command Window

```

Facesheet failure: 21673 N
Intra-cell bulking: 6125923 N
Core shear failure: 27114 N

```

Figure 6.1: 3 point bend MATLAB script.

Some modifications were made to the calculations used in the script to improve accuracy. Fortunately, this tool could be validated with previous physical testing results with the Cycom 970 prepreg skin material. The increase in solver accuracy is reflected in a comparison of the original and updated scripts with previous physical test results in shown in Figure 6.2.



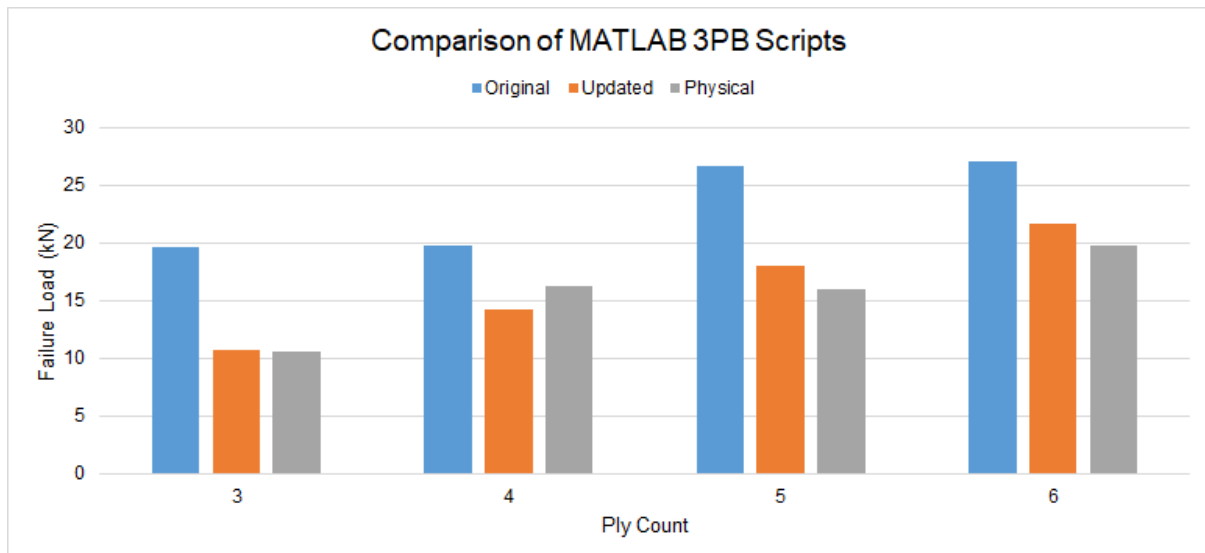


Figure 6.2: Comparison of MATLAB 3PB scripts for Cycom 970 sandwich panel strengths.

With the new material properties, the panel strength increased by approximately 50%, according to the MATLAB design tool. The data outputted by the script is analysed in SES along with the finalised monocoque geometry to provide preliminary estimates on the panel stackup requirements using the new GMS EP-270 prepreg CFRP.

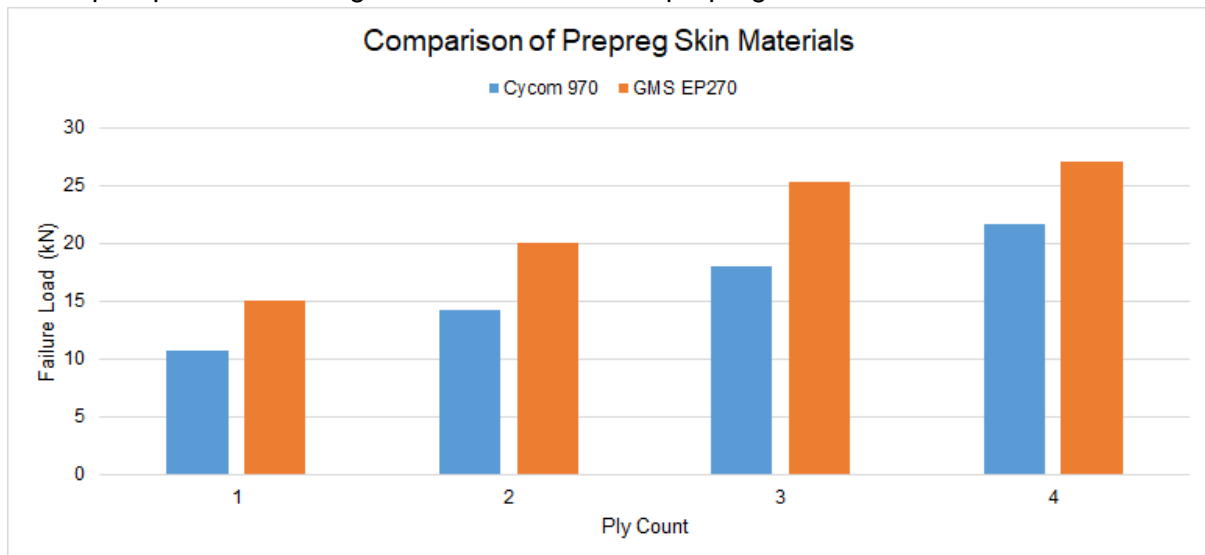


Figure 6.3: Comparison of Cycom 970 and GMS EP-270 sandwich panel strengths.

Previous physical testing data has shown a non-linear trend with increasing ply count and failure load, and the MATLAB design tool supports that to an extent. This is because as the ply count increases, the limiting failure mode transitions from facesheet failure to core shear failure. As a result, for regions of the monocoque where thicker laminates are required, such as the main roll hoop bracing, a more conservative laminate estimation is chosen.

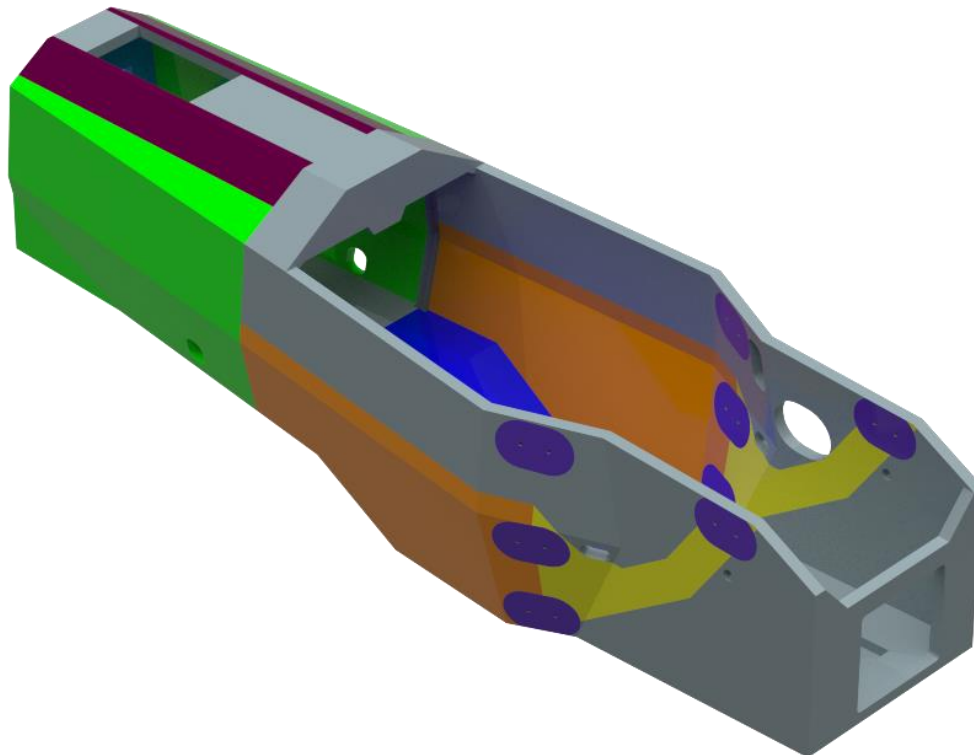
Another factor that needs to be taken into consideration is the perimeter shear requirement for three regions of the monocoque: front bulkhead, front bulkhead support structure and side impact structure. A simple hand calculation can be used to estimate the number of plies required:

$$n_{plies} = \frac{F}{D\pi\sigma_{shear}t_{ply}} \quad (6.1)$$

where:

- $F$  Perimeter shear load requirement
- $D$  Loading test fixture diameter (25mm or 32mm)
- $\sigma_{shear}$  CFRP skin shear strength
- $t_{ply}$  CFRP ply thickness

The preliminary chassis layup schedule is shown below in Figure 6.4. Note that the image is of the combustion car monocoque and is lacking annotations for EV specific primary structure elements such as the accumulator and rear impact protection panels. The next step before manufacture of the monocoque is to finalise the layup schedule with physical testing data to be discussed in Chapter 7, as this is the only accepted form of material data for SES.

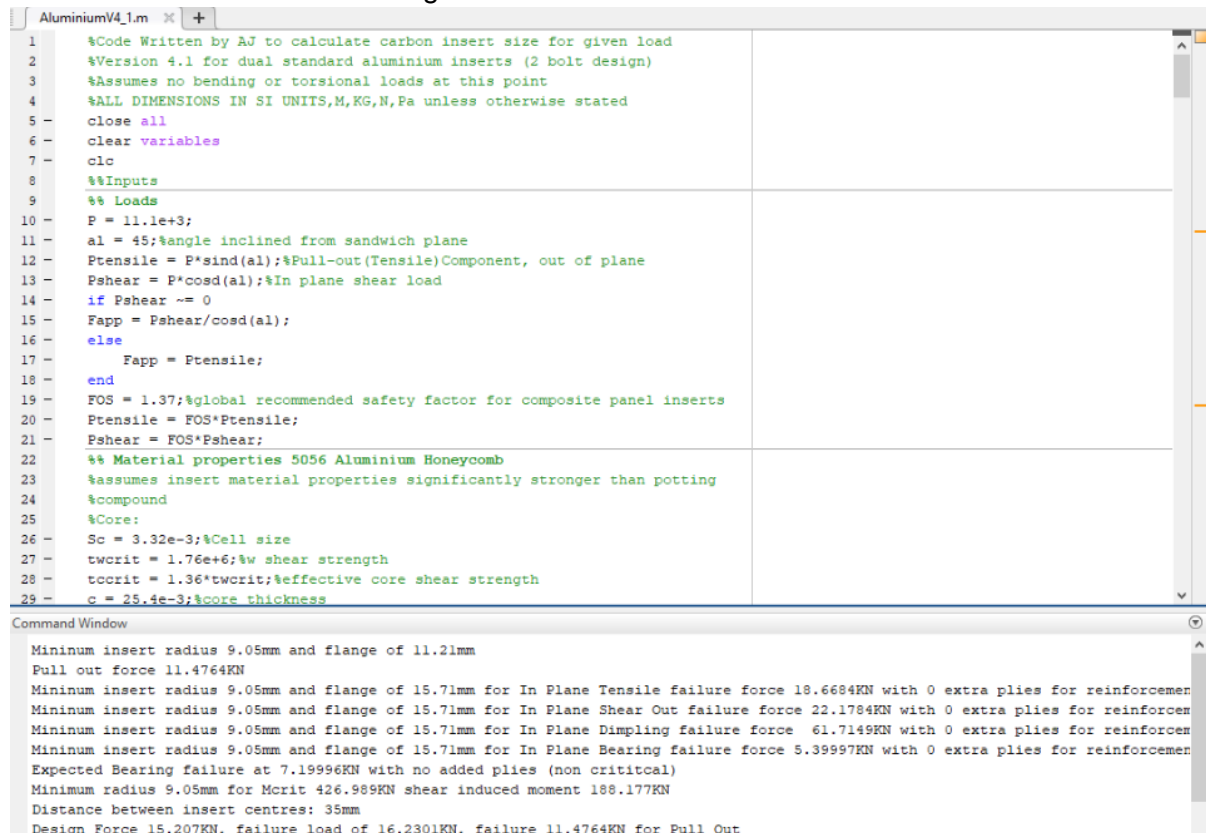


Panel Region	Ply Count (outer/inner)
Front Bulkhead	25 / 3
Front Bulkhead Support Structure	3 / 3
Front Roll Hoop Bracing	9 / 9
SIS Vertical	6 / 6
SIS Horizontal	6 / 3
Main Roll Hoop Bracing Support	6 / 6
Accumulator Side Protection	8 / 8
Tractive Side Protection	8 / 8
Rear Impact Protection	4 / 4
Other	3 / 3

Figure 6.4: Preliminary chassis layup schedule.

## Insert Design

The calculations and theory of the Insert Design Handbook were implemented into a MATLAB script by Kusangaya in 2016. This design tool would be used for preliminary sizing of the chassis hardpoint inserts, in particular the wishbone mounting inserts and harness attachments, as these are most critical to chassis performance. The script has been written to accept insert groups and factor in reductions in insert loading capacities, which is beneficial for bolted wishbone clevis arrangements.



```

1 %Code Written by AJ to calculate carbon insert size for given load
2 %Version 4.1 for dual standard aluminium inserts (2 bolt design)
3 %Assumes no bending or torsional loads at this point
4 %ALL DIMENSIONS IN SI UNITS,M,KG,N,Pa unless otherwise stated
5 - close all
6 - clear variables
7 - clc
8 %%Inputs
9 %% Loads
10 - P = 11.1e+3;
11 - a1 = 45;%angle inclined from sandwich plane
12 - Ptenstile = P*sind(a1);%Pull-out(Tensile)Component, out of plane
13 - Pshear = P*cosd(a1);%In plane shear load
14 - if Pshear ~= 0
15 -     Fapp = Pshear/cosd(a1);
16 - else
17 -     Fapp = Ptenstile;
18 - end
19 - FOS = 1.37;%global recommended safety factor for composite panel inserts
20 - Ptenstile = FOS*Ptenstile;
21 - Pshear = FOS*Pshear;
22 %% Material properties 5056 Aluminium Honeycomb
23 %assumes insert material properties significantly stronger than potting
24 %compound
25 %Core:
26 - Sc = 3.32e-3;%Cell size
27 - twcrit = 1.76e+6;%w shear strength
28 - tcocrit = 1.36*twcrit;%effective core shear strength
29 - c = 25.4e-3;%core thickness

```

Command Window

```

Minimum insert radius 9.05mm and flange of 11.21mm
Pull out force 11.4764KN
Minimum insert radius 9.05mm and flange of 15.71mm for In Plane Tensile failure force 18.6684KN with 0 extra plies for reinforcement
Minimum insert radius 9.05mm and flange of 15.71mm for In Plane Shear Out failure force 22.1784KN with 0 extra plies for reinforcement
Minimum insert radius 9.05mm and flange of 15.71mm for In Plane Dimpling failure force 61.7149KN with 0 extra plies for reinforcement
Minimum insert radius 9.05mm and flange of 15.71mm for In Plane Bearing failure force 5.39997KN with 0 extra plies for reinforcement
Expected Bearing failure at 7.19996KN with no added plies (non critical)
Minimum radius 9.05mm for Mcrit 426.989KN shear induced moment 188.177KN
Distance between insert centres: 35mm
Design Force 15.207KN, failure load of 16.2301KN, failure 11.4764KN for Pull Out

```

Figure 6.5: Hardpoint insert MATLAB script by Kusangaya.

The design goal of the wishbone inserts was for easy manufacture and a large factor of safety. The reasoning behind the latter is two-fold. Firstly, due to timeline constraints there was minimal time available for validating the chassis inserts via physical tests and so it was crucial to have successful tests on first attempt, even at the expense of some added mass. The second reason was due to consideration for damage repairs. For a worst case scenario of a crash or something that would damage the suspension, it would be far less taxing and easier to repair a damaged clevis, wishbone or outboard assembly than it would be to repair an insert in the monocoque. The idea is to design the chassis insert to be the strongest link in a series of components.

The critical design loads taken from *The Ring* spreadsheet for each wishbone member are summarised in Table 6.1. The angle at which the load is applied is also taken into consideration. As mentioned on pg. , some of the wishbone attachment points were deliberately placed such that loading on the inserts would be in-plane which generally has a higher load capacity as opposed to out-of-plane.

Table 6.1: Critical wishbone chassis insert loads.

Wishbone designator	Critical load (N)	Critical loading angle relative to monocoque panel plane (deg)
Front lower fore	7688	97
Front lower aft	-8058	97
Front upper fore	-3040	42
Front upper aft	3354	36
Front shock	-9765	60
Rear upper fore	-2356	53
Rear upper aft	2649	90
Rear lower fore	5805	47
Rear lower aft	-3806	10
Rear shock	-11750	51
Rear toe	2360	74

To reduce testing time and increase the ease of manufacture, standardised aluminium cylindrical inserts were chosen. Using the MATLAB design tool, two insert sizes were chosen to be tested. The first was the desired insert size while the second was to be used as a last resort backup should physical testing be unsuccessful, and assurance was required that the monocoque would be structurally sound. Packaging requirements dictated insert spacing distances of either 50mm or 65mm, both of which had more than adequate safety factor over the design loads. Insert stiffness was also given a high priority to minimise compliance in the suspension stiffness with a target of at least 3kN/mm set which also resulted in the high safety factors.

Table 6.2: Preliminary hardpoint sizing and failure loads.

	Type 1	Type 1	Type 2	Type 2
<b>Insert diameter (mm)</b>	10	10	20	20
<b>Insert group spacing (mm)</b>	50	65	50	65
<b>Out-of-plane pullout force (kN)</b>	13.63	15.35	13.66	14.90
<b>In-plane tensile failure force (kN)</b>	27.34	30.78	21.51	23.46
<b>In-plane shear out failure force (kN)</b>	31.25	35.19	25.29	27.58
<b>In-plane dimpling failure force (kN)</b>	90.72	102.16	126.25	137.68
<b>In-plane bearing failure force, non-critical (kN)</b>	6.20	6.99	10.31	11.24
<b>Stiffness (kN/mm)</b>	3.01	3.01	8.44	8.44

The next step is to validate these proposed insert sizes with physical testing.

## 3 Point Bend FEA

To complement the MATLAB simulations, a 3 point bend ACP model was created in ANSYS by Olorenshaw in 2016 [33]. The simulation performed here is purely linear, it may be worthwhile at a later stage to implement progressive damage modelling to further increase accuracy. The experimental results from this design tool were not used in the original determination of the chassis layup schedule, rather it was developed afterwards to become a useful tool for future chassis designs. Modifications to this model in 2019 included updated material properties and improved representative CAD geometry.

## Setup Procedure

### Workflow

The workflow in ANSYS is broken up into several modules. ANSYS has two composite processing modules, Pre and Post, used to define a composite laminate and to analyse a solved model, respectively. The loading fixture and panel supports are modelled in the Mechanical Model module. Both ACP (Pre) and the Mechanical Model feed information directly into Static Structural, where the bulk of the analysis simulation is completed.

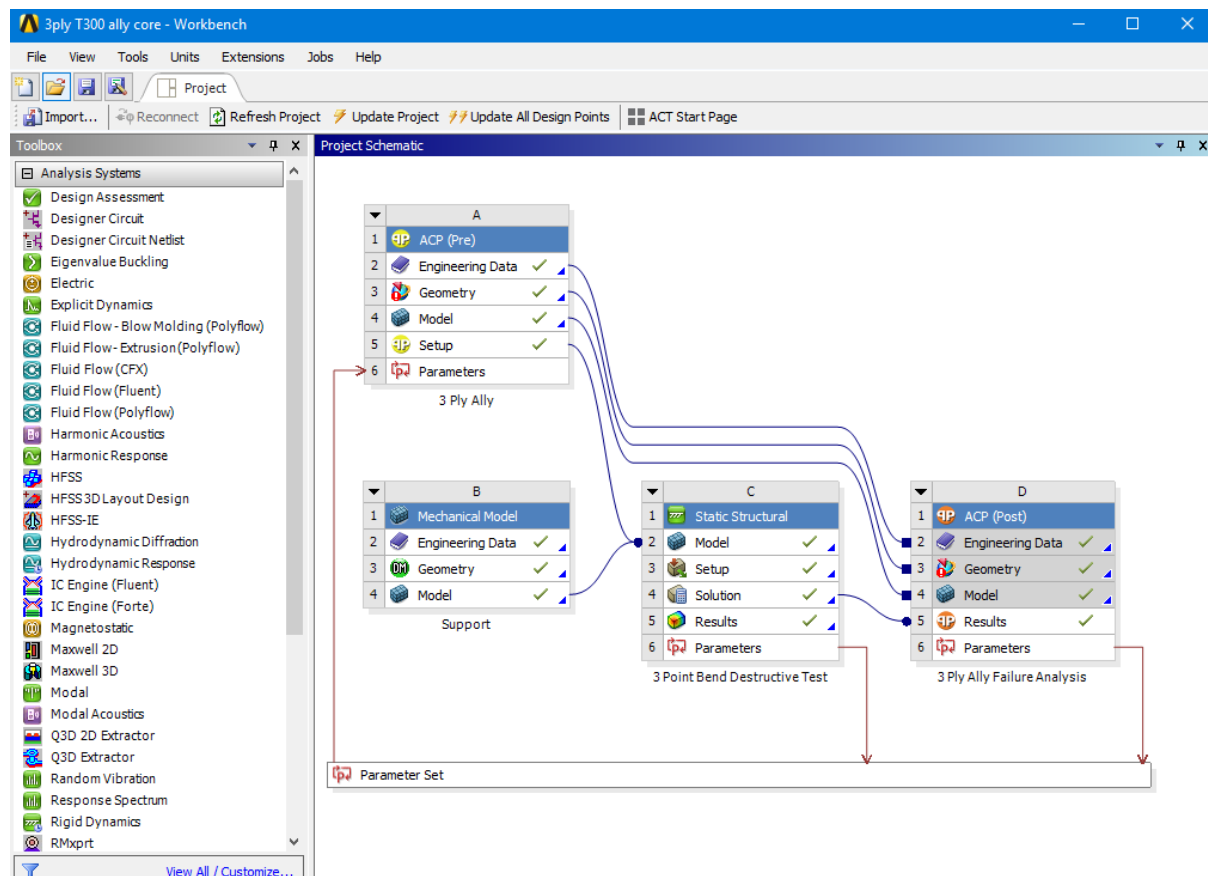


Figure 6.6: ANSYS Workbench for 3PB FEA.

## Material Properties

The material properties for the prepreg CFRP and aluminium honeycomb are directly imported into ANSYS as custom materials. Unfortunately, the material properties for the EP-270 provided by our sponsors, were not sufficient in detail and were lacking certain parameters such as ultimate strengths in tensile or compressive directions. Since the EP-270 uses a Toray T300 twill weave fabric, data was obtained for a Toray T300 prepreg with very similar mechanical properties from the Autodesk Heliux Composite design software database. The aluminium honeycomb had adequate material properties as provided by Plascore.

## Importing Geometry and Meshing

The quarter model composite panel is constructed in CAD as a 2D sheet body to be interpreted as a shell representation in ANSYS. Because the main area of interest of the model is at the interface between the sandwich panel and the load supports, a biased mesh sizing method has been implemented, with finer mesh being used in these areas, as seen in the image below. Quad mesh element types are used to improve solver efficiency.

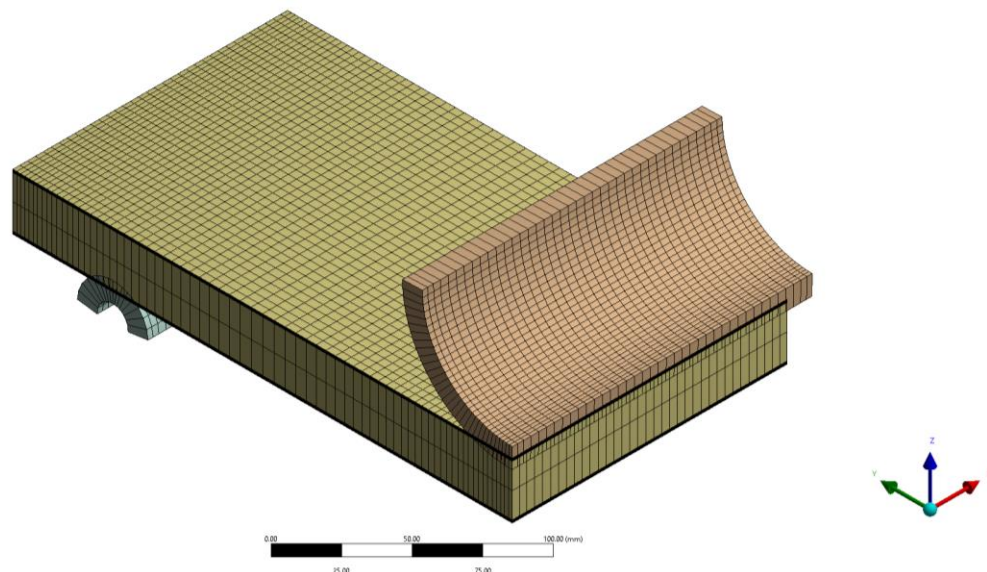


Figure 6.7: ANSYS mesh setup.

## ACP (Pre) Setup

ACP (Pre) allows for the definition of the composite structure. The workflow for defining a composite material is as follows [34]:

- Define fabric (ply material, ply stackup definitions etc.)
- Define rosettes and Oriented Element Sets (reference coordinate systems for ply fibre directions)
- Create Modelling Plies (assigning mesh elements to ply groups)
- Create Solid Model (extrudes shell model to a solid model)

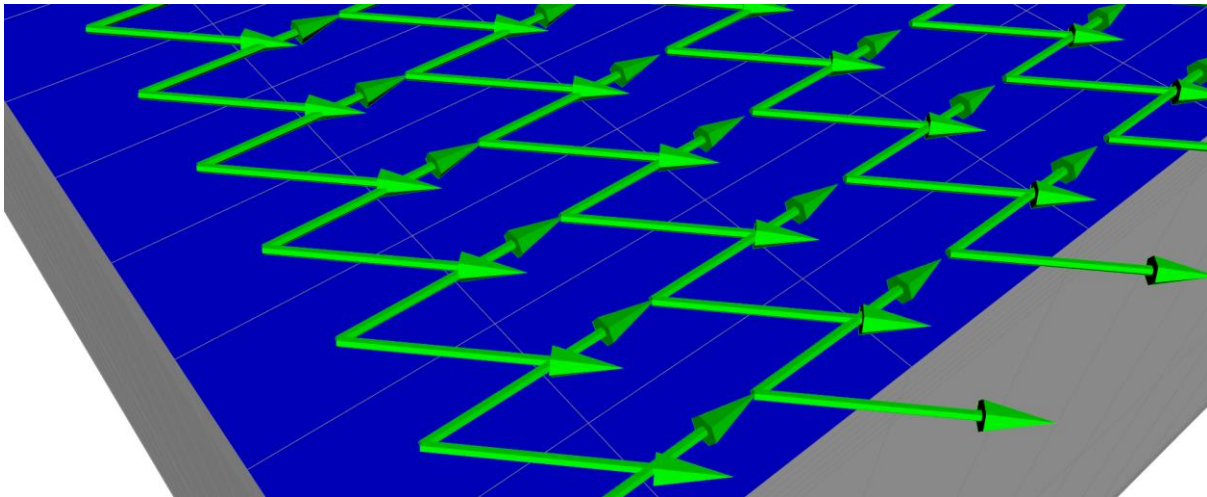


Figure 6.8: 6 ply sandwich panel modelled in ACP, showing 0/45 degree fibre directions.

## Contacts and Boundary Conditions

The structural analysis of the composite panel is done under the Static Structural model in ANSYS. The contact region between the panel support and load application fixtures to the composite panels are modelled as frictionless contacts to allow sliding of the panel against those surfaces. Since the FEA model is a quarter of the size of the physical model, frictionless support boundary conditions are used to model symmetry conditions. The panel support is treated as a fixed support reference point, while the actual load applied on the panel is achieved by applying a remote displacement on the load applicator. A reaction force probe is placed on the fixed panel support to determine the loading on the composite panel.

C: 3 Point Bend Destructive Test  
 Static Structural  
 Time: 1. s  
 15/10/2019 1:28 PM

- A Fixed Support
- B Remote Displacement
- C Frictionless Support
- D Frictionless Support 2

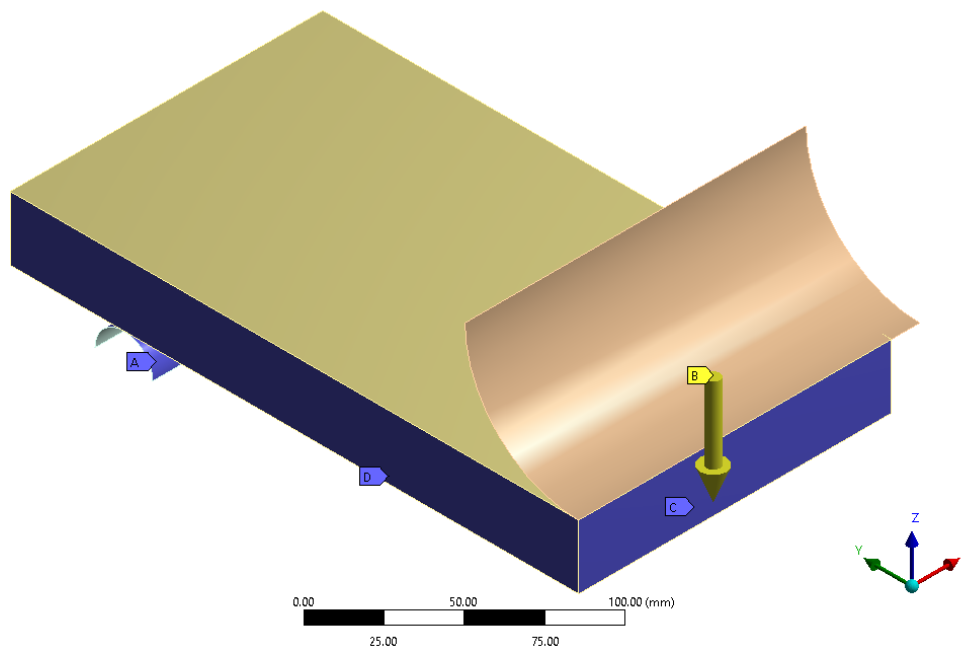


Figure 6.9: Model conditions in ANSYS Mechanical.

## Results Processing and ACP (Post)

Determination of the failure point of the composite panel is done through the post-processing package ACP (Post). In ACP (Post), failure criteria for both laminate and sandwich failure are set. ACP allows for multiple failure theories to be applied, such as max stress, Tsai-Hill and Tsai-Wu failure criteria. The failure criteria are then applied to the solid model for a visual representation. A panel is considered to be completely failed when the failure of any ply or core material has propagated across the full width of the panel. Finding when this occurs requires navigating to the correct time step of the simulation. The corresponding reaction force at the fixed support for this specified time step is then considered to be the ultimate failure load of the quarter sized composite panel.

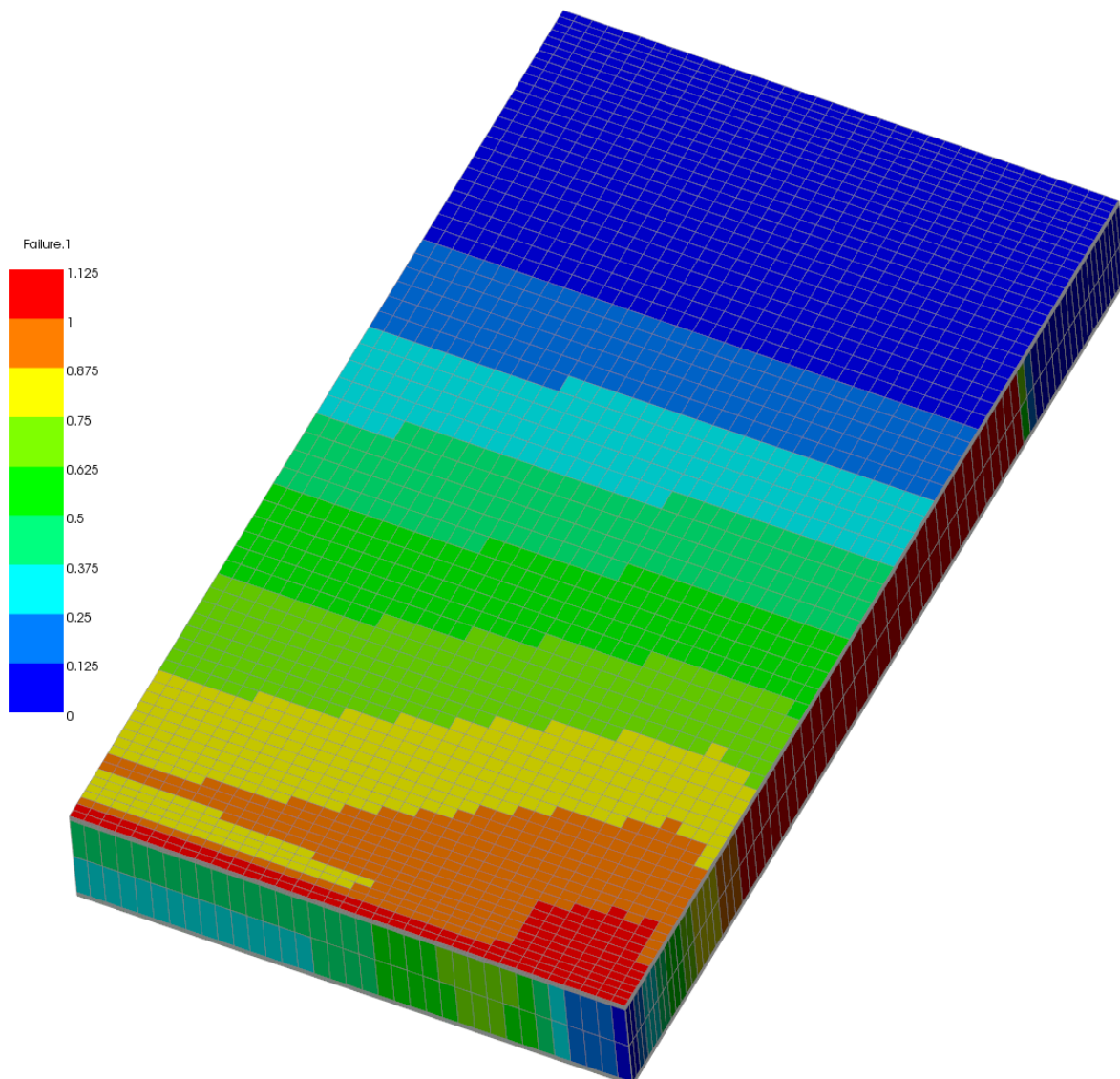


Figure 6.10: Ultimate load time step of the composite panel, showing full propagation of ply failure through the width of the panel.



## Discussion

A comparison of the panel failure loads between the MATLAB script and the ACP FEA is shown in Figure 6.11. It can be seen that the FEA produces more conservative failure loads than the MATLAB script. Had this design tool been ready to implement when the chassis layout schedule was being estimated, it would have been preferable to use the FEA results to produce preliminary estimates given that they are more conservative. Analysis by Olorenshaw [33] had already shown that this model had achieved 20% accuracy when compared to physical tests with the Cycom 970 prepreg, so the results can be fairly representative of real physical tests going forward.

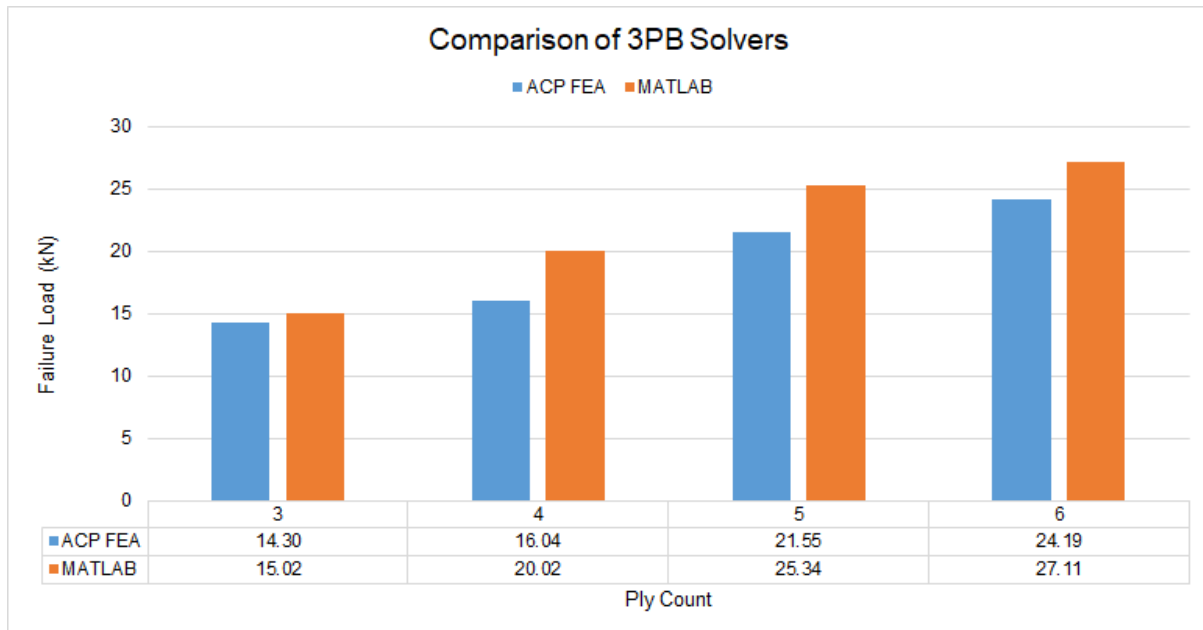


Figure 6.11: Comparison of failure loads simulated using FEA and MATLAB.

## Chassis Torsion FEA

It has already been explained on pg. the effect chassis stiffness and deformation can have on the overall performance of the car. Therefore, analysis must be conducted to ensure the chassis is meeting the target hub-to-hub installation stiffness (i.e. torsional stiffness) of 3300Nm/deg or more which was set from pg. . As seen above there are multiple tools that can be used to analyse a structure. In the case of analysing the torsional stiffness of the chassis FEA is by far the best option.

## CAD Model

The first step of creating an FEA model is to is to create a representative geometry. Due to the complexity of the monocoque CAD model, the decision was made to create a simplified CAD model for ease of implementation, to minimise meshing issues and to improve solve time.

A number of features have been simplified. This was done to balance the accuracy of the model and the computational load associated with solving it. The simplified model has omitted any holes for fastening the impact attenuator, wishbone clevises, main roll hoop and drainage holes. This simplification should not greatly affect the magnitude of the results. The next change that was implemented was to split the faces of the monocoque into ply regions, this is necessary so that the right ply stackup can be applied. The implemented changes in the monocoque CAD model can be seen in Figure 6.12.

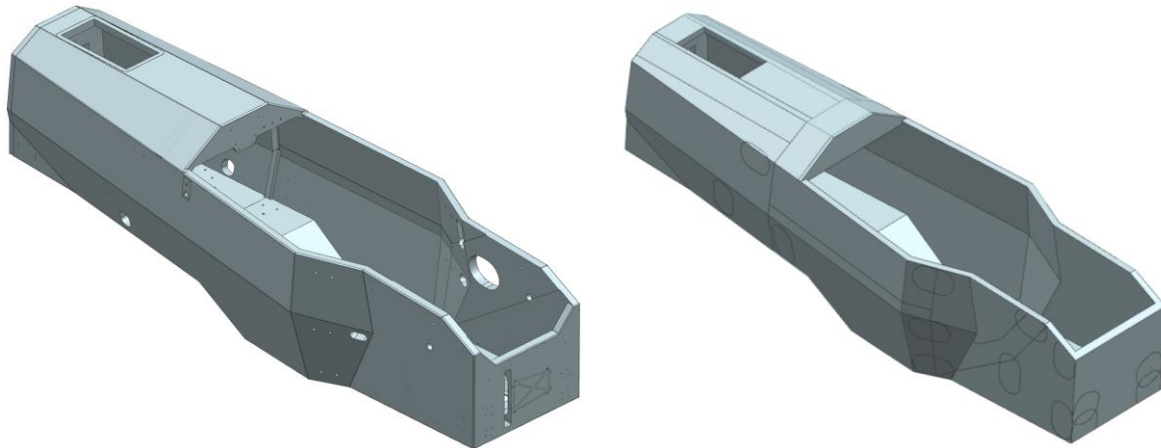


Figure 6.12: (Left) Existing CAD of the M19 monocoque. (Right) Simplified monocoque CAD.

All critical stiffness enhancing components must be both present in both the FEA simulation and the physical testing. This is because both are tools used to analyse the installation stiffness, which as mentioned in Chapter 3 is necessary to ensure that the car doesn't lose any vehicle performance as a result of an inadequately stiff chassis.

As such the engine must be included in the model. The engine is modelled as a rigid block, with the weight force acting onto the chassis through the engine mounts, as shown in Figure 6.13. This level of accuracy is sufficient enough as the stiffness of an engine is magnitudes above any other component in this assembly. By keeping the dummy engine simple, computational load is also decreased. It was decided for the electric vehicle that FEA didn't need to be conducted as of yet because the team didn't plan on doing physical testing on the electric vehicle before competition in December.

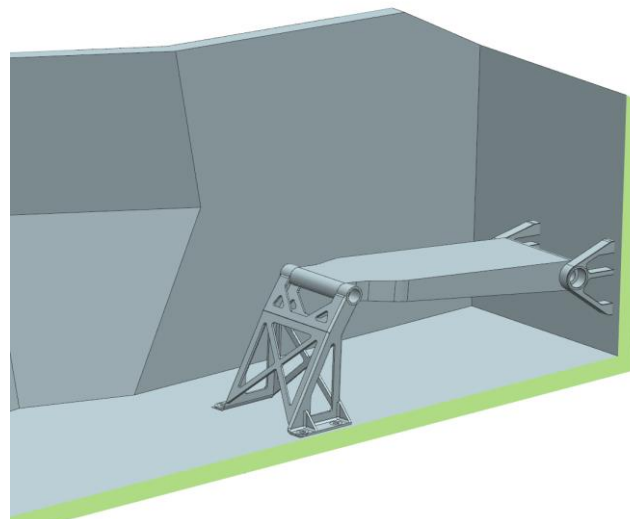
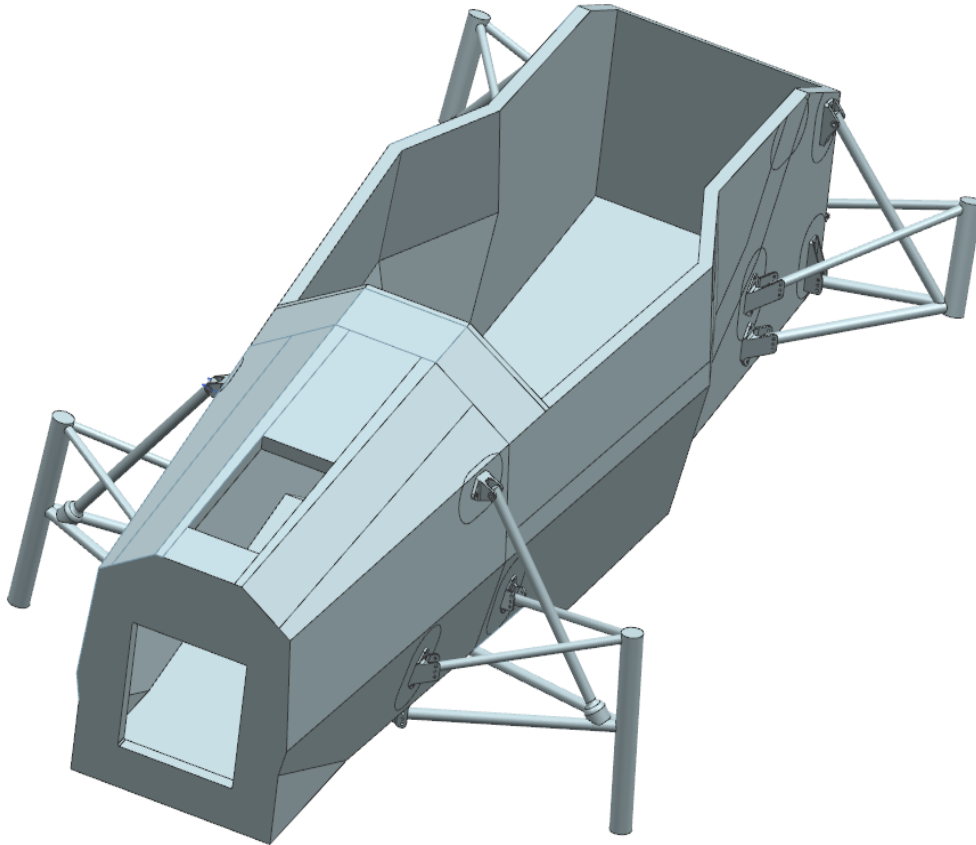


Figure 6.13: CAD representation of the powertrain.

The suspension CAD utilised is very similar to that in the physical testing. The wishbones and mounts have the same dimensions as in the real world situation with the exception of bolts and bearings. This decision was made as compliance incurred through these parts cannot be accurately accounted for. The uprights and shock have been modelled as rigid solid members to again reduce computational time and compliance respectively.



*Figure 6.14: CAD representation of the suspension.*

## Composite Model and FEA Setup

The following FEA analysis has taken place using the ANSYS composite package/platform, ACP. The laminate parameters used are defined in Chapter 7 and can be visualised in Figure 6.15 below.

Early research on literature from ANSYS revealed that in situations where the loading was out of plane, a solid model produces more accurate results [35]. Due to this, the solid model became the priority and was developed further. Initial results obtained from the solid model indicated torsional stiffness values that were significantly lower than those expected based on physical data. The source of these inaccuracies was found to be due to pinched off layers which greatly altered joints between multiple panels. Technical advice from LEAP Australia, coupled with analysis of the project schedule led the team to pursue a shell model over a solid model. This was due to the significant time constraints and the acknowledgement that reasonably accurate results can still be obtained from the shell model.

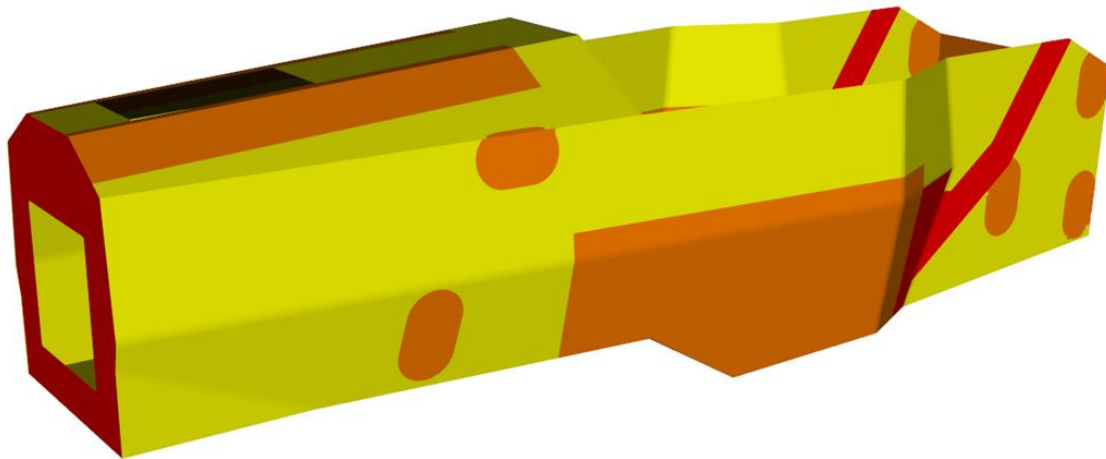


Figure 6.15: ACP Layup thickness plot.

The FEA constrains the vehicle in the same manner as the physical test, with the rear outboard under tension being fully fixed, the other as a roller support, and the front axle acting as a pivot point with a point load applied at each front outboard but in opposite directions. This can be observed in Figure 6.16.

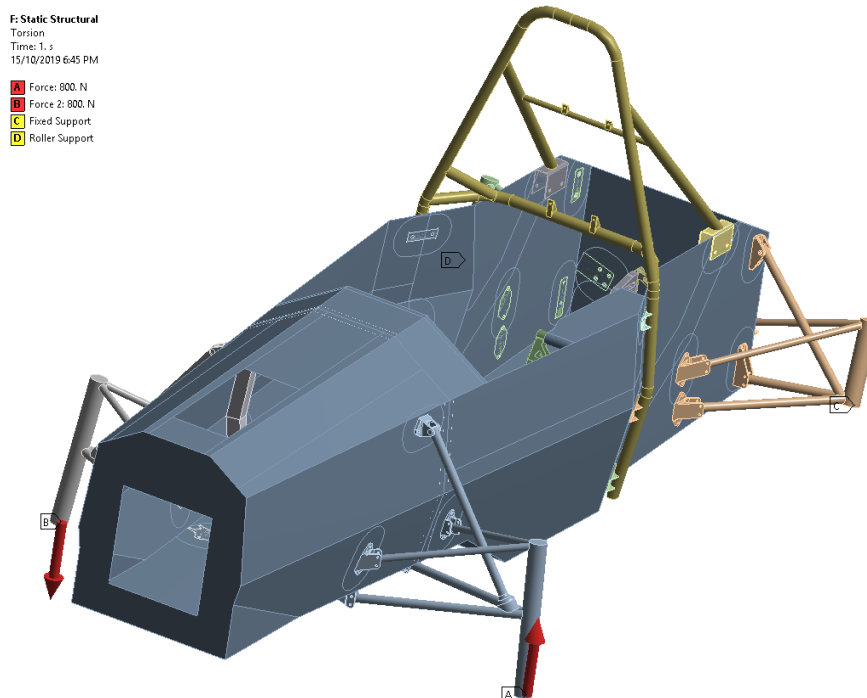


Figure 6.16: FEA Setup.

## Results and Discussion

The installation stiffness of the chassis has been measured in two ways. The first method is by using representative suspension and comparing the FEA results directly against the physical results. This method doesn't account for suspension compliance in the bearings, fasteners, rod ends etc. The second method involves measuring the simulated chassis stiffness using a rigid suspension and then combining this with physical suspension outboard compliance results to compare against the physical installation stiffness. Unfortunately, physical compliance testing was not completed for the 2019 suspension design and as such

the results from the team's 2017 compliance testing has been used instead. This second method is the preferred method, but using out of date data leaves too much room for potential error and as such the first method shall be used. The first method produces an installation stiffness of 3515Nm/deg.

From here physical bench testing shall be conducted once manufacturing has occurred to determine the accuracy of the FEA results. This comparison also potentially allows the team to see if there are any major manufacturing defects throughout the chassis. If the FEA results are within 5% then the shell model may be sufficient, otherwise it is advised that the solid model is persevered with. Regardless the team now has a working model that can be used to help future designs.

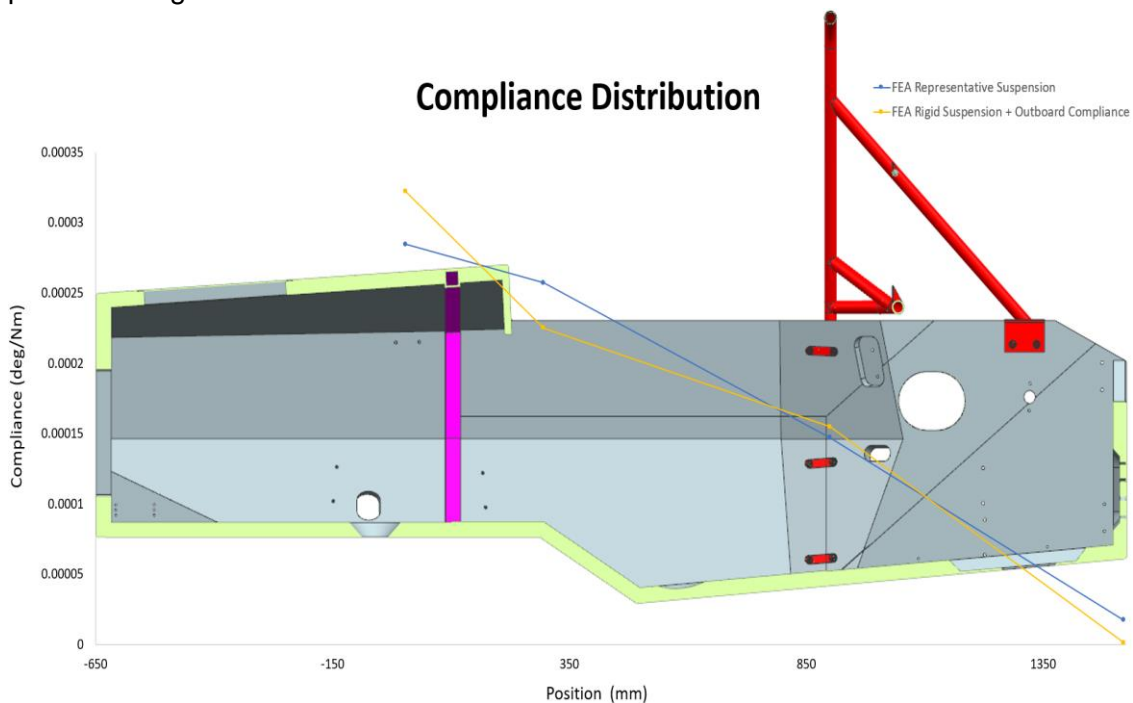


Figure 6.17: Compliance Distribution.

Rigid Suspension  
 Expression:  $\text{abs}(\text{atan}(\text{USUM}/\text{LOCZ}))$   
 Unit: °  
 Time: 1  
 14/10/2019 9:56 PM

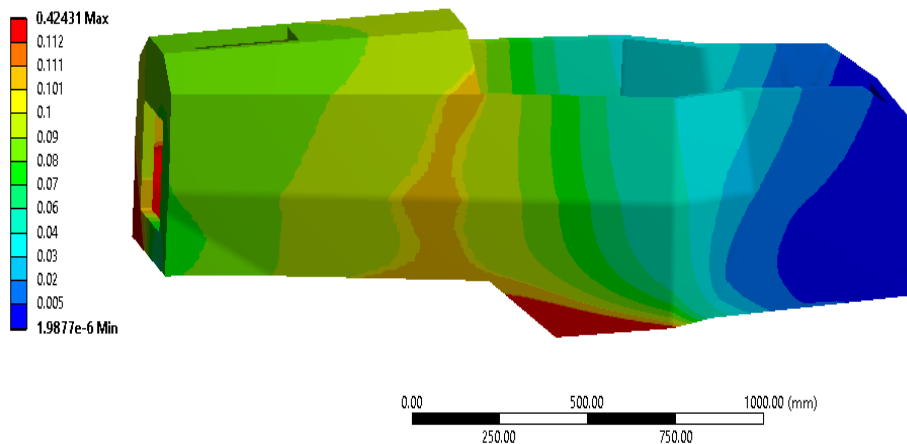
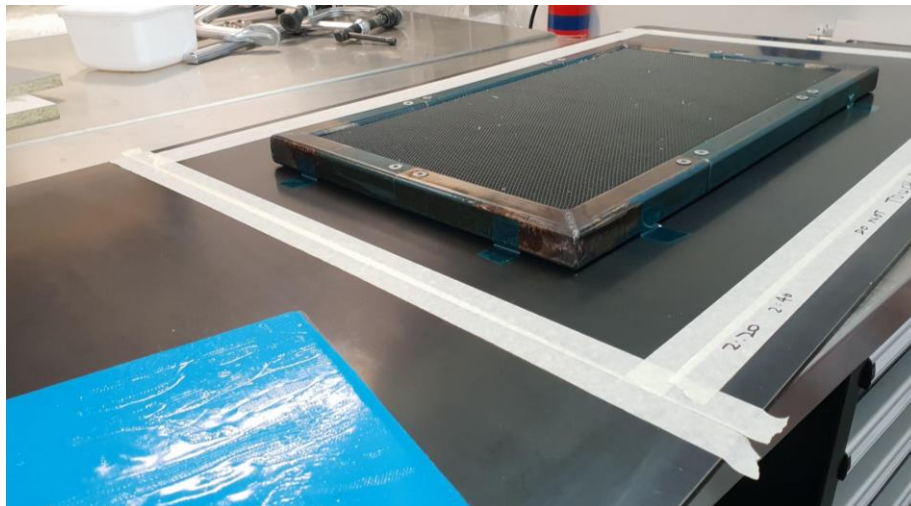


Figure 6.18: FEA results (Rigid Suspension) showing degrees of rotation along the monocoque.

# Chapter 7 Physical Testing

## Test Panel Production

All of the panels used for physical testing were manufactured in-house at Monash University using the university autoclave for prepreg curing. Special tooling was created for the manufacture of the various types of test panels, including support frames to prevent core crush phenomenon, where the core crushes inwards under vacuum pressure. The test panels were manufactured in a process matching the one used for the physical monocoque, as will be discussed in Chapter 8.



*Figure 7.1: Test panel manufacture showing core crush support frame (background) and MTA 240 adhesive film (foreground).*

The cure cycle used for the sandwich panel was completed at a temperature of 90°C and a cure time of 4 hours, with a 2°C/min ramp up rate in accordance with data sheets provided by GMS Composites and Cytec for their respective products. The autoclave bag pressure was set at 275kPa which is lower than what is normal for autoclave cured composites however was deemed lower risk with a thin aluminium mould.



*Figure 7.2: 3 point bend panel sample being loaded into the Monash University autoclave.*

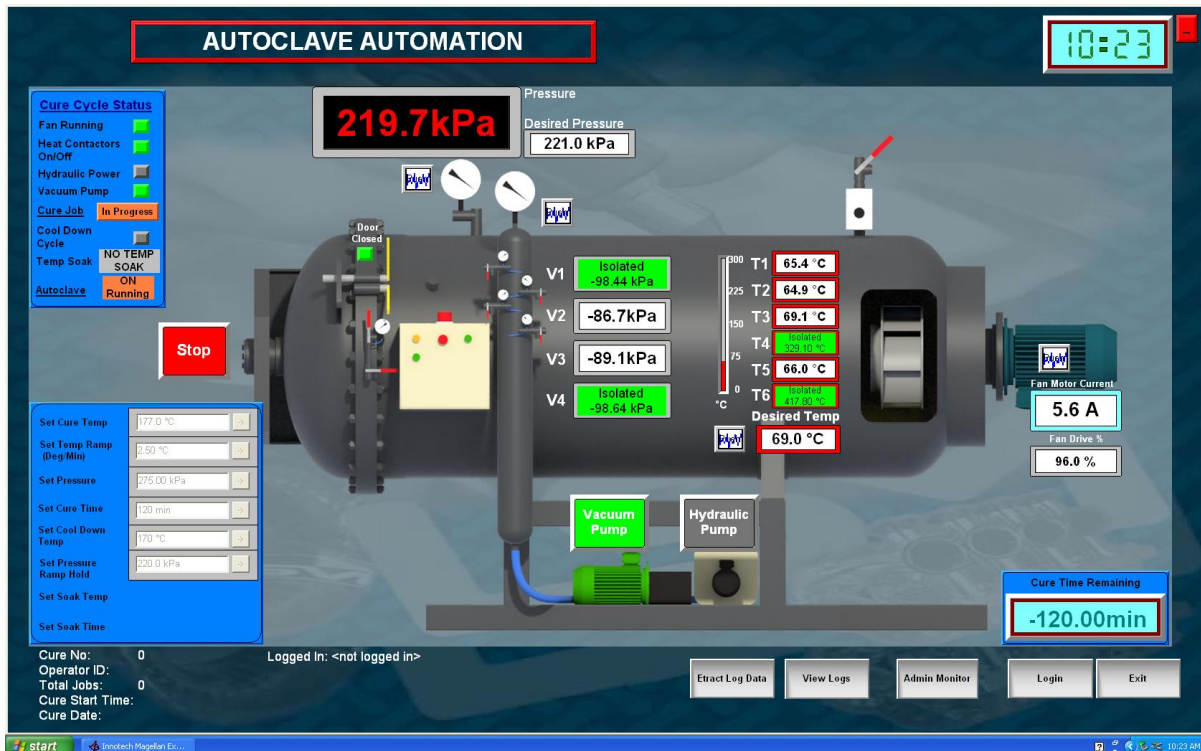


Figure 7.3: User interface of the Monash University autoclave automation software.

### 3 Point Bend Testing

The Formula Student rules specify the dimensions of the panel specimen to be tested. The panel must have minimum dimensions of 500mm x 275mm and must be supported by a rig with 400mm spacing. A load applicator with a radius of 50mm must be applied centrally on the panel. There are no specifications on the rate at which the load is applied. Previous testing in 2016 found that the panel exhibits marginally higher stiffness and failure loads at higher load rates, thus a load rate of 4000mm/min was used for all 3PB physical tests.

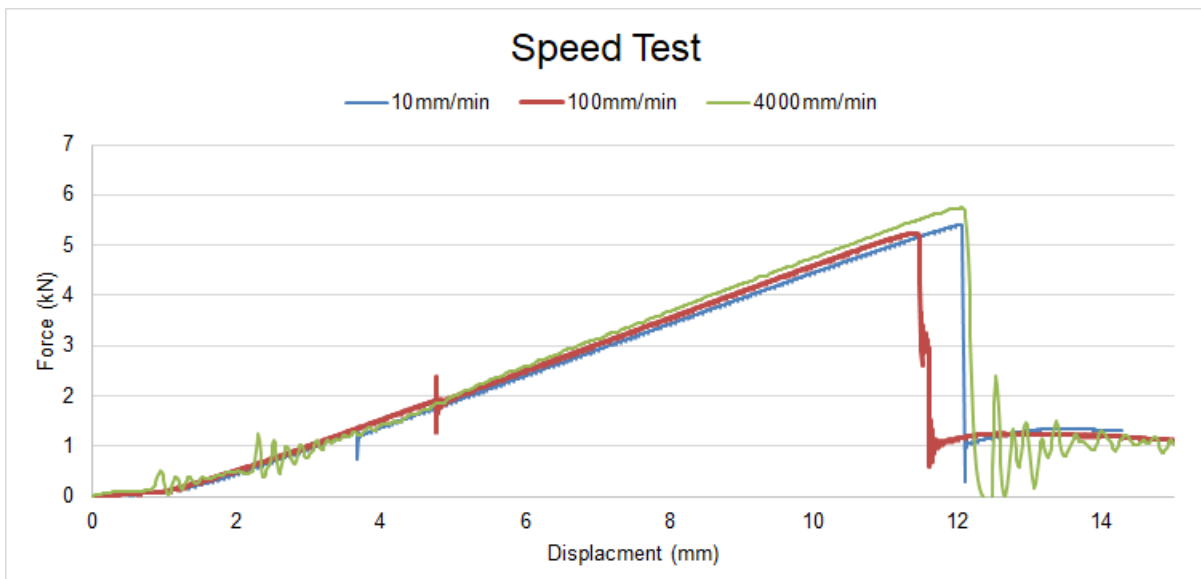


Figure 7.4: Speed test results for 3 point bending tests conducted in 2016.

The test rig for this test was constructed from welded steel components. It was found in initial calibration tests that the two panel supports (pictured in Figure 7.5 below) had too large a radius that was causing the effective panel span to reduce as the specimen deflected downwards, thus increasing the stiffness and failure load. This was rectified in later tests by welding two thin steel bars to negate this effect.

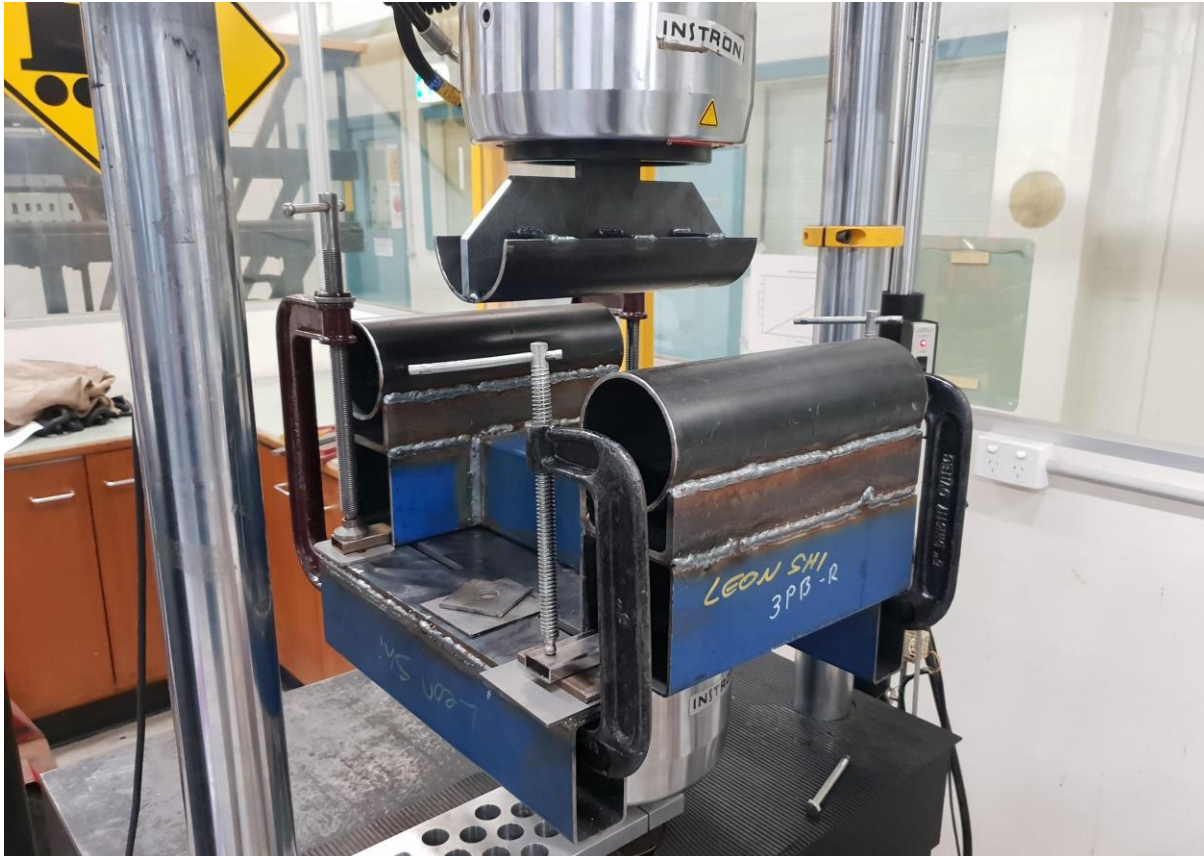


Figure 7.5: 3 point bend test rig setup on the Instron 100kN UTM at the IRT Highbay Area.

All of the physical tests for 3 point bending, perimeter shear and hardpoint inserts were performed on an Instron 100kN hydraulic powered universal testing machine located at the Institute of Railway Technology Highbay Area located at the Monash University engineering precinct. MMS team members are able to be inducted into the area and operate the equipment.

The side impact structure requires an additional test to prove that the energy absorption of the composite panel is equivalent to two baseline steel tubes up to a displacement of 12.7mm. For SAE rules this value is 19mm instead. In this test the loading rate was done quasi-statically at 5mm/min instead of the 4000mm/min for the composite panels. The test setup and results are shown in Figure 7.7. The stiffness of the steel tubes is calculated from the gradient of the linear-elastic region of the force-displacement graph, while the energy absorption value is the area under the curve up to the required deflection value. The secondary purpose of the steel baseline test is to establish the compliance of the test rig used. It compares the calculated EI from the physical test and compares it with theoretical values for the same tubing dimensions in order to establish a rig compliance value. For the composite panel tests, the actual panel stiffness is determined by as follows:



$$\text{Actual Gradient} = \frac{1}{\frac{1}{\text{Measured Gradient}} - \frac{1}{\text{Rig Compliance}}} \quad (7.1)$$

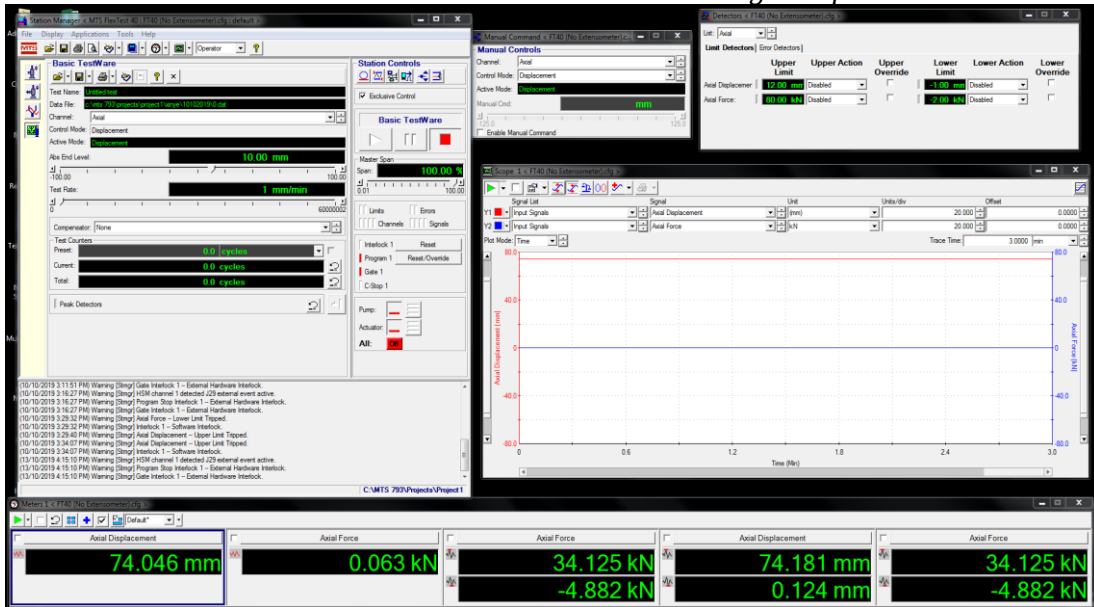


Figure 7.6: User interface of Instron computer controller.

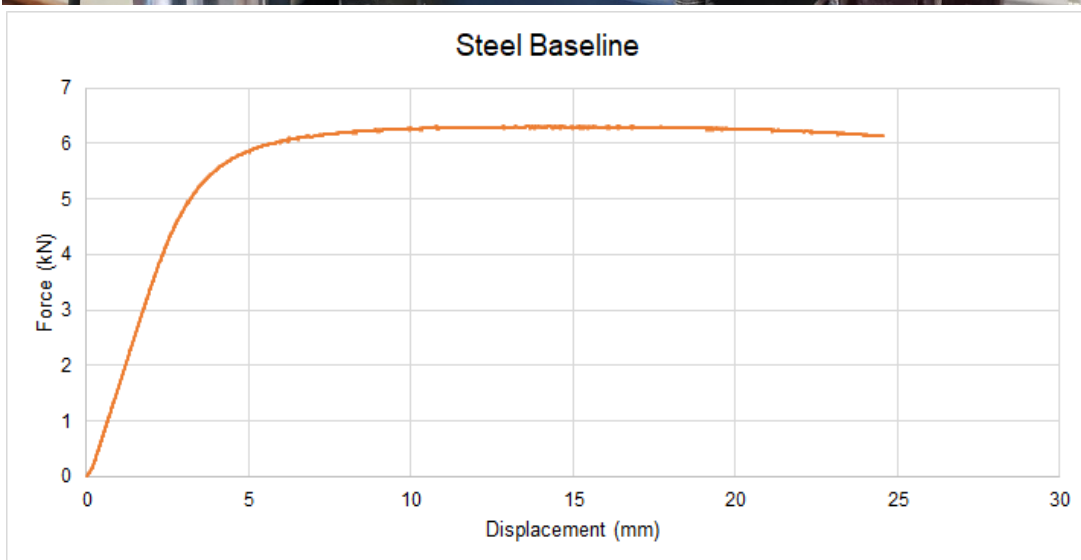


Figure 7.7: Steel baseline bend test setup (top) and force-displacement graph (bottom).

Several tests with different panel configurations were performed based off the preliminary monocoque layup schedule estimates. Some panel stackups were found to be not sufficient and were then modified to suit the needs of the monocoque.



Figure 7.8: Composite panel specimen setup on the Instron UTM (note the modified panel supports).

The results of the 3 point bend testing of composite panels concluded with 4 variants of panel stackups to be used in monocoque. These results were parsed through SES with the final monocoque geometry and all met equivalency. The force-displacement graph for all 4 panel variants are shown below in Figure 7.9. Due to an error in the machine setup the polling rate was set too low, nevertheless the data is still usable and had no effect in any regard. Note that the [24/Core/3] panel is a unique construction used solely for meeting the front bulkhead perimeter shear requirements, hence the thick outer skin but very thin inner skin.

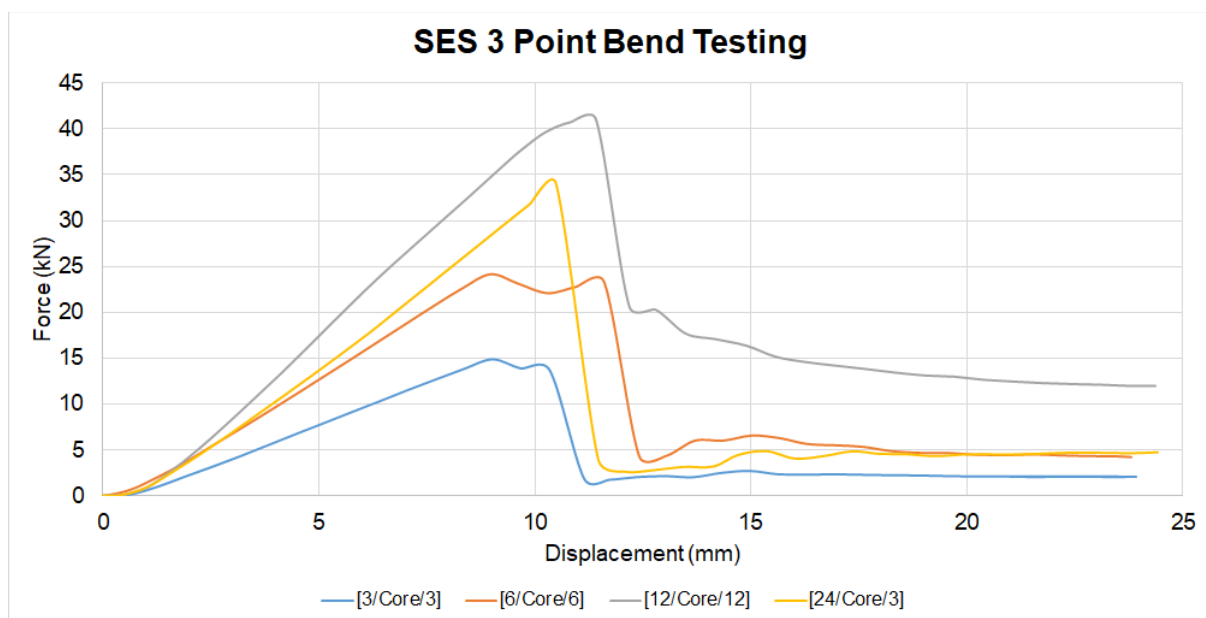


Figure 7.9: Force-displacement graph for SES 3 point bend tests.

## Comparison with Simulated Panels

Figure 7.10 below is a comparison of the different simulation tools introduced in (ref Ch5) with the physical test results. It can be seen that the FEA model achieves greater accuracy on average compared to the MATLAB script, especially for the 3 and 6 ply laminates. The maximum error for the FEA for these thinner laminates is 4.16% while for the MATLAB script the error is 12.07%.

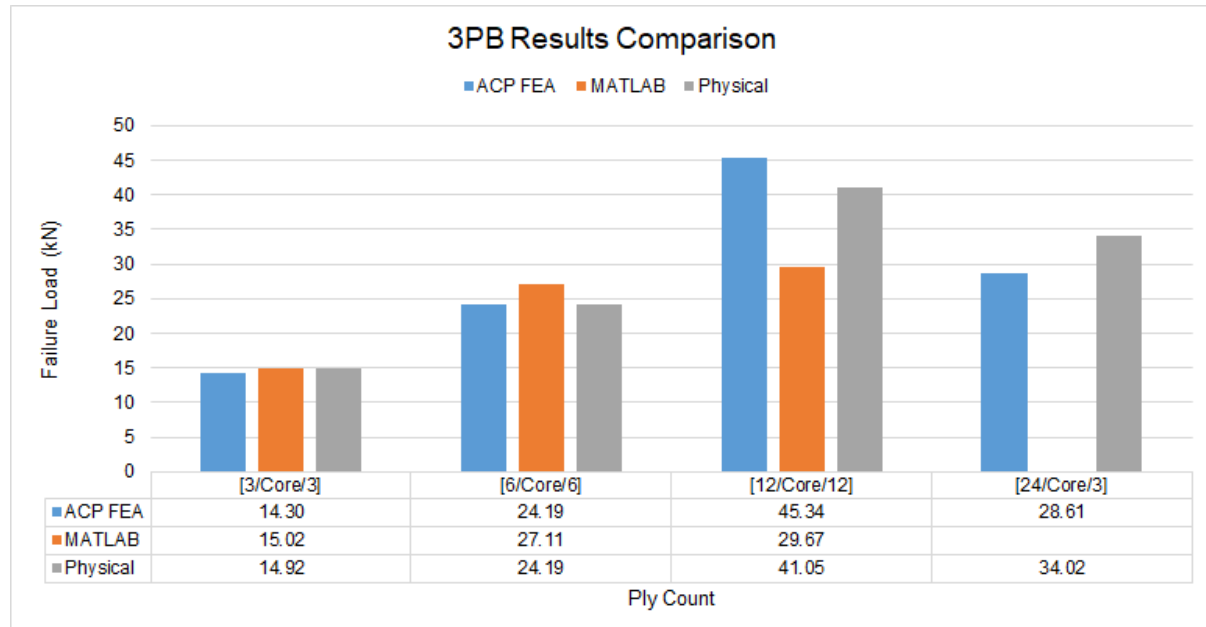


Figure 7.10: Results comparison between FEA, MATLAB and physical 3 point bend tests.

The MATLAB code breaks down for thicker laminates when the onset of the core shear dominates the panel failure mode, as can be seen with the low prediction of the 12 ply panel. In reality the core failure may not necessarily translate to the peak force the panel is able to withstand, rather the skins still have an increased load capacity to some extent over the core failure load. The MATLAB code is also only able to perform calculations on symmetric skin laminates in a composite panel. Hence the [24/Core/3] front bulkhead panel is not able to be predicted in MATLAB.

The ACP FEA model also appears to be less accurate for thicker laminates, with a 10.45% error for the 12 ply panel and 18.91% error for the front bulkhead panel. In reality the error may not be as great as it appears. For the physical 3 point bend test of the 12 ply panel, the interlock safety limits of the Instron UTM were initially set too low as they were based off the MATLAB script predicted failure load. As a result, the panel was loaded to 45kN when the interlock was tripped and the Instron UTM was shut down. The panel had not experienced a full failure at this point but had a reduced loading capacity as a result of an extra load cycle, hence on second attempt the panel failed at a reduced 41.05kN. Had the interlock value been set at an adequate value the final failure load would have been closer to the FEA predicted value.

As for the [24/Core/3] front bulkhead panel, unlike all other panels which experienced a facesheet compression failure on the top skin, because the top skin is very thick and the bottom skin is very thin, the dominant failure mode is skin tension on the bottom skin. This

failure load is dependent on the ultimate tensile strength of the prepreg CFRP. Recall that on pg. , the material properties of the EP-270 prepreg were assumed to be similar to Toray T300 prepreg. The error seen in the FEA was most likely a result of the ultimate tensile strength of the Toray T300 being lower than the EP-270. The ultimate compressive strength values appear to be very similar to each other, hence the small error for the 3 and 6 ply panels, which failed under facesheet compression.

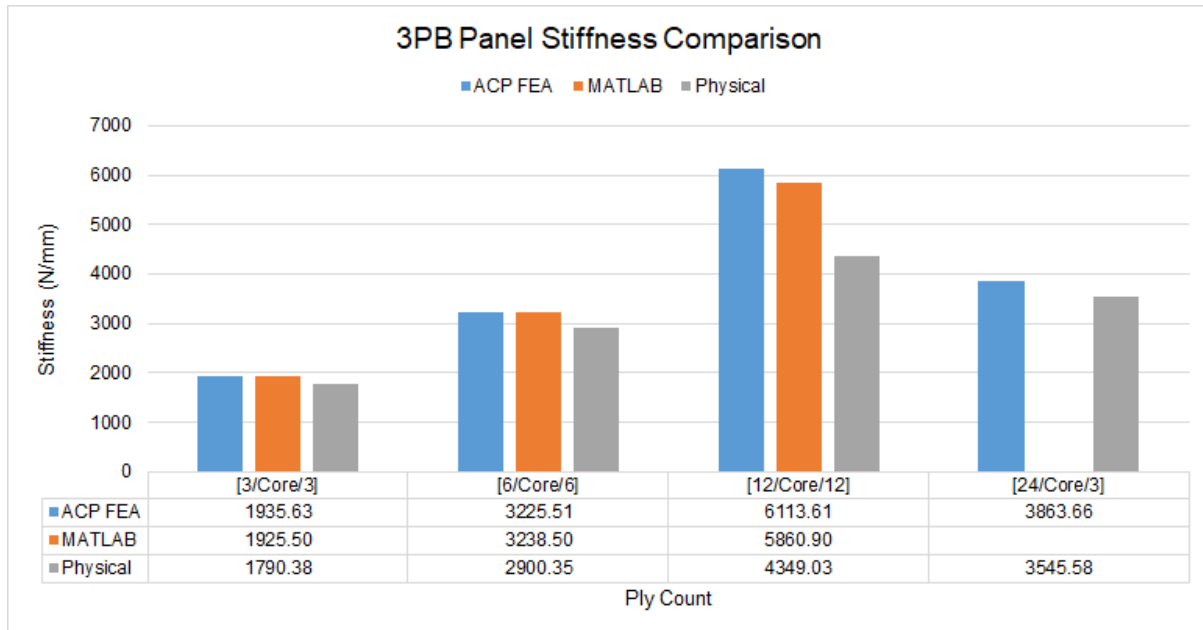


Figure 7.11: Panel stiffness comparison between FEA, MATLAB and physical 3 point bend tests.

Another comparison between the different simulation tools and physical test results for panel stiffness is shown in Figure 7.11. It can be seen that the accuracy of both simulation methods is very representative. Once again there is an outlier for the 12 ply panel which is still attributed to the double loading regime that the panel experienced in the physical test. The similarity in stiffness between both simulation models is to be expected as the calculation is purely dependent on the geometry of the panel.

## Perimeter Shear Testing

As with the 3 point bend tests, the Formula Student rules specify the dimensions of the panel specimen to be tested. The panel must have minimum dimensions of 100mm x 100mm and must be supported by a rig with a 32mm hole lined up coaxially with the load applicator, a flat punch with a diameter of 25mm. Again, there are no specifications on the rate at which the load is applied, with previous 2016 tests showing a load rate of 5mm/min providing the most optimum results for SES.

The results of perimeter shear tests with the same laminate stackups as the ones from the SES 3 point bend tests are plotted on the force-displacement graph in Figure 7.13. The force peaks correspond to the two laminate skins, the first peak being the top skin and the second peak being the bottom skin.

The perimeter shear results proved to be the limiting factor in terms of minimum ply stackups for the monocoque. All of the 3 point bend test results produced equivalencies of 125% or

greater for virtually all primary structure panels in SES, while the perimeter shear requirements for the front bulkhead, front bulkhead support and side impact structure were met with much smaller margins. Nevertheless, the results of both the 3 point bend tests and perimeter shear tests provided enough data for the team to determine a final chassis layout schedule moving into the production phase.



Figure 7.12: Perimeter shear test setup on the Instron UTM.

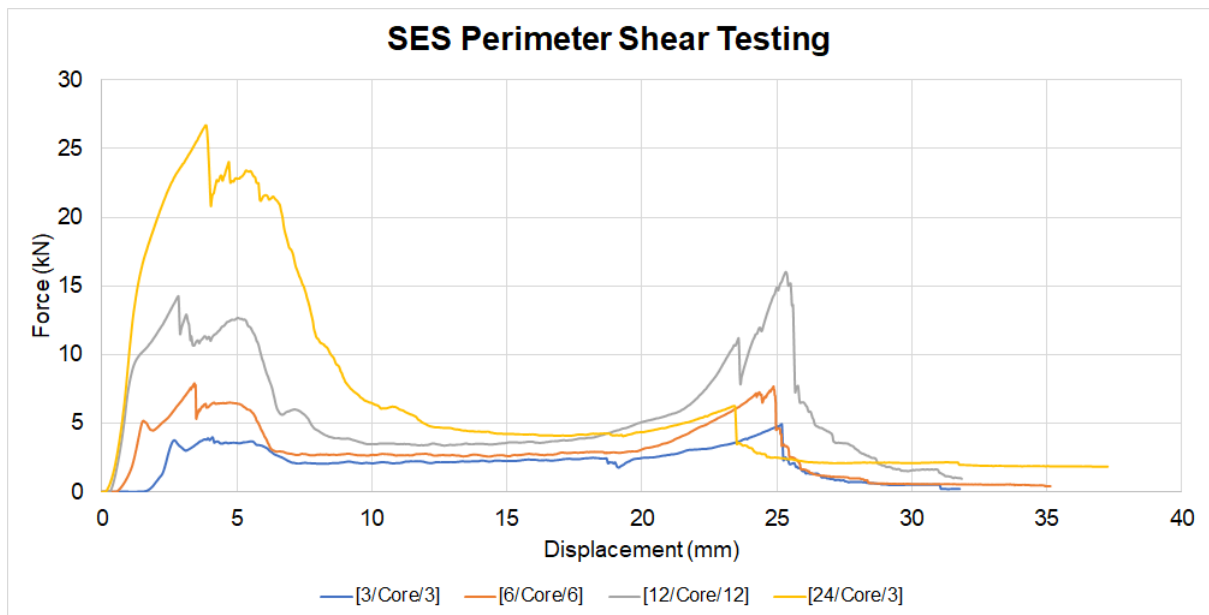
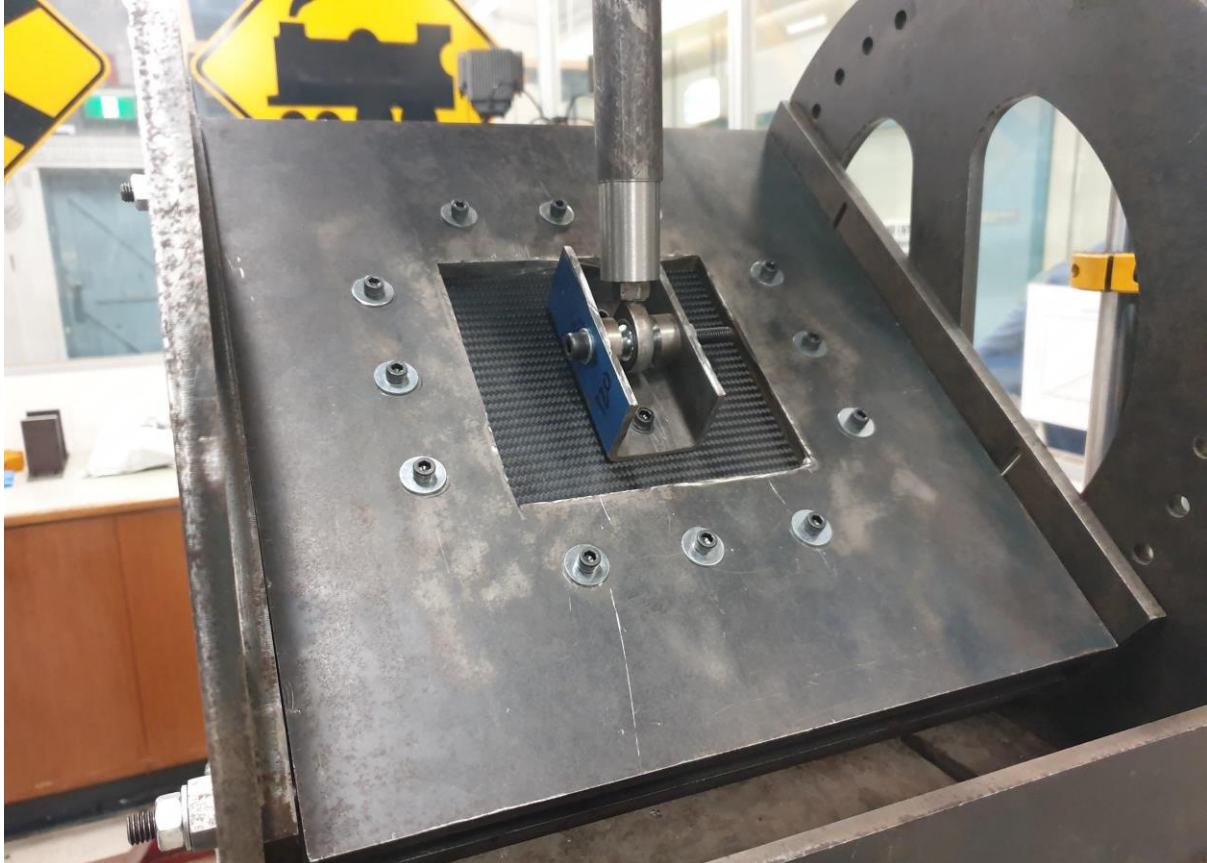


Figure 7.13: Force-displacement graph for SES perimeter shear tests.

## Hardpoint Insert Testing

The hardpoint insert pull-out tests were completed on the Instron UTM using a test rig developed by the chassis section in 2015. The test rig allows for a range of panel pull-out scenarios to be tested by adjusting the angle of the panel support structure within the rig. The adjustment holes can be seen in Figure 7.14 below. The loading rate for these insert pull-out tests were set at 5mm/min.



*Figure 7.14: Insert pull-out test rig setup on the Instron UTM for inclined loading.*

As mentioned on pg. , two standard sized insert groupings were chosen, one with a diameter of 10mm and one with a diameter of 20mm. The inserts were tested at 3 different loading scenarios to give an accurate indication of the loading these inserts would see on the monocoque chassis. In total, 8 panels were physically tested with the following parameters as shown in Table 7.1. To keep things consistent, all of the tested panels had a 6 ply layup schedule matching the SIS. This layup schedule would be retained on the actual monocoque with added reinforcement patches where necessary. The force-displacement graph results of the tests are shown in Figure 7.15.

All of the inserts performed at a suitable level to be used as a wishbone attachment point or harness attachment in the monocoque. The initial stiffness in the linear-elastic region for all tests was also above the targeted 3kN/mm to ensure there would be minimal compliance in the suspension system at this component level. The force-displacement graph does reveal evidence of panel slip in some tests, most notably Panel 1 (orange curve in Figure 7.15) where the gradient of the curve reduces for higher displacement levels. This is a potential source of

Table 7.1: Hardpoint insert physical testing parameters.

Panel number	Insert diameter (mm)	Insert loading angle (degrees relative to plane of panel)	Insert group spacing (mm)
1	10	90	65
2	10	90	65
3	10	0	65
4	10	0	65
5	10	40	65
6	10	40	65
7	20	40	65
8	10	40	50

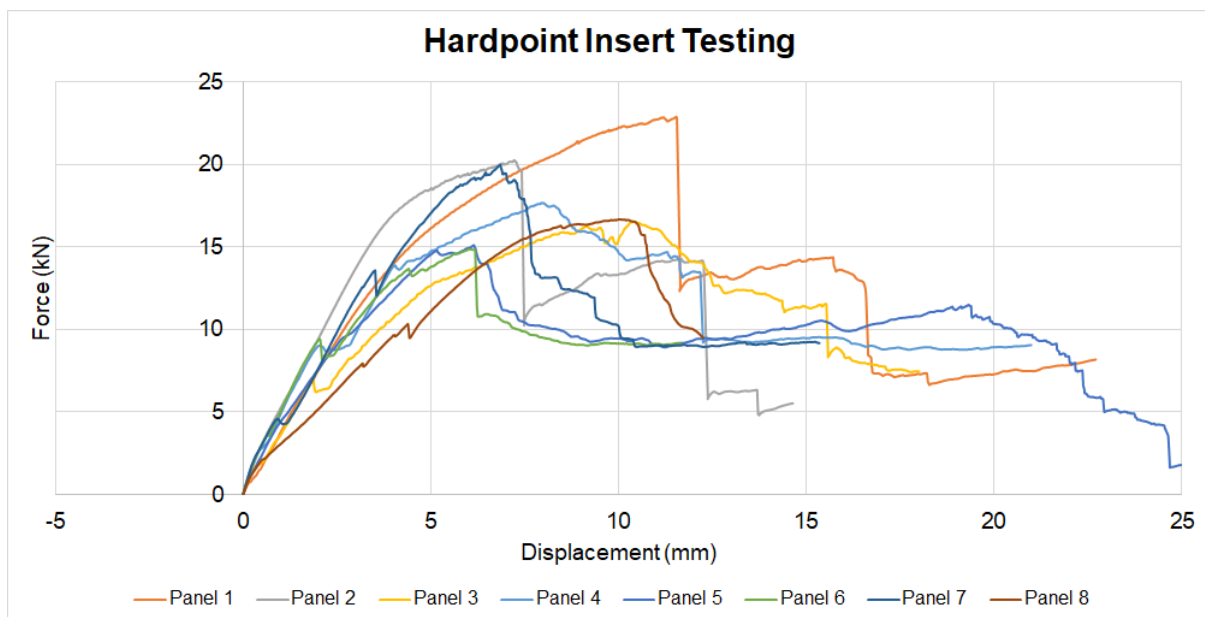


Figure 7.15: Hardpoint insert force-displacement graph.

compliance that is inherent to the current hardpoint insert testing rig. It is also worthy to note that Panels 1 and 2, 3 and 4, and 5 and 6 were identical panel setup pairings in order to increase the sample size of the data collected. While the variance in ultimate failure loads are within reason, the stiffness of the panels was noted to increase significantly on the second panel loading attempt. This is further indication of compliance in the test rig. The first time the panel was loaded at a given loading angle always produced the lowest stiffness gradient, and subsequent ones would see a significant increase. While this did not negatively affect the results of the test for the purposes of determining suitable inserts for the monocoque, it does suggest that improvements should be made to achieve more consistent testing results in the future.

## Comparison with Simulated Hardpoint Inserts

The comparison of insert performance between those predicted in MATLAB in (ref Ch5) and the physically tested hardpoint inserts is shown below in Figure 7.16. It can be seen that the error in the predictions is quite large and is under predicting out-of-plane pull-out forces and over predicting in-plane and inclined loads.

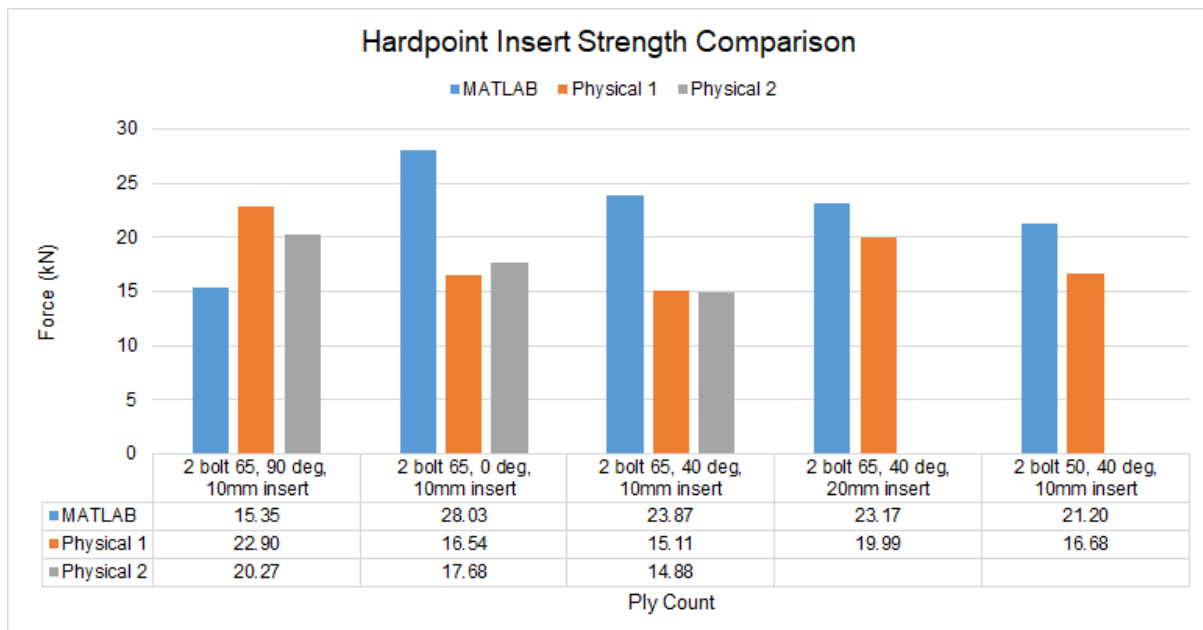


Figure 7.16: Results comparison between MATLAB and physical hardpoint insert pull-out tests.

The comparison of insert stiffnesses shown in Figure 7.17 also shows large errors in the MATLAB prediction, however it must be noted that the Insert Design Handbook does not explain the calculation of stiffness in detail and instead a rudimentary spring model was used instead. It also highlights the likely rig compliance mentioned earlier, with subsequent physical tests showing increased insert stiffness.

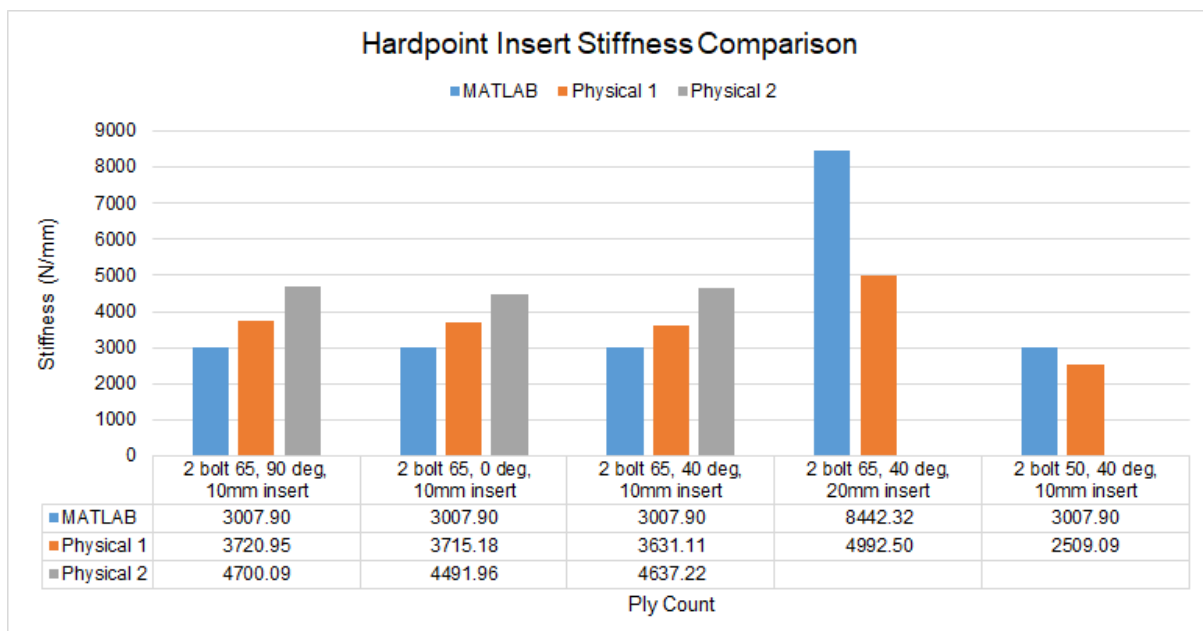
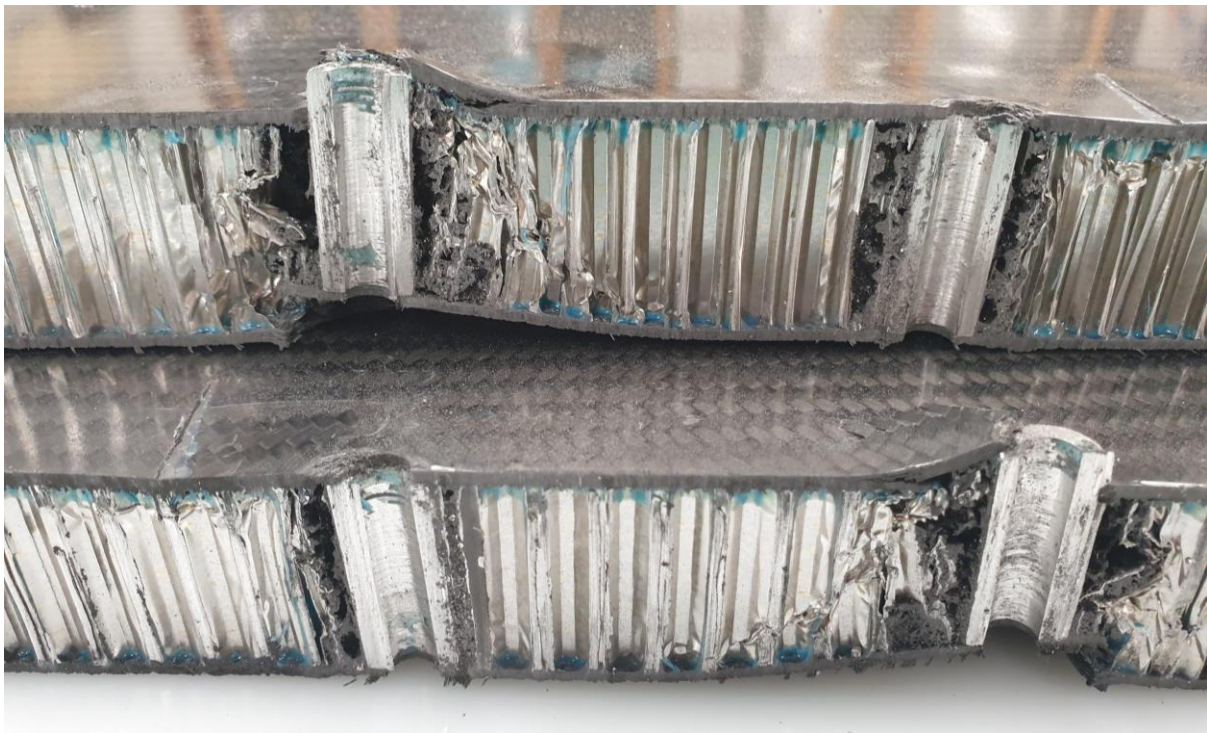


Figure 7.17: Insert stiffness comparison between MATLAB and physical hardpoint insert pull-out tests.



Despite the large errors in predictions, the tested failure loads and stiffnesses all met requirements for the wishbone attachments. To gain a better understanding of predicting insert loads, the MATLAB script was revisited and adjustments were made to better improve the model.

For the in-plane loading test samples, it was observed that the insert did not fail due to in-plane tensile or compressive loads, rather it was out-of-plane pull-out created by the moment of loading the panel with a clevis at an offset distance. It was also found that the predicted failure loads were extremely sensitive to the effective potting radius and real potting radius. Upon inspection of the cross section of some of the tested panels, it was seen that the potting radius created by the foaming adhesive was larger than the recommended calculation in the Insert Design Handbook.



*Figure 7.18: Detailed inspection of the hardpoint insert potting from the foaming adhesive.*

Part of this reason is that the aluminium cylindrical hardpoint inserts used here are not the conventional potted insert design using liquid potting compounds. A study on carbon tube inserts with similar geometry to the aluminium cylinders used here determined that the effective potting radius was closer to a value of 10% greater than the insert radius [36].

Fine tuning of the effective potting radius value and implementing the calculation of a moment induced pull-out failure yielded the following failure loads shown in Figure 7.19. While the error compared to physical tests is greatly reduced, 3 separate models for were needed to model the failure loads accurately. The outcome of this is that we are able to predict the failure loads of the hardpoint inserts but only for specific conditions. If the team were to change up the design the predictions would most likely no longer be valid. Nonetheless, the MATLAB script can still be used as a very easy and quick to use design tool for very early estimates of hardpoint insert sizing, with physical testing still required as final validation before confirming a design.

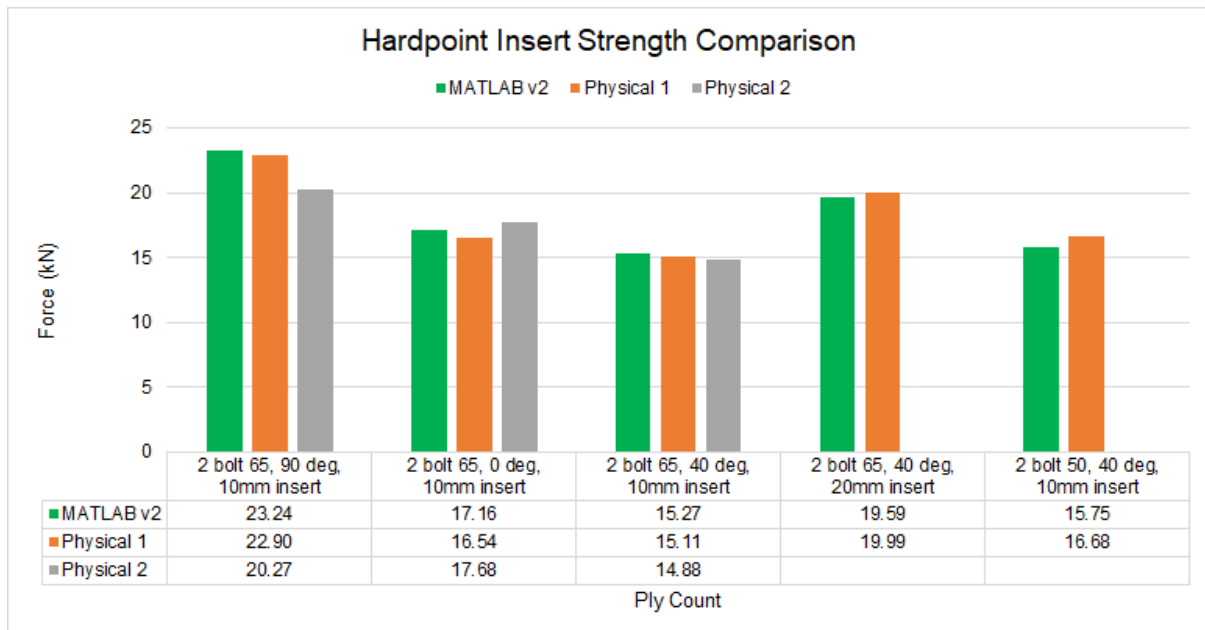
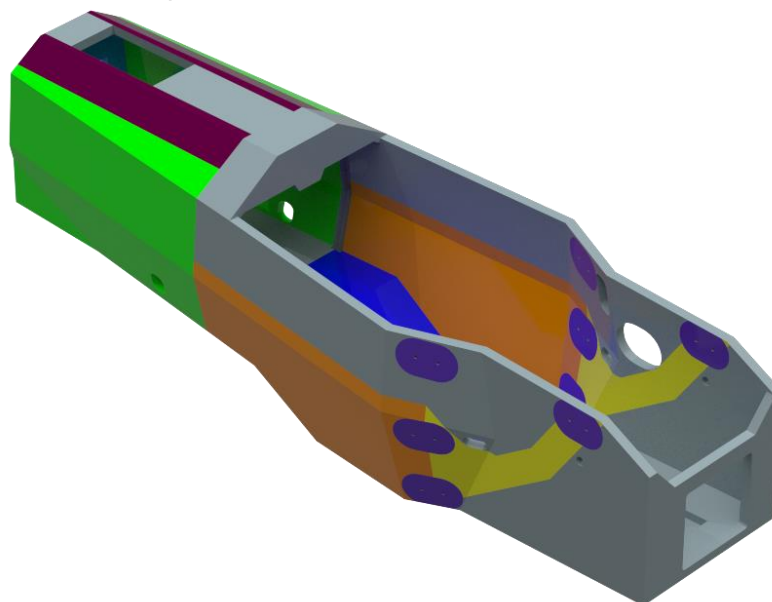


Figure 7.19: Results comparison with modified MATLAB model.

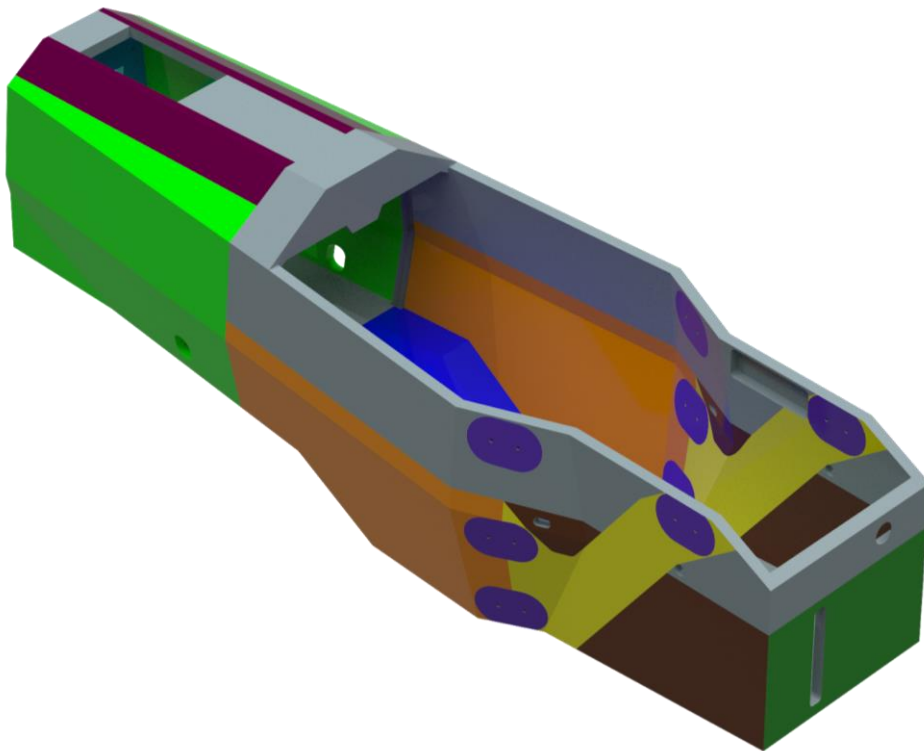
## Final Chassis Layup Schedule

Following the completion of all of the physical tests, the final chassis layup schedule could be determined ready for manufacturing. The individual layup schedules for both the combustion and electric vehicle monocoques are shown below.



Panel Region	Ply Count (outer/inner)
Front Bulkhead	24 / 3
Front Bulkhead Support Structure	3 / 3
Front Roll Hoop Bracing	6 / 6
SIS Vertical	6 / 6
SIS Horizontal	6 / 6
Main Roll Hoop Bracing Support	12 / 12
Other	3 / 3

Figure 7.20: Final chassis layup schedule for the combustion vehicle.



Panel Region	Ply Count (outer/inner)
Front Bulkhead	24 / 3
Front Bulkhead Support Structure	3 / 3
Front Roll Hoop Bracing	6 / 6
SIS Vertical	6 / 6
SIS Horizontal	6 / 6
Main Roll Hoop Bracing Support	6 / 6
Accumulator Side Protection	6 / 6
Tractive Side Protection	6 / 6
Rear Impact Protection	6 / 6
Other	3 / 3

Figure 7.21: Final chassis layup schedule for the electric vehicle.

# Chapter 8 Production

## Manufacturing Proof of Concept

In order to determine that the selected hybrid manufacturing concept from pg. would be feasible for the team, a small scale front bulkhead section of the monocoque mould was produced as a 'proof of concept'. The construction and design of the test piece aimed to mimic the final mould design as much as possible, with slots and tabs to join panels and silicone sealant to close off any edge gaps. Outsourcing of the laser cutting and folding of the aluminium sheet for the test piece was done with Laser3D, a former sponsor of the team.



*Figure 8.1: Mould test piece as constructed.*

The construction of the mould was found to be very straightforward and not time consuming, with very good accuracy being achieved and no post-work required. A simple prepreg skin was laminated into the mould, and the final results were very encouraging. The surface finish was equivalent to or better than any other moulded composite components seen on the team previously, but with the major advantage of little to no mould preparation work. The results of this mould test validated that the hybrid manufacturing concept would be a viable solution for the team moving into the manufacturing period.

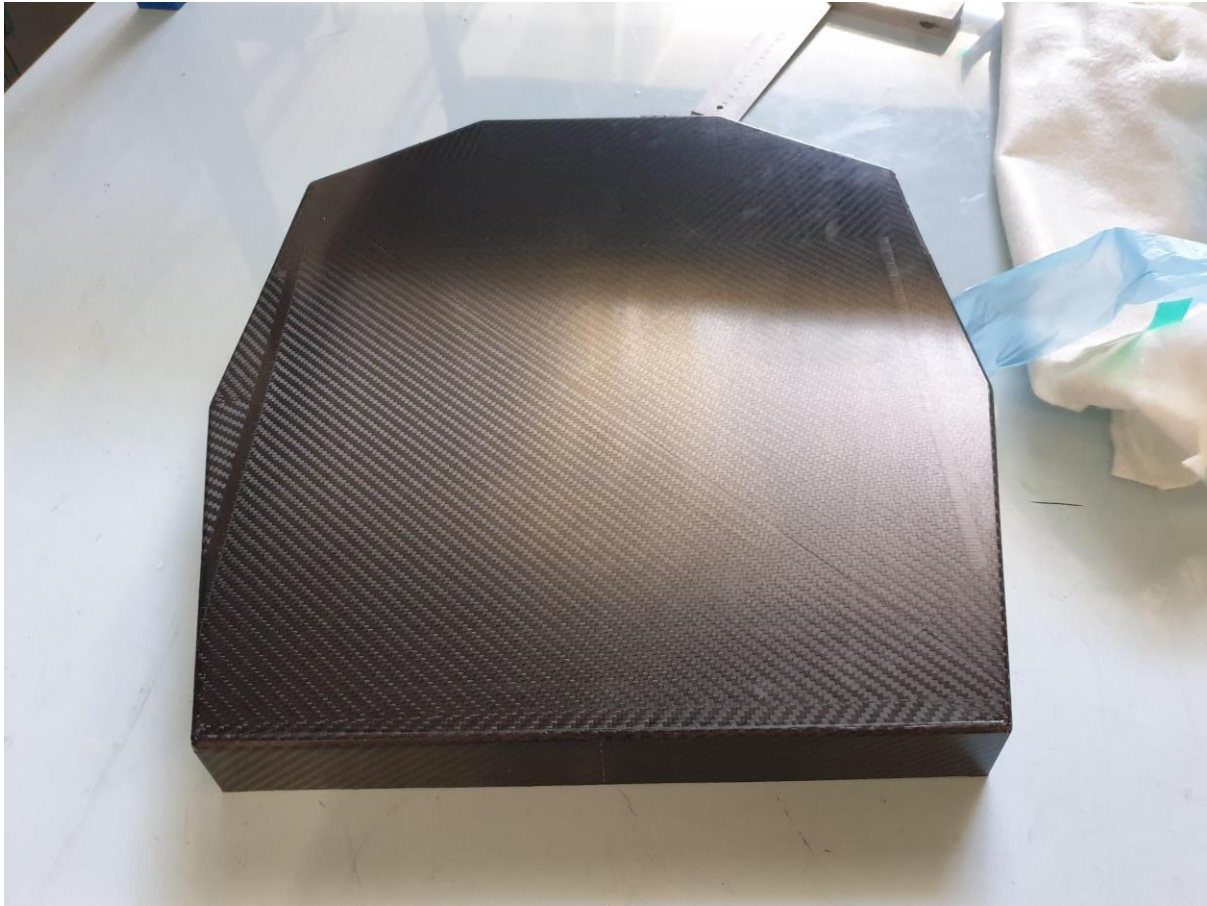


*Figure 8.2: Test piece outcome.*

## Manufacturing Procedure

### Mould Design and Construction

With the hybrid concept selected and the proof of concept proven to be successful, the design of the final mould began. The mould was designed as 12 laser cut and CNC press brake folded 3mm aluminium sheet metal components that assemble together with tabs, corresponding slots and joining brackets. The mould included laser cut bolt holes so as to accurately locate hardpoints and mould inserts which allow for necessary holes in the monocoque such as for suspension componentry, powertrain and driver controls. Steel support bracing was also added over the open cockpit section to prevent warping during high temperature autoclave cure cycles and aluminium angle closeouts were added to prevent the core crushing.

A lot of care was taken to ensure that every individual panel section would be able to be demoulded; this included widening slots for tabs so that there would be room for the panels to move against each other when attempting to assemble or disassemble them. Furthermore, the panels were designed to be interchangeable between the electric and combustion monocoques, which shared identical front sections but slight deviations at the rear for differences in powertrain packaging.

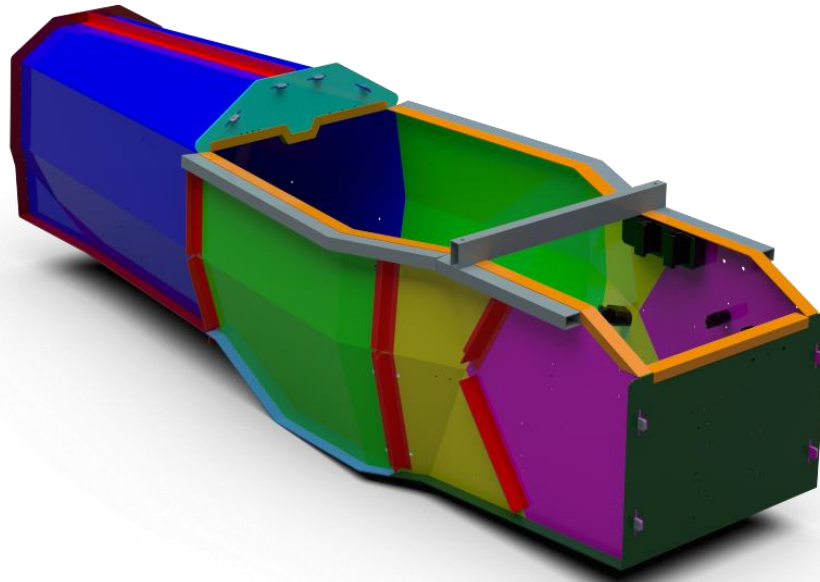


Figure 8.3: CAD of M19-E monocoque mould.

The final assembly of the mould was completed very efficiently, within two days, and as expected. This represented a significant reduction in time taken for tooling assembly over the moulded concept and even compared to a steel spaceframe chassis, where laser cut steel tooling jigs require approximately a week of welding to be fully assembled and ready for production.

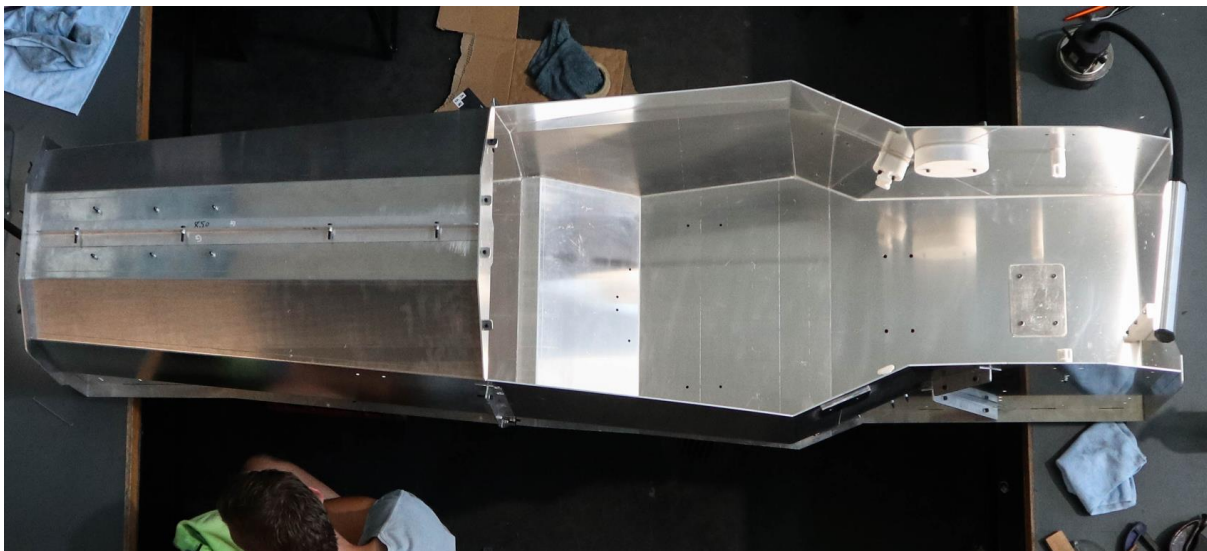


Figure 8.4: Assembled mould for M19-C.

## Timeline

The initial manufacturing timeline proposed during the early design phase saw the two monocoques being manufactured back-to-back, sharing the same mould components with small sections substituted out where required. The key deadline that the chassis section had to work towards was the *rolling* milestone on 30 May 2019, which demanded a fully functioning chassis with driver controls and suspension subsystems assembled onto it. Working backwards from this date and allowing for finishing and assembly time saw the first

monocoque needing to be completed by 18th April and the second by 15th May. Approximately four weeks of manufacture time was allocated to each monocoque, which was based on other experienced Formula Student teams' who require 3 weeks for one monocoque. The extra week was allocated as a safety margin for any issues which may potentially arise. Since MMS had a relatively low level of composite manufacturing experience.

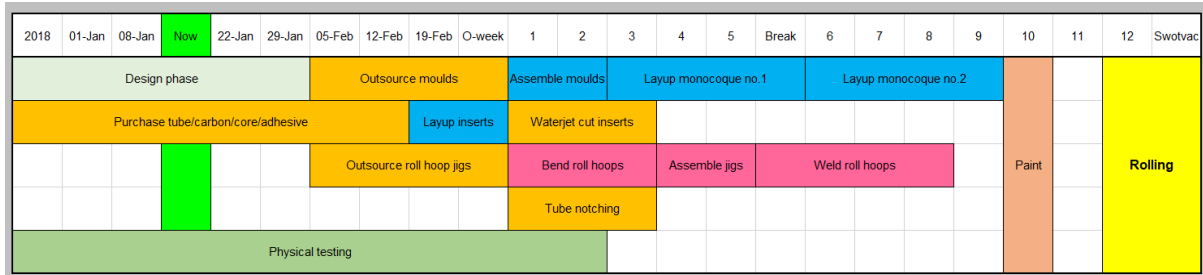


Figure 8.5: Proposed manufacturing timeline.

In reality, a number of setbacks, some that were manageable such as delays in hardpoint insert testing and some that were out of the team's control such as outsourcing purchasing delays, meant that this timeline was not achievable. In order to still meet the rolling deadline, a revised, more aggressive and higher risk timeline had to be developed and implemented. This involved outsourcing two separate moulds for each car and manufacturing the two monocoques simultaneously but staggered by 1-2 weeks. As a result, the two manufacture time for both monocoques occurred in a period of just under 6 weeks.

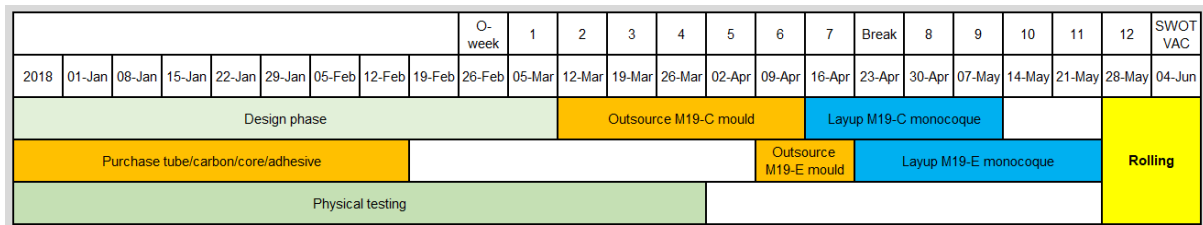


Figure 8.6: Revised manufacturing timeline.

## Production

The production of an autoclave-processed composite sandwich panel structure can be divided into three separate cure stages:

1. Outer skin cure
2. Core and insert bonding
3. Inner skin cure

The general procedure for an autoclave cured composite component is depicted graphically below. Apart from the mould tooling and composite laminate, a number of ancillary consumables are required to complete the vacuum bagging component of the layup, each of which are crucial for a successful cure.

For management of the production schedule, a rudimentary composite ply book was generated which outlined each individual step of the entire manufacturing procedure. It would specify what material would be laid into the monocoque at each step, when a debulking process was required and when an autoclave cure was scheduled. It is necessary to place down plies in small quantities as opposed to everything in one operation to allow for laminate

consolidation through the debulking process, to compact all the individual plies and to remove trapped air in between.

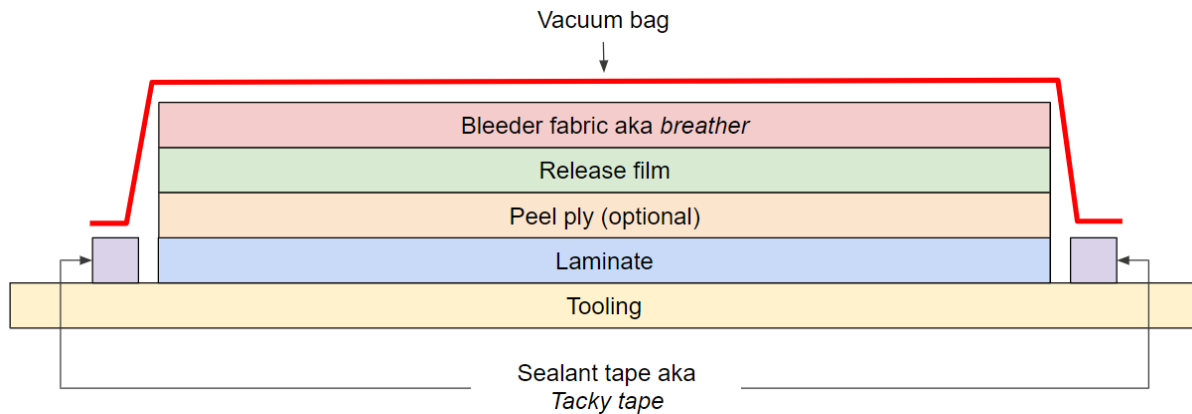


Figure 8.7: Typical autoclave layup procedure.

The ply book is organised sequentially in steps as opposed to dates and deadlines. This was left to the discretion of the part designer and section management during the production period.

Step:	1	DEBULK	2	3	4	5	6	7
Angle:	0		45	quasi 0/45	quasi 0/45	quasi 0/45	quasi 0/45	quasi 0/45
Material:	EP270		EP270	2xEP270	2xEP270	6xEP270	2xEP270	2xEP270
Note:	Surface ply		2nd ply all	FRHB	SIS vert	FBH	MRHB	SIS hori
Step:	8	DEBULK	9	10	DEBULK	11	12	13
Angle:	quasi 0/45		quasi 0/45	quasi 0/45		quasi 0/45	quasi 0/45	quasi 0/45
Material:	6xEP270		2xEP270	2xEP270		6xEP270	4xEP270	6/9xEP270
Note:	FBH		HP/EP reinf.	MRHB		FBH	MRHB	MRH reinforce
Step:	14	DEBULK	15	16	DEBULK	17	18	19
Angle:	quasi 0/45		0	45		CURE @275kpa, 90degC, 4hrs	Assemble dash	quasi 0/45
Material:	2xEP270		EP270	EP270		3xEP270		
Note:	FBH		Inner ply all	All >3ply skins		Dash		
Step:	20	Assemble FRH	22	DEBULK	23	24	25	26
Angle:	-		Offcut		Offcut	-	Assemble core	Assemble inserts/EP
Material:	MTA240		2xEP270		2xEP270	MTA240		
Note:	FRH		FRH		Edge overlaps	All		
Step:	27	DEBULK	28	29	30	DEBULK	31	32
Angle:	CURE @150kpa, 80degC, 5hrs		-	45	0		quasi 0/45	quasi 0/45
Material:			MTA240	EP270	EP270		6/9xEP270	6xEP270
Note:			All	All >3ply skins	Inner ply all		MRH reinforce	MRHB
Step:	33	DEBULK	34	35	36	37	DEBULK	38
Angle:	quasi 0/45		quasi 0/45	quasi 0/45	quasi 0/45	quasi 0/45		45
Material:	2xEP270		2xEP270	2xEP270	2xEP270	2xEP270		EP270
Note:	HP/EP reinf.		SIS hori	MRHB	SIS vert	FRHB		2nd ply all
Step:	39	DEBULK	40					
Angle:	0		CURE @275kpa, 90degC, 4hrs					
Material:	EP270							
Note:	Surface ply							

Figure 8.8: Ply book for the production of the M19-C monocoque.



## Outer Skin Cure

All of the individual laminate plies were cut by hand. To ensure accuracy and precision of the cuts, a set of cutting instructions and laser cut card paper templates using facilities at Monash MADA were devised. Each individual ply was modelled in Siemens NX 12.0 CAD and nested together onto the footprint of the prepreg CFRP roll. This would be used as a cutting guide on the actual prepreg roll in order to minimise wastage. The laser cut paper templates, which included orientation guides for alternating ply angle cuts, would be used to trace out the patterns onto the roll of prepreg.

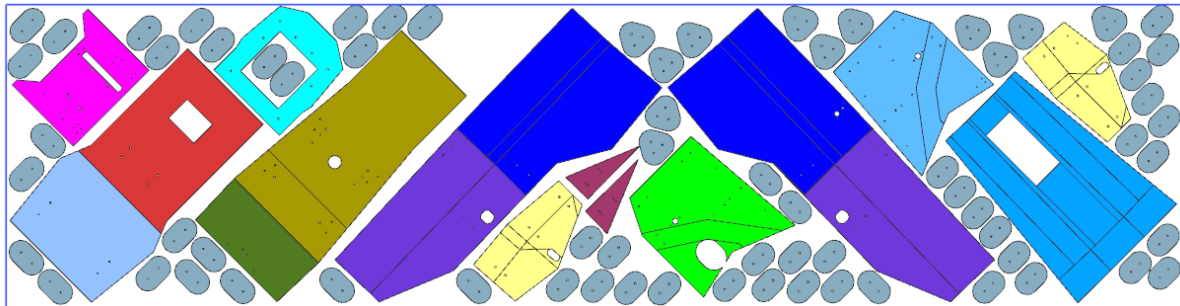
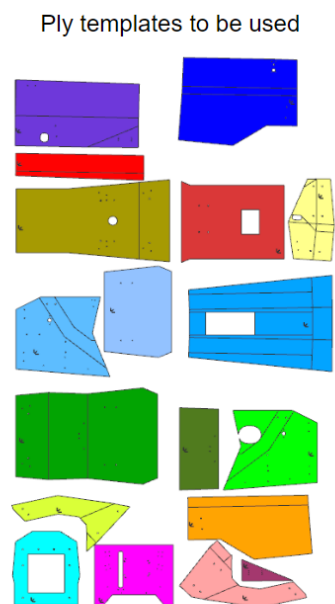


Figure 8.9: Composite plies nested onto the prepreg CFRP roll in NX 12.0.



### Instructions:

1. Cut off roll length for each 'group' one at a time. Keep the main prepreg roll in the freezer as much as possible.
2. The ply templates used for the outer skin of C-car will have 'OUT' printed on them. The ones labeled 'IN' will not be used for now.
3. Use a ruler and black permanent marker (no paint pen!) to mark out lines, using the paper template as a guide. Be careful not to rip or damage the template.
4. Label each ply either '0 deg' or '45 deg' on the polyethylene sheet side
5. Cut the outer profile of each ply but leave any small bolt holes uncut. Make sure the location of the holes is marked clearly with a marker (use a solid dot and a cross symbol)
6. Each 'group' of plies is to be stored in a sealed vac bag (use Specialised Spaces stock, keep track of how much is used) with silica gel packets in them. They must be stored flat in the freezer (put cardboard underneath it to make it flat)
7. Don't peel back any of the backing films and avoid puncturing the prepreg!

Figure 8.10: Cutting instructions cover sheet with instructions.

The plies were sized and shaped to fit into the mould with relative ease. Repositioning of the mould upside down was required to assist in getting to difficult to reach areas such as the roof of the nose section. It was important to lay out the workspace to give adequate working conditions and lighting was set up to increase visibility when working inside the mould. The final outer skin, once fully vacuum sealed, was taken to Tickford Racing's composite autoclave facilities in Campbellfield, Victoria for curing.



Figure 8.11: Outer skin during layup.

## Core and Insert Bonding

The insertion of the aluminium honeycomb core into the monocoque requires preparation and planning. Because of the tight and sharp corners of the geometry, it is not possible to bend the core into position. It is therefore necessary to cut and chamfer the core to fit into shape. This was achieved with a variety of rotary cutting tools such as angle grinders, die grinders and circular saws.

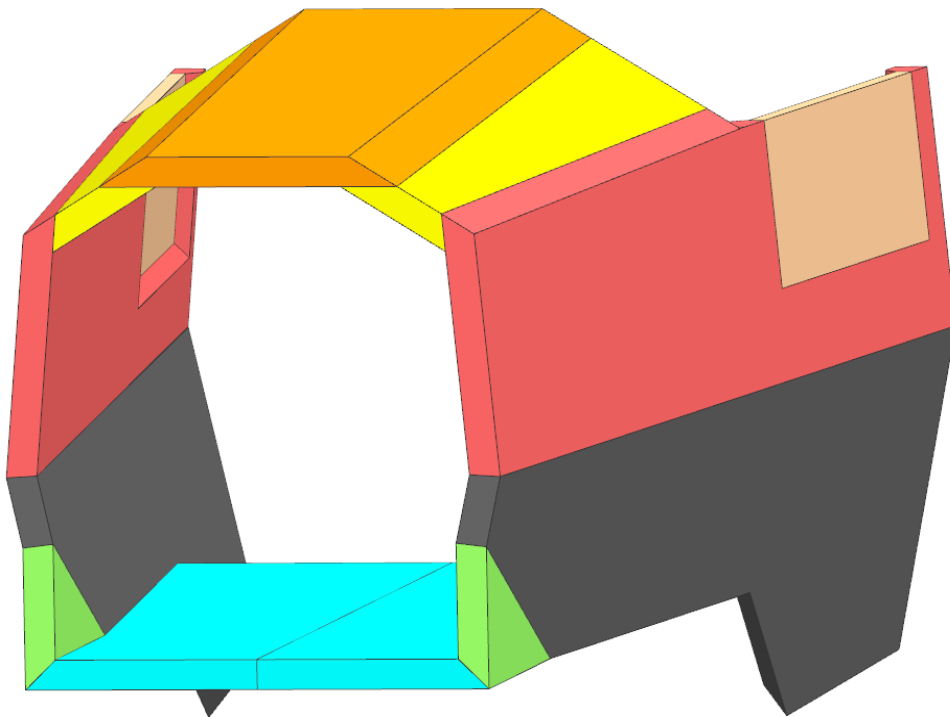
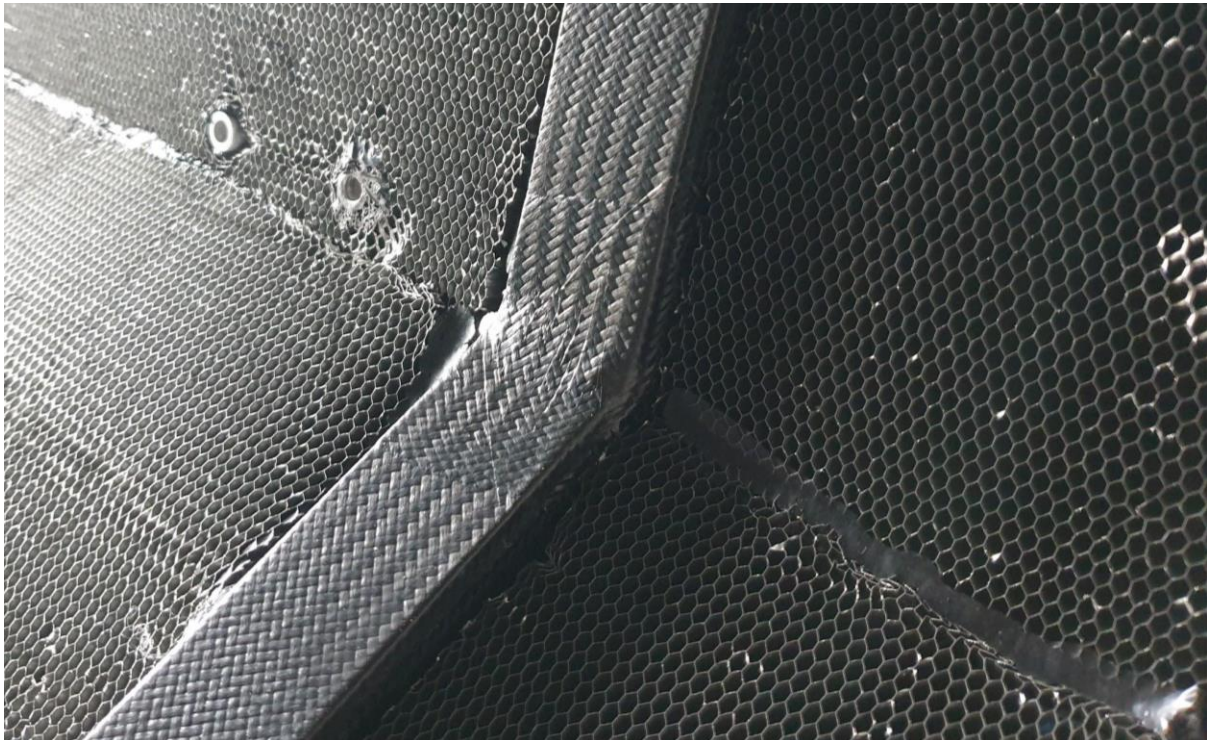


Figure 8.12: Core chamfering geometry.

Bonding the core to the cured outer skin requires the use of the MTA-240 adhesive film for the core-skin bond, while Hexcel HexBond 212-NA foaming adhesive film was used to 'splice' individual pieces of core together. This particular type of adhesive would expand in volume during a heat cure cycle, which would fill the gap in the honeycomb splices and create a strong bond for transferring loads from one section of core to another.

In addition to core bonding, the aluminium hardpoint inserts and front roll hoop also have to be bonded and laminated into the monocoque. The hardpoints are inserted into the core using foaming adhesive to bond to the core cell walls, whilst the front roll hoop is glued in using Plexus MA-420 structural MMA adhesive before being laminated in by several plies of prepreg carbon.



*Figure 8.13: Front roll hoop, core and inserts cured and bonded in.*

## Inner Skin Cure

The procedure for the final inner skin cure was very much the same as the outer skin. The same style paper templates and cutting guides were used for hand cutting the carbon plies, the debulking schedule in the ply book was adhered to and curing again took place at Tickford Racing.

## Demoulding

The final demoulding of each monocoque was very straightforward due to the flat panel nature of all the mould pieces. The smooth aluminium surface finish made for a very non-stick surface, further compounding the ease of panel removal. The quality of the surface finish was excellent given how little surface preparation was required.



Figure 8.14: Vacuum bagging process for the mould.

Despite setbacks, both monocoques were completed by the rolling deadline as originally scheduled, a major milestone for the new 2019 cars.



# WE'VE GOT TWINS!

24.05.2019

We are proud to announce the arrival of two monocoques.  
 Measuring 2.2 metres long and weighing in at 26.3kg and 25.1kg,  
 Monash Motorsport welcomes M19-E and M19-C!

Figure 8.15: Celebratory social media marketing post for the completion of the new monocoques.

# Chapter 9 Evaluation & Review

## Evaluation

The raw tub masses for the M19-E and M19-C monocoques were 26.3kg and 25.1kg, both of which were well within the range of early estimates. The exterior surface finish straight out of the mould exceeded expectations, with only a couple slight machining marks from the CNC folding process being visible up close. A detailed breakdown of issues or changes made at every manufacturing stage follows.

## Manufacturing Issues Encountered

### Outer Skin Cure

The original plan for the outer skins was to use bolts as locating pins for all the hardpoints and layup around these holes, as can be seen in Figure 9.3. However, this proved to be very time consuming and with the tight working schedule it was decided to ignore this step and drill the holes in the outer skin post cure. Aside from this, the rest of the outer skin layup was fairly straightforward, with the prepreg providing adequate tack on the first ply to allow it to adhere to the smooth mould surface. The debulk interval every 2 to 3 plies for most regions also proved to be very effective at consolidating the layup. It took on average 5 days to complete the outer skin layup for each monocoque, starting from mould releasing to final vacuum bagging, with approximately 2 debulk sessions per day.

The final autoclave vacuum bag was sealed on the first attempt for both cars which was ensured by performing prior leak tests. The generally accepted criteria is for the vacuum pressure to drop by no more than 2" Hg (equivalent to ~6.7kPa) over a period of 5 minutes. Extra care was taken in the storage and handling of the vacuum bag to prevent accidental puncturing and leaks.

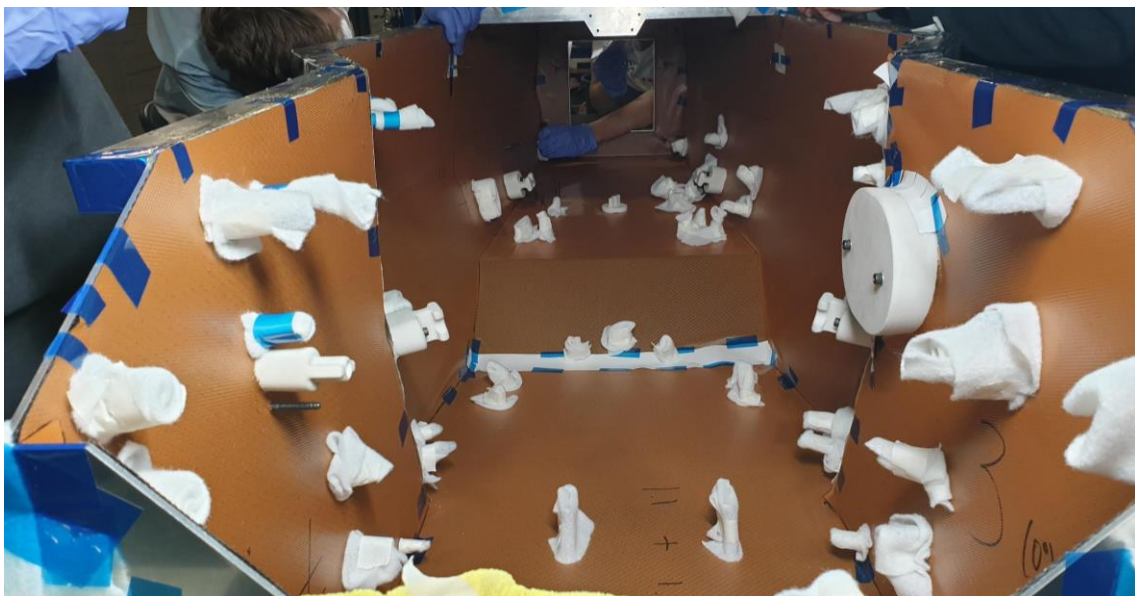


Figure 9.1: First ply with bolt locating pins visible.

There were visible signs of thermal expansion effects post cure. This was to be expected to some degree as there was a thermal expansion coefficient mismatch between the aluminium mould and carbon fibre skin. During the autoclave cycle, the mould would have expanded more under heating, and consequently shrink more upon cooling. This left the carbon skin to bow slightly across the largest flat sections, however this would not be expected to be an issue for subsequent cures with the core providing adequate stiffness to prevent warping upon cooling.

## Core and Insert Bonding

Following the outer skin cure, the hardpoint holes had to be drilled through the carbon skin. Care had to be taken to clamp the skin to the mould such that it would not bow and release itself off the mould when applying drill forces. The skin surface also had to be sanded and prepped for bonding. An orbital disc sander with a low grit of around 40-60 was used, and die grinders with grinding attachments used to get too difficult to reach areas.

The most time consuming component of the entire monocoque production proved to be cutting and fitting the honeycomb core. As explained earlier on pg. , the core required chamfering on the edges in order to fit together. Initially a jig was prototyped using a Dremel rotary cutting tool to create the chamfers, however it proved to be ineffective as the cutting disc diameter was too small to create full depth cuts. It was quickly found that a circular saw and angle grinder were very effective for rapid material removal, and when combined with the Dremel for finer detailing proved to be the most efficient combination.



*Figure 9.2: Prototype Dremel chamfering jig.*

Fitment of the chamfered core into the monocoque required a lot of care and patience. The most efficient procedure for accomplishing this was revealed to be laying down adhesive film onto the prepped outer skin first, then inserting the core and finally applying foaming adhesive at the spliced interfaces. The order in which the core was inserted required pre thought, and the placement during insertion had to avoid snagging and dragging on the pre laid adhesive film. Failure to do so would result in a dry patch where there would be no bond between the core and carbon skin. A small clearance gap of 1-2mm had to be given for the foaming adhesive to be able to be inserted and splice the core segments. Too large a gap would result in the foaming adhesive not being able to fully expand and bridge the gap. In total the time

taken from cutting and chamfering the core to having it fully bonded to the monocoque was just over one week.



*Figure 9.3 Core insertion process.*

At the same time as inserting core, the welded aluminium front roll hoop and cylindrical hardpoint inserts also had to be bonded to the monocoque. The front hoop was welded together on a steel jig that was then heat treated by AMTS.

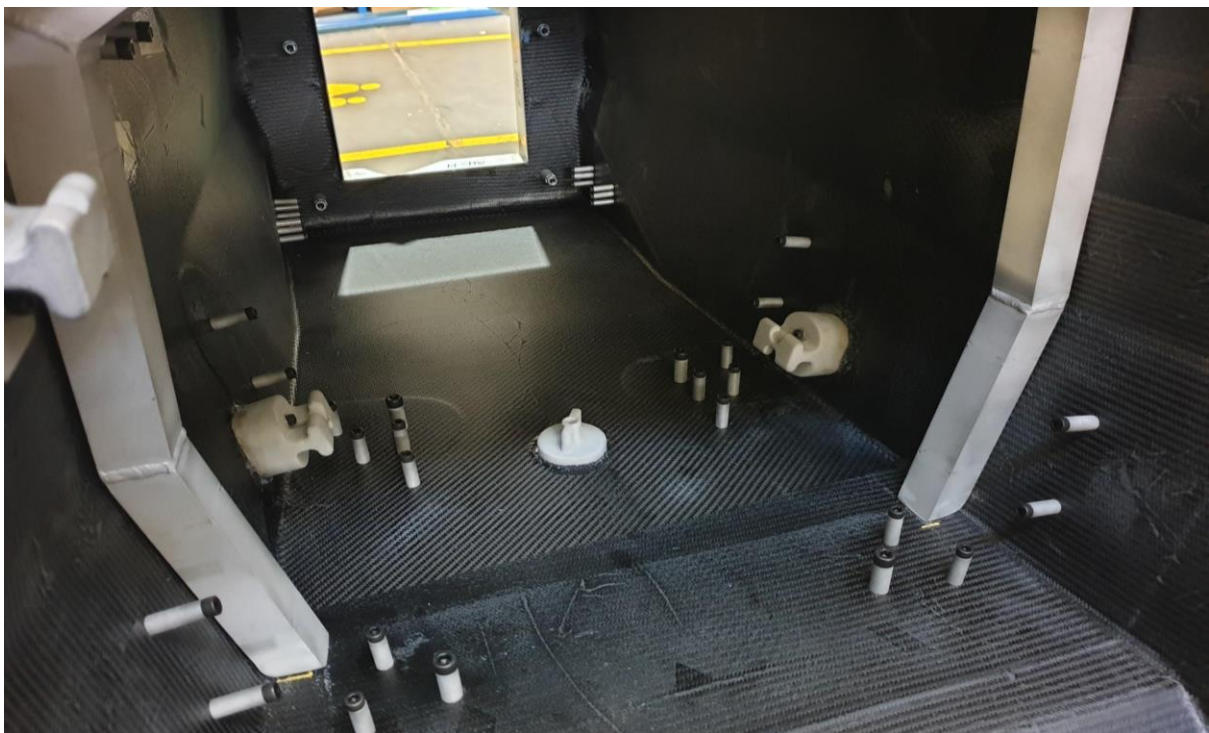


*Figure 9.4: Test fitment of the front hoop and inserts.*

Potting the hardpoint inserts into the core was straightforward. The best solution was to pry the core apart where the hardpoint was to be located and then insert the hardpoint with foaming adhesive wrapped around it. A tight fit was necessary to ensure proper bonding. For insert groups such as wishbone attachments or steering mounts, a backing plate was bolted on to ensure the hardpoints would not float or become lodged at an angle inside the core. It also added additional clamping force onto the outer skin to improve the bond.

The dash outer skin and mould panel of the monocoque could not be bolted to the rest of the mould and laid up until after the hoop was inserted due to clearance issues. This presented some issues as it would therefore have to be co-cured with the core. The issues did not become apparent until full demould of the monocoque at the end, but was essentially a result of lack of constant vacuum pressure applied in the autoclave because of the core interfering, leaving a substandard laminate that was not properly compacted. A separate 2 ply prepreg skin was later bonded over the dash panel for cosmetic reasons. The same issue occurred for the exposed edge faces of the core in the cockpit opening, which had been covered up by an aluminium closeout with prepreg laid up over the edge.

## Inner Skin Cure

The layup of the inner skin was by far the least time consuming with the fastest turnaround of 2 to 3 days for the M19-C monocoque with an average of 2 debulk sessions per day. The M19-E inner skin layup was completed over a period of 5 days with only 1 debulk session per day. Some work was required before the layup could commence however. On both occasions after the core cure, the foaming adhesive at the core splices did not provide full coverage in some regions and therefore required more adhesive to be wedged in. In other areas, the foaming adhesive had expanded too much and created ridges which then needed to be sanded back.

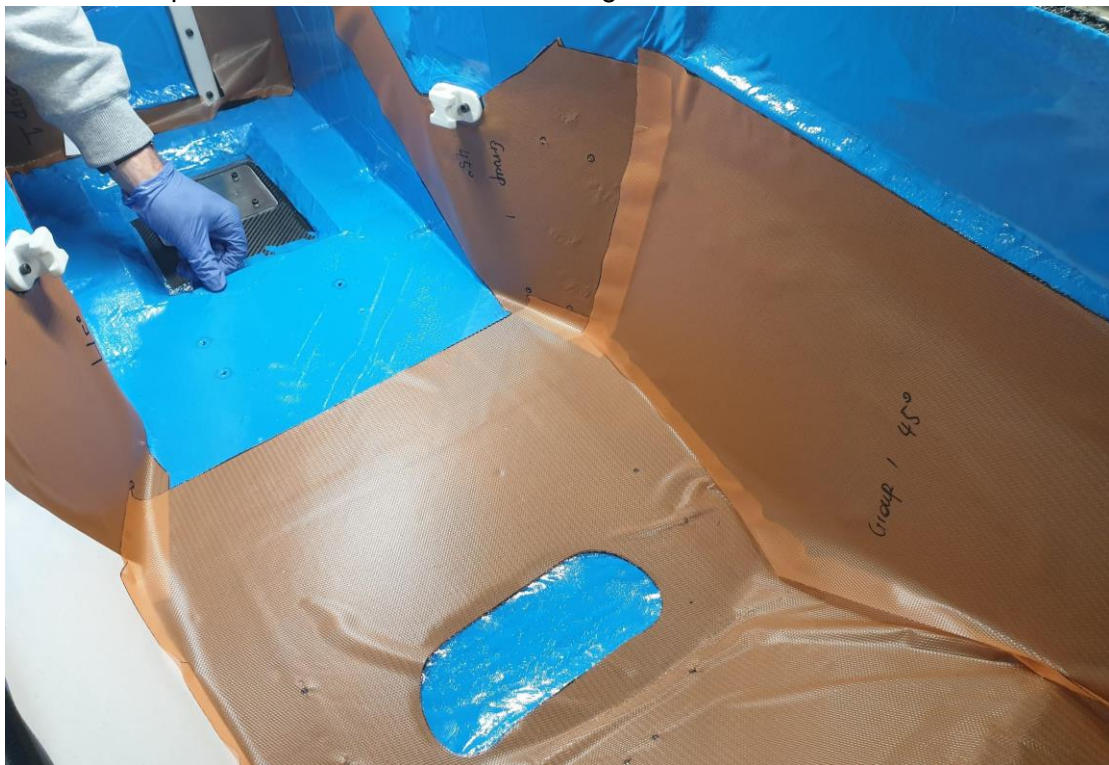


Figure 9.5: First prepreg ply of the inner skin with adhesive film.



## Post-manufacture Inspection

Prior to full car assembly, a range of NDT inspection techniques were sought after to validate the structural integrity of the monocoque. The most commonly used inspection techniques are ultrasonic scanning, radiography and the tap hammer test. These methods are used to identify any defects in a composite laminate or sandwich panel, in particular delamination or debonding.

There was a new opportunity to perform either ultrasonic scanning or radiography through a potential new team sponsor ATTAR. However, after initial talks and delivering some samples to test with it was concluded that the monocoque structure was too complex to draw meaningful conclusions with the equipment they had available, rather their equipment was more suitable for aerospace standard thick laminates as opposed to thin walled honeycomb sandwich structures. There may be opportunities in the future to co-develop a phased array UT scanner tuned to structures such as the monocoque.

Instead, the tap hammer method was employed. As suspected from the sub-optimum vacuum bag for the core bond cure of the M19-C monocoque, some areas of delamination or debonding between the core-skin interface were detected. The M19-E monocoque also exhibited some very minor delamination zones, most likely attributed to adhesive film being dislodged while inserting the honeycomb core.

## Delamination Repairs

### Repair Techniques

There are several composite panel repair techniques documented in literature [37]. These are briefly outlined in the section below.

#### Repair Plug

The repair plug is typically classified as being non-structural and purely cosmetic. It is used for small damage and mainly for sealing off a surface from environmental attacks such as moisture ingress. The plug can be either purely potting compound or a hand layup composite patch laminated to the exterior surface. For core-skin disbonds this type of repair method is not suitable.

#### Resin Injection

Resin or thixotropic adhesives may be injected between gaps within a laminate or sandwich panel bond. Holes are drilled into the composite structure, usually one for injecting with a syringe and the other for venting of air. This type of repair technique is easy to apply, however the reliability and structural integrity is difficult to validate post-repair without extensive NDT. It is typically not recommended for high end aerospace applications because of this risk.

## Laminated Doubler Patch

A doubler patch acts in the same way as doubler plates in ship repairs. The damaged area must first be removed, and any core damage must be replaced with either a new core or a solid insert, before the doubler may be laminated over to patch the damaged area. This type of repair is not suitable for the widespread scale of disbonds. Additionally, the repair patch is not flush with the existing surface and so would alter the physical appearance of the part.

## Scarfed Patch

A scarf repair restores a damaged component to be fully flush in its original state. The damaged area is completely removed and then a chamfer (i.e. a scarf) is applied to the edges of the hole cut-out. The repair patch, either pre-cured or secondary bonded, is also tapered and designed to fit inside the chamfered hole. This type of repair has good aerodynamic benefits for a race car and is the preferred method for Formula 1 wing repairs, however, requires a degree of skill and experience to execute properly.

## Selected Technique

Based on the knowledge and skills of the team, as well as the tight testing schedule, the team opted for the fastest method of repair technique that is resin injection.

## Validation Testing

To verify that the injection repair method would be sufficient for the purposes of a Formula Student monocoque, a set of representative test panels were manufactured to simulate a resin injected composite honeycomb sandwich panel. Panels were manufactured using traditional techniques, but then were deliberately delaminated by unpeeling once of the carbon skins. No surface preparation or modifications were done to replicate the scenario in the actual monocoque.

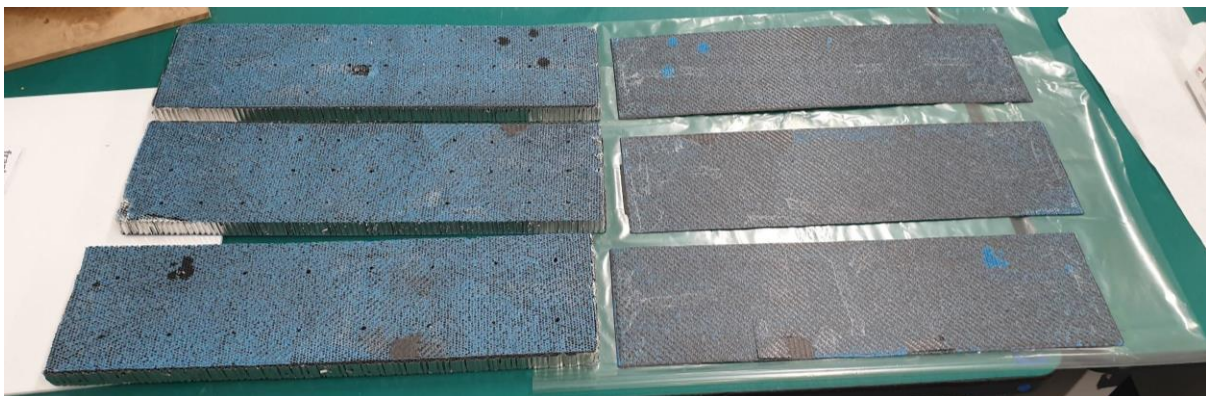


Figure 9.6: Delaminated samples.

In total four panel specimens were manufactured. One was left as a control and was untampered. Another was repaired with injection holes spaced every 70mm in a grid array, while the remaining two were both repaired with 50mm spaced grid array injection sites. The spacing was chosen based on accessibility in the monocoque chassis to drill holes. The resin used in the repairs was West Systems 105 epoxy resin and 205 fast hardener. This resin is popular within the boat repair market, is locally sourced, exhibits exceptional strength characteristics and has low viscosity suitable for injection.

The panels were physically tested in the Instron UTM in the same configuration as the three point bend tests. The force-displacement results of the validation tests can be seen below and demonstrate that the repair technique was able to fully restore the strength of the damaged panels. Not only was the strength fully restored or exceeded but the stiffness (i.e. gradient) of the panel also increased slightly. The reasoning behind this is the extra resin filling the honeycomb cells increases the second moment of area of the panel. The repairs did come with a mass penalty however, with a 40% increase in panel mass being observed.

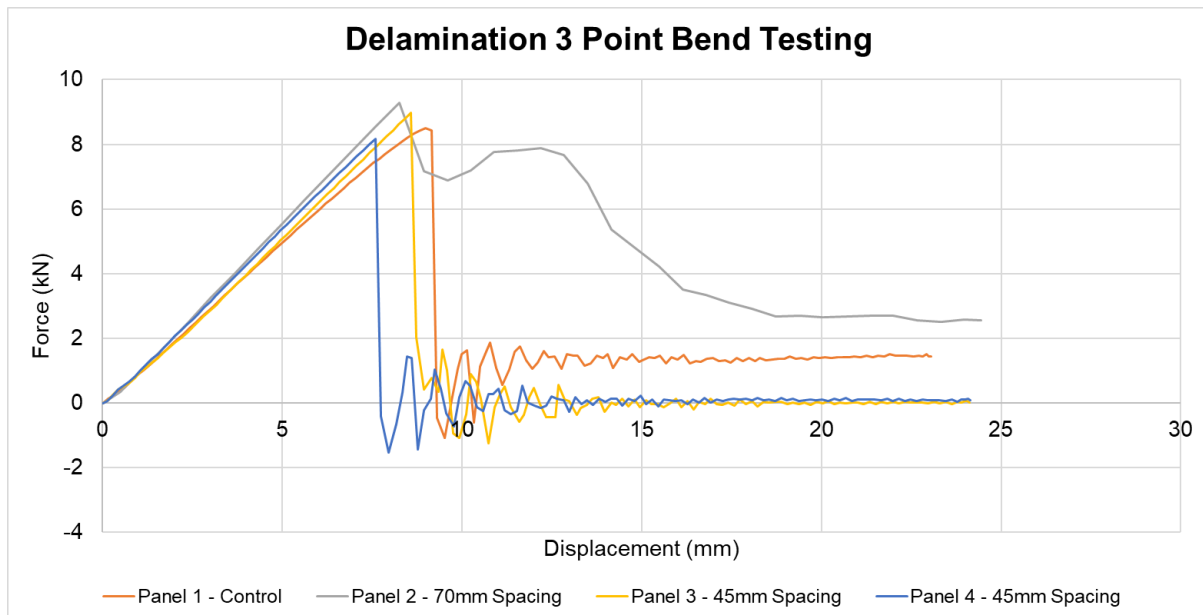


Figure 9.7: Physical testing validation of resin injection repair methods.

## Implementation

The repairs took place within two weeks after the monocoque manufacturing period was completed. Regions of suspected delamination were mapped out on the inside of the chassis and injection holes were drilled out. The holes were drilled from the inside to preserve a damage free surface on the exterior. Injection took place in four operations, one for each orientation (top, bottom, left, right) of the monocoque using gravity to assist with resin flow to the core-skin interface. Following tap hammer tests post-injection to validate the bond had been restored, the drill holes were filled with black dye epoxy and sanded smooth.

## Torsion Bench Test

As part of validating the FEA model, a physical bench test for measuring hub-to-hub installation stiffness, colloquially known as *torsional stiffness*, was performed on the M19-C monocoque.

### Setup

The bench setup constrains the vehicle in the same manner as the FEA constraints, with one fully fixed rear outboard, the other as a roller support, and the front axle acting as a pivot point with a point load applied at each front outboard but in opposite directions.

Because the bench test is a measure of installation stiffness, the shocks of the suspension system were replaced with solid steel bar *dummy* shocks to eliminate any unwanted compliance in the system. The main roll hoop, KTM 690 engine and the majority of the combustion powertrain were also installed to provide a fully representative vehicle.



Figure 9.8: Test setup.

The hub-to-hub installation stiffness is derived from measuring vertical deflections at the hub at a given load, or *torque*, applied to the chassis at the front hubs. This was measured by positioning dial gauge measurement devices on the hubs to provide readings. The lateral position of the dial gauge relative to the vehicle centreline is important. Additional dial gauges were placed along the longitudinal axis of the car at the dash, main hoop and rear bulkhead to provide additional readings and to generate a stiffness distribution plot of the car.

The load application at the front hub was achieved by hanging multiples of 10kg weights on one hub and an equal amount off the other but via a pulley system in order to load the hub in the opposite direction. The two opposing force vectors create the *torque* applied to the chassis. The weights were measured on a precision scale to give precise mass readouts as they were actually slightly under the advertised 10kg mass.

As a bare minimum requirement, two runs were performed loading the chassis in a clockwise direction and two runs in an anticlockwise direction. Performing more runs allows for better averaged results. A Microsoft Excel spreadsheet calculator as seen in Figure 9.13 was created to manage and record all data collection, in particular the dial gauge readings which were read manually and required conversion of units as some gauges were metric and other imperial.

# Results

In total seven runs were performed with four tests in the counter clockwise direction and three in the clockwise direction. Results from one of CCW tests were scrapped due to improper setup of a dial gauge resulting in it reaching it's positive stop before maximum deflection.

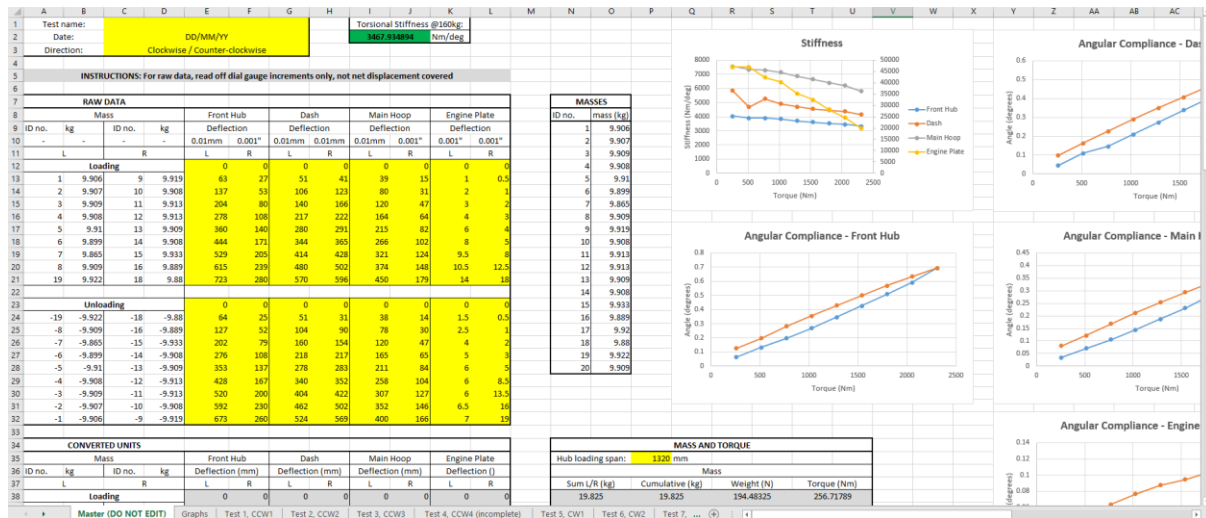


Figure 9.9: Spreadsheet calculator for torsion testing.

The calculated installation stiffness was found to be non-linear as more torque was applied. For direct comparison with the tested installation stiffness of the previous iteration MMS steel spaceframe chassis in 2017, the presented stiffness values are taken when 160kg of total load was applied, equating to approximately 1026Nm. The averaged hub-to-hub installation stiffness of the M19-C monocoque is shown in Figure 9.14 below.

CCW	Nm/deg	CW	Nm/deg
1	3467.935	1	3419.475
2	3583.218	2	3611.184
3	3663.309	3	3565.133
<b>AVG</b>	<b>3571.487</b>	<b>AVG</b>	<b>3531.931</b>

<b>Average ALL</b>	<b>3551.709</b>	<b>Nm/deg</b>
--------------------	-----------------	---------------

Figure 9.10: Summary of hub-to-hub installation stiffness results.

For the same 160kg loading scenario, the distribution of compliance (inverse of stiffness) along the longitudinal axis of the chassis is plotted graphically in Figure 9.15.

## Discussion

There can be seen to be a 1 percent difference between physical testing (3551Nm/deg) and the simulated results (3515Nm/deg). This may seem incredibly accurate but the results can be misleading. More accurate results are expected in the future as the team develops more data and experience. A more accurate model that utilises solid elements rather than shell elements is recommended. As well as that, the mechanical properties of the panels can be fine-tuned through correlation between physical and simulated results of panels in 3 point bending. Finally concerns of manufacturing quality have been raised and will no doubt be addressed in the next manufacturing period.

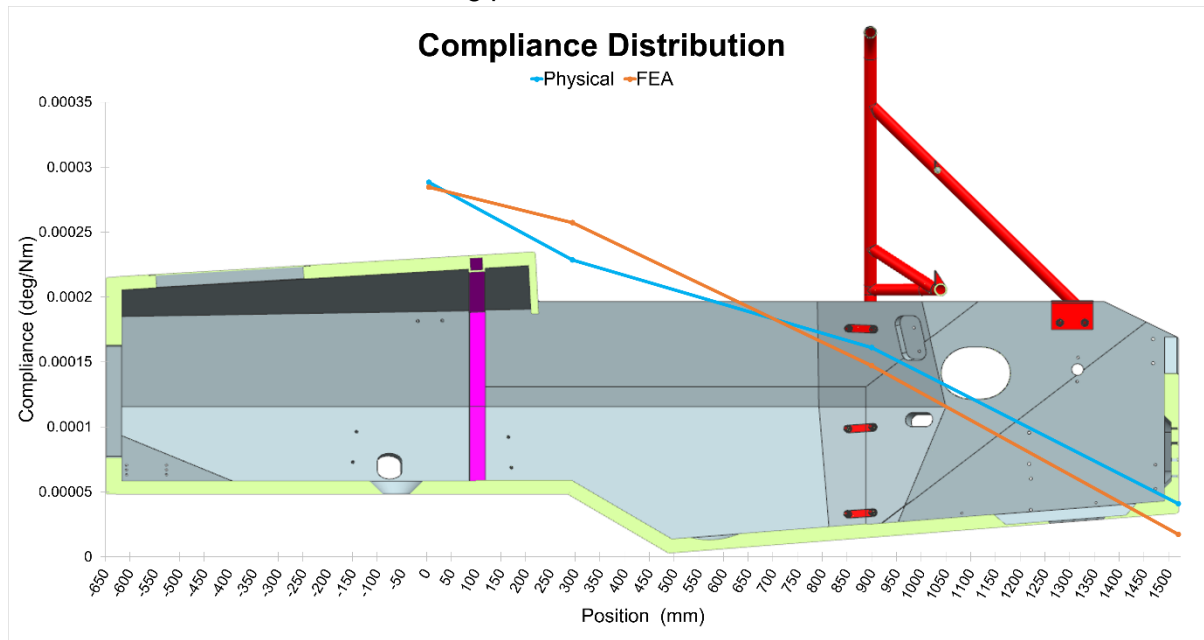


Figure 9.11: Comparison of compliance distribution along the chassis longitudinal axis between physical and FEA results.

In comparison, the 2017 spaceframe featured a stiffness of 1977Nm/deg and an error of 5 percent between physical and simulated. The major differences between 2017 and 2019 were as expected. The additional strength and stiffness per weight of composite panels in comparison to steel tubes is the main reason behind the team's decision to transition to a carbon monocoque. The chassis has nearly doubled in torsional stiffness while still weighing a similar weight. The team will aim to significantly reduce this weight in the coming years. The reduction in FEA accuracy compared to the physical bench test was also as to be expected with the added complexity that accompanies composites.

Looking at the distribution of compliance along the longitudinal axis of the chassis it can be seen that the least compliance per distance occurs in the cockpit. For reference, compliance is the inverse of stiffness, meaning that the chassis is most stiff in the cockpit. This may be surprising given the lower moment of inertia that you would presume comes with an open cockpit section, but alas this is not the case. This is because of the added strength and stiffness that the side impact structure and floor has in comparison to the rest of the chassis. These additional properties are requirements set by the Formula Student rules.

# Conclusion

The design, testing and manufacture of all new monocoque chassis for Monash Motorsport in 2019 has been the culmination of over four years of research and development. Transitioning from the tried and tested tubular spaceframe chassis to a carbon fibre composite monocoque chassis has been a significant undertaking, requiring a whole new knowledge base, analysis tools and manufacturing skills within the team.

After an in-depth review of composite theory, new design tools have been created to aid future monocoque designers. FEA simulation tools using ANSYS ACP are able to predict composite panel 3 point bend failure loads and chassis installation stiffness with an error of less than 5% compared to physical testing data, while a MATLAB script has been developed to provide an early prediction on the strength of chassis hardpoint inserts used for localised loading of the monocoque. These tools will be able to reduce analysis time in the future and eliminate the need for extensive physical testing, both a time consuming and costly process.

The geometry design of the 2019 monocoques has been an ambitious one; aimed at allowing for a much larger aerodynamics package as a result of tighter and narrower packaging of the driver, suspension and powertrains. Input and integration from all parties was critical to achieving a design that would be satisfactory for everyone.

A highly innovative laser cut and folded aluminium mould saw drastic reductions in cost and manufacture time compared to the traditional composite tool manufacture process. To complement this, a low temperature curing GMS Composites EP-270 twill weave prepreg CFRP was chosen to be combined with a Plascore 5056 aluminium honeycomb core to form the sandwich panel construction. In total, two monocoques were produced by the chassis section in six weeks, weighing in at 25.1kg and 26.3kg: a phenomenal effort. Post NDT evaluation of the finished monocoques did reveal some manufacturing defects, however these were quickly rectified using validated composite repair techniques. A post repair torsional analysis test saw a recorded 3551Nm/deg chassis installation stiffness for the M19-C monocoque.

The 2019 monocoques have laid down the foundations for future successful chassis designs, but in order to continue the evolution from the best Formula Student team in Australasia to the best in the world there are a number of steps that we recommend are taken. These include changes to the geometry, materials, manufacturing techniques, analysis and testing conducted. All of these recommendations are expanded on in the following chapter.

# Chapter 10 Future Developments

This chapter is dedicated to presenting future monocoque chassis development paths for the team at Monash Motorsport.

## Chassis Design

### Geometry

There are further potential mass reductions to be had by altering the geometry of the monocoque chassis. The footwell of the cockpit may potentially be shortened to only package up to the 95% percentile male and the size of the front bulkhead could be reduced by tapering in the nose section.

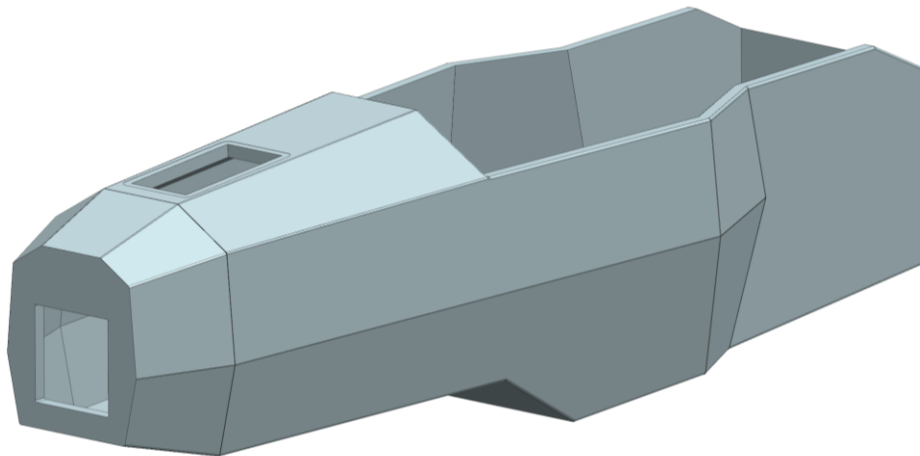


*Figure 10.1: Conceptual front bulkhead size reduction.*

Looking further rearward, the high side impact structure could be reduced in height. There are considerations for driver safety and overall aesthetics of the race car to be had however. The main roll hoop height could potentially be made lower for two reasons: one mass and the other to clean up airflow to the rear wing and conceivably implement a bi-plane wing for increased downforce.

Obviously, a change in design philosophy and overall vehicle concept will have a significant sway in terms of chassis geometry. The above comments mainly apply to the current high downforce aerodynamics concept for 2019 and may not be relevant for future MMS vehicles.

### Material Selection

The choice of materials used in the monocoque can heavily influence the overall performance and mass of the chassis. Currently the GMS Composites EP-270 prepreg CFRP is locally sourced and decently priced, but it is lacking in perimeter shear strength and so is restricting mass savings in the front bulkhead and side impact structure of the monocoque. The main barrier to moving to higher performance prepreps is financial, but if that were not an issue or sponsored stock could be sourced then it should definitely be reinvestigated.



The core material could also see large potential performance gains. Currently the entire monocoque is restricted to 1" thick core in all regions, however it could be worth investigating changing core thicknesses to aid in packaging or to increase strength and stiffness in certain areas, and vice versa. The core type could also potentially be reinvestigated for the same reasons as why the GMS Composites EP-270 prepreg was chosen: locally sourced and cheaper stock. The current grade Plascore aluminium honeycomb is one of the highest commercially available grades of aluminium core, and therefore commands a higher price tag. GMS Composites does supply cores of different specifications, so it could be worth researching prices and material properties to see if there are gains to be had there.

The last item that could be looked into concerns chassis torsional stiffness. An incredibly efficient way to improve the strength of the monocoque is to use unidirectional fabrics instead of woven fabrics. While this won't be sufficient for SES rules equivalency due to the extreme anisotropic behaviour of UD fabrics, they can be used as additional plies of reinforcement.

## Analysis

### Modal Analysis

There have been reported cases of the natural frequency of a composite monocoque chassis causing issues in the competition. The issues ranged from car shutdowns in the high voltage tractive system to extreme cases of the natural frequency of the monocoque matching the driver's eyes at certain engine RPM ranges, severely affecting driver vision and safety. No such cases have been reported to date with the 2019 monocoque chassis, however it is something that should be considered and not forgotten or ignored in future designs. The ANSYS FEA package supports modal analysis so could definitely be implemented as part of the design process for the team.

### Hardpoint Inserts

Further improvements for predicting hardpoint insert load capacities can potentially be achieved by developing an FEA model. Whether it will be a more efficient method than using the simple MATLAB script for preliminary sizing of inserts remains to be seen. In either case, physical testing is still the preferred method of design validation as that will be the most representative.

With regards to the current insert design, one test that has yet to be completed is fatigue loading of the inserts. This is particularly of concern for wishbone attachment inserts, as these see the most cyclic loading of any loaded insert in the monocoque. Theory suggests that the fatigue life of composites is superior to metallic materials and is near infinite in some cases. Mechanical testing of carbon wishbones and bonded metallic inserts [39] has already hinted at this however actual validation of a monocoque insert is still desirable.

The design of the hardpoint insert may not be strictly limited to aluminium tube inserts in the future. There are potential weight savings to be had using lower density materials such as

balsa wood or monolithic CFRP, the second of which is quite popular amongst the competition, and was briefly considered for 2019 with prototype inserts made (see Figure 11.3 below). These insert designs utilise similar effective core bonding area to the aluminium inserts, but rather than a small potting radius and large core height they utilise a large potting radius and small core height for their strength, as such they can also be known as *tapered* inserts. Manufacturing for these types of inserts can be more complex and time consuming however.

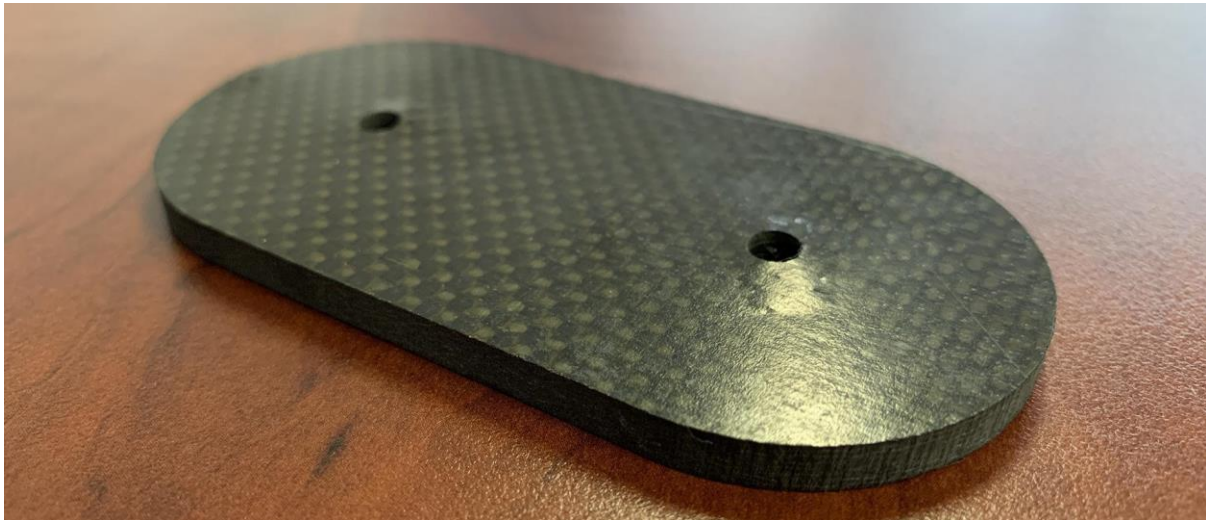


Figure 10.2: Prototype waterjet cut CFRP hardpoint insert.

## Testing Infrastructure

All of the test rigs used on the Instron UTM could see some modifications to improve ease of use and efficiency. This includes method to make alignment of panels more streamlined, or tools to make turnaround time between one test and the next much faster. Additionally, in the case of the hardpoint insert test rig, eliminating compliance should have a high priority as it will the team to make accurate predictions on insert stiffness based on the physical tests.

## Manufacturing

### Mould

Laminating by hand in a one-piece female mould proved to be difficult as access to the inside of the monocoque was severely limited. If the opportunity exists, it is recommended that the monocoque is manufactured in two halves, top and bottom, and then bonded together via a bonded scarf joint. While further testing and equivalency must be shown for the joining method of the two halves, the drastically improved accessibility would reduce manufacture time significantly.



Figure 10.3: Constrained working conditions inside the mould.

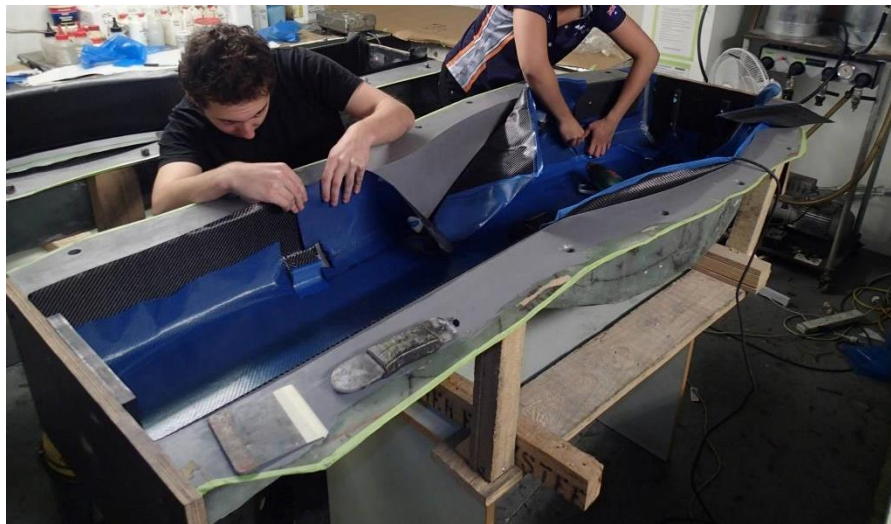


Figure 10.4: Top and bottom chassis moulds from University of Auckland 2013. [40]

## CNC Ply and Core Cutting

There are significant time savings to be had in the manufacturing stage with regards to cutting the prepreg plies and honeycomb core. In 2019 these were all done manually using hand tools, however since then trials have been made using CNC machines to streamline the process. Not only does it reduce time but also increases the accuracy of the cutting geometry.



Figure 10.5: CNC ply cutting trial with Monash Food Innovation.

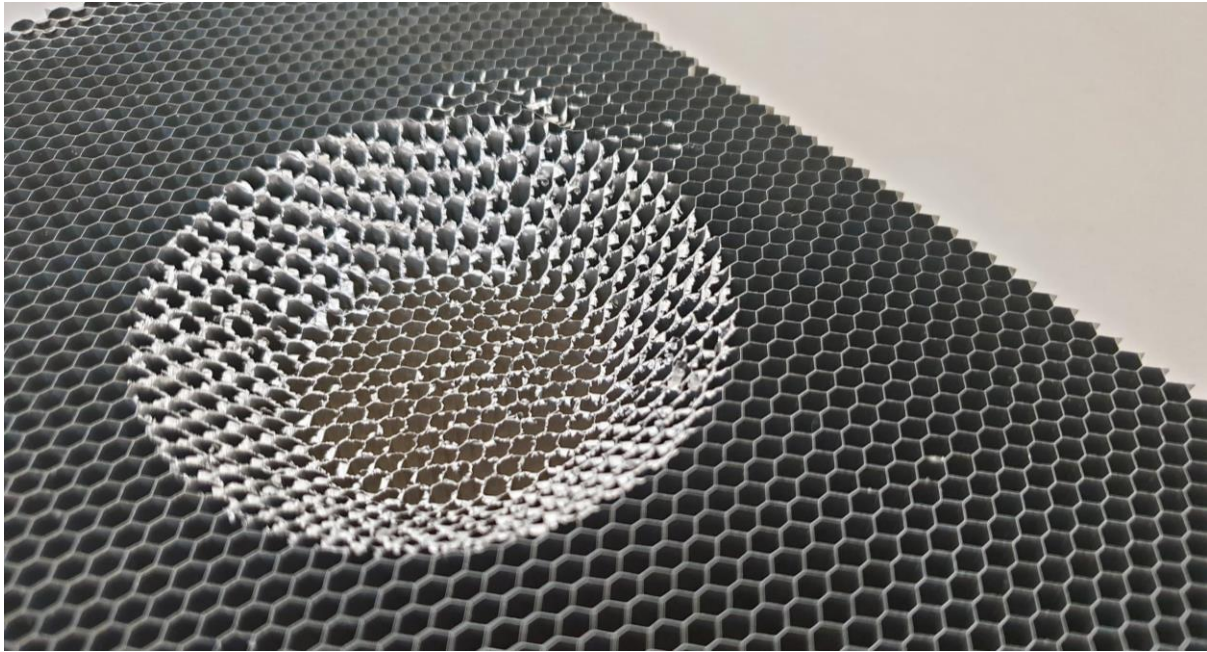


Figure 10.6: CNC routed aluminium honeycomb core.

## Core Splicing

The foaming adhesive proved to be fairly difficult and expensive to work with. Other options other than the chosen Hexcel HexBond 212-NA foaming adhesive film are available and may be worth investigating. In particular, liquid adhesives may prove to be easier to use as they can be cured at room temperature during the core bonding process. This may assist to holding the core in the right location before hardpoint inserts are inserted and the vacuum bagging process are completed. That being said, the foaming adhesive film used is said to be of a high quality and is aerospace grade so a better option may not exist.

## Testing and Validation

### NDT Ultrasonic Scanning

As mentioned on pg. , keeping close communications with ATTAR in the future may open up opportunities for a phased array UT scanner for composite panels, allowing for through NDT on the monocoques post manufacture.

### 3D Laser Scanning

The accuracy of the laser cut and folded mould was never fully verified. It was known that there were inaccuracies in some of the bend angles, but the degree and scale on the entire monocoque is still largely unknown. Due to time constraints, the 2019 monocoques were never analysed in detail, however MMS has the industry support from sponsor Veris to be able to perform 3D laser scanning and analysis of the monocoques in the future.

## Chassis Torsion Testing

### On-track Stiffness Targeting

The current chassis installation stiffness targets are based off purely theoretical vehicle dynamics models, and to date MMS has yet to validate and quantify the performance gains to be had on track with increased or decreased installation stiffnesses. Performing this kind of testing on track with a monocoque chassis is difficult. Stiffness may be increased via the addition of bracing structures however testing reduced stiffness is near impossible. Rather, a steel spaceframe chassis is a much easier solution as steel tubes may be either welded on or cut off to alter the chassis stiffness. This is something MMS has at its disposal with the previous year's M18-C combustion vehicle still in service.

Plans have been made previously to perform an on track torsion test with a spaceframe chassis but never came to fruition. Finer details such as what sensors are required and the track setup have yet to be finalised. Because chassis stiffness mostly affects the rate of longitudinal load transfer, track configurations with dynamic slaloms and chicanes are likely to produce more pronounced effects in lap time and handling as opposed to long sweeping steady state transient type corners. A slip angle sensor is also most likely required to be able to measure the responsiveness of the chassis.

### Postseason Testing

For vehicles which compete over a long period of time at many competitions, it may be worth investigating the reduction in chassis stiffness, if any, after prolonged driving periods. MMS currently has no data on whether the chassis stiffness does decrease over time or not, and to what extent. If this data existed it could aid in future designs where the loss of chassis stiffness is compensated for in the original design, to ensure that the chassis stiffness is still at acceptable levels come the final competition for that vehicle. In the case of MMS, the last competition in the season for one of their vehicles is usually Formula Student Germany, where the competition is most fierce and so peak vehicle performance is of utmost importance.

# Chapter 11 References

- [1] D. Mazur, "FSG media," 2019. [Online]. Available: <https://media.formulastudent.de/>.
- [2] D. Case, "Formula SAE - Competition History 1981 - 1996," *SAE Technical Paper 962509*, p. 23, 1996.
- [3] D. Mazur, "Formula Student - World Ranking Lists," 2019. [Online]. Available: <https://mazur-events.de/fs-world/>.
- [4] Formula Student Germany, "FSG Magazine 2019," 24 July 2019. [Online]. Available: <https://www.formulastudent.de/pr/magazine/>.
- [5] SAE International, "2019 Formula SAE Rules V2.1," 2019. [Online]. Available: <https://www.fsaeonline.com/cdsweb/gen/DocumentResources.aspx>.
- [6] Monash Motorsport, "Monash Motorsport," 2019. [Online]. Available: <https://www.facebook.com/monashmotorsport/>.
- [7] Formula 1 Dictionary, "Chassis," [Online]. Available: <http://www.formula1-dictionary.net/chassis.html>.
- [8] Formula 1 Dictionary, "Monocoque," [Online]. Available: <http://www.formula1-dictionary.net/monocoque.html>.
- [9] McLaren Automotive, "35 years ago McLaren built the MP4/1, the world's first carbon fibre Formula 1 car," [Online]. Available: <http://tiny.cc/swivez>.
- [10] McLaren Automotive, "30 years of carbon fiber innovation as McLaren unites John Watson with the MP4-12C," EuroCar News, 3 July 2011. [Online]. Available: <http://www.eurocarnews.com/0/0/1137/0/30-years-of-carbon-fiber-innovation-as-mclaren-unites-john-watson-with-the-mp4-12c.html>.
- [11] Rennteam Uni Stuttgart e.V., "F0711-12 (2017)," [Online]. Available: <https://www.rennteam-stuttgart.de/f0711-12/>.
- [12] D. Mazur, "FS Rules 2019 V1.1," 2019. [Online]. Available: <https://www.formulastudent.de/fsg/rules/>.
- [13] W. Milliken and D. Milliken, *Race Car Vehicle Dynamics*, Warrendale: Society of Automotive Engineers, Inc., 1995.
- [14] O. Danielsson and A. G. Cocaña, "Influence of Body Stiffness on Vehicle Dynamics Characteristics in Passenger Cars," Chalmers University of Technology, Goteborg, 2015.
- [15] C. Smith, *Tune to win*, Fallbrook, CA: Aero Publishers, Inc., 1978.
- [16] M. Hermann, "Torsional Stiffness and Natural Frequency Analysis of a Formula SAE Vehicle Carbon Fiber Reinforced Polymer Chassis using Finite Element Analysis," December 2016. [Online]. Available: <https://pdfs.semanticscholar.org/66ff/f806b31f1b199bb03100fc5c5e19c23935f2.pdf>.
- [17] A. Mapson, "Design, Manufacture and Testing of Suspension for a Formula SAE Car," Monash University, Clayton, 2009.
- [18] W. Yan, *Class Lecture, Topic: "Chapter 3: Micromechanical Analysis of Lamina"*, Monash University, Melbourne: MEC4426, Department of Mechanical and Aerospace Engineering, 2018.
- [19] A. K. Kaw, *Mechanics of Composite Materials*, 2nd ed., Boca Raton, Florida: CRC Press, 2006.
- [20] A. Petras and M. Sutcliffe, "Failure mode maps for honeycomb sandwich panels," *Composite Structures*, vol. 44, no. 4, pp. 237-252, April 1999.
- [21] R. D. Story, "Design of Composite Sandwich Panels for a Formula SAE Monocoque Chassis," Oregon State University, Corvallis, 2014.
- [22] Hexcel Composites, "HexWeb Honeycomb Sandwich Design Technology," December 2000. [Online]. Available: [https://www.hexcel.com/user\\_area/content\\_media/raw/Honeycomb\\_Sandwich\\_Design\\_Technology.pdf](https://www.hexcel.com/user_area/content_media/raw/Honeycomb_Sandwich_Design_Technology.pdf).
- [23] O. T. Thomsen and W. M. Banks, "An improved model for the prediction of intra-cell buckling in CFRP sandwich panels under in-plane compressive loading," *Composite Structures*, vol. 65, no. 3-4, pp. 259-268, 2004.
- [24] European Cooperation for Space Standardization, ECSS-E-HB-32-22A Space engineering: Insert design handbook, Noordwijk: ESA Requirements and Standards Division, 2011.
- [25] TUfast Racing Team, "Vehicle Dynamics," 17 November 2018. [Online]. Available: <https://www.formulastudent.de/academy/20181117-zf/>.
- [26] N. McIver and R. Paine, "Design of a F-SAE Carbon Fibre Monocoque Chassis," Monash University, Clayton, 2015.
- [27] Edith Cowan University Racing, "Edith Cowan University Racing," 2014. [Online]. Available: <https://www.facebook.com/pg/ECU.Motorsport/photos/>.
- [28] Revolve NTNU, "Revolve NTNU," 2016. [Online]. Available: <https://www.facebook.com/pg/RevolveNTNU/photos/>.

- [29] H. Haugum and M. Pløen, "Design, Analysis and Testing of Joints on Carbon Fiber Composite Sandwich Chassis," Norwegian University of Science and Technology, Trondheim, 2014.
- [30] RMIT Electric Racing, "RMIT Electric Racing," 2019. [Online]. Available: <https://www.facebook.com/pg/RMITElectricRacing/photos/>.
- [31] Dexcraft, "Aluminium vs carbon fiber – comparison of materials," Dexcraft, 7 October 2015. [Online]. Available: <http://www.dexcraft.com/articles/carbon-fiber-composites/aluminium-vs-carbon-fiber-comparison-of-materials/>.
- [32] A. De Morton, "Development of a Monocoque for F-1," Monash University, Clayton, 2015.
- [33] C. Olorenshaw, "FEA of Composite Sandwich Panels," Monash University, Clayton, 2016.
- [34] ANSYS, ANSYS Composite PrepPost User's Guide, Canonsburg: ANSYS, Inc., 2016.
- [35] M. Alberts and P. Thieffry, "Designing Solid Composites," *ANSYS Advantage*, vol. VII, no. 1, pp. 51-53, 2013.
- [36] J. Block, T. Brander, M. Lambert, J. Lyytinen, K. Marjoniemi, R. Schütze and L. Syvänen, "Carbon fibre tube inserts - a light fastening concept with high load carrying capacity," May 2015. [Online]. Available: <http://articles.adsabs.harvard.edu/full/2005ESASP.581E.133B/0000133.007.html>.
- [37] G. Savage and M. Oxley, "Repair of composite structures on Formula 1 race cars," *Engineering Failure Analysis*, vol. 17, no. 1, pp. 70-82, 2010.
- [38] H. McCredie, "Determination of the Material Properties of Pre-impregnated Carbon Fibre," Monash University, Clayton, 2015.
- [39] D. Crowe, "Design and Development of Carbon Fibre Wheel Shells and Wishbones for a Formula Student Racecar," Monash University, Clayton, 2019.
- [40] University of Auckland Formula SAE Team, "University of Auckland Formula SAE Team," 2013. [Online]. Available: <https://www.facebook.com/pg/UoAfsae/photos/>.